University of Groningen

[Link to publication in University of Groningen/UMCG research database](#)

Internal kinematics of spiral galaxies in distant clusters

IV. Gas kinematics of spiral galaxies in intermediate redshift clusters and in the field[★]

E. Kutdemir[1,2], B. L. Ziegler[2], R. F. Peletier[1], C. Da Rocha[2,3], A. Böhm[4], and M. Verdugo[5]

[1] Kapteyn Astronomical Institute, PO BOX 800, 9700 AV Groningen, The Netherlands
  e-mail: kutdemir@astro.rug.nl
[2] European-Southern Observatory, Karl-Schwarzschild Str. 2, 85748 Garching, Germany
[3] Núcleo de Astrofísica Teórica, Universidade Cruzeiro do Sul, R. Galvão Bueno 868, 01506-000, São Paulo, SP, Brazil
[4] Institute of Astro- and Particle Physics, Technikerstrasse 25/8, 6020 Innsbruck, Austria
[5] Max-Planck-Institut für extraterrestrische Physik, Giessenbachstraße 85748 Garching be München, Germany

ABSTRACT

Aims. We trace the interaction processes of galaxies at intermediate redshift by measuring the irregularity of their ionized gas kinematics, and investigate these irregularities as a function of the environment (cluster versus field) and of morphological type (spiral versus irregular).
Methods. We obtain the gas velocity fields by placing three parallel and adjacent VLT/FORS2 slits on each galaxy. To quantify irregularities in the gas kinematics, we use three indicators: the standard deviation of the kinematic position angle (σ_{PA}), the mean deviation of the line of sight velocity profile from the cosine form which is measured using high order Fourier terms ($k_{3,5}/k_1$) and the average misalignment between the kinematical and photometric major axes ($\Delta\phi$). These indicators are then examined together with some photometric and structural parameters (measured from HST and FORS2 images in the optical) such as the disk scale length, rest-frame colors, asymmetry, concentration, Gini coefficient and M_{20}. Our sample consists of 92 distant galaxies. 16 cluster ($z \sim 0.3$ and $z \sim 0.5$) and 29 field galaxies ($0.10 \leq z \leq 0.91$, mean z=0.44) of these have velocity fields with sufficient signal to be analyzed. To compare our sample with the local universe, we also analyze a sample from the SINGS survey.
Results. We find that the fraction of galaxies that have irregular gas kinematics is remarkably similar in galaxy clusters and in the field at intermediate redshifts (according to $\sigma_{PA} \approx 10\%$, $k_{3,5}/k_1 \approx 30\%$, $\Delta\phi \approx 70\%$). The distribution of the field and cluster galaxies in (ir)regularity parameters space is also similar. On the other hand galaxies with small central concentration of light, that we see in the field sample, are absent in the cluster sample. We find that field galaxies at intermediate redshifts have more irregular velocity fields as well as more clumpy and less centrally concentrated light distributions than their local counterparts. Comparison with a SINS sample of 11 $z \sim 2$ galaxies shows that these distant galaxies have more irregular gas kinematics than our intermediate redshift cluster and field sample. We do not find a dependence of the irregularities in gas kinematics on morphological type. We find that two different indicators of star formation correlate with irregularity in the gas kinematics.
Conclusions. More irregular gas kinematics, also more clumpy and less centrally concentrated light distributions of spiral field galaxies at intermediate redshifts in comparison to their local counterparts indicate that these galaxies are probably still in the process of building their disks via mechanisms such as accretion and mergers. On the other hand, they have less irregular gas kinematics compared to galaxies at $z \sim 2$.

Key words. galaxies: evolution – galaxies: kinematics and dynamics – galaxies: clusters: individual: MS 0451.6–0305, MS 2137.3-2353, MS 1008.1-1224, Cl 0412-65 – galaxies: spiral

1. Introduction

Galaxy clusters are important laboratories for understanding the origin of different morphological types of galaxies. The main reason for that is the relation between local galaxy density and morphological type (Dressler 1980). For nearby rich clusters, the spiral galaxy fraction decreases from 80% in the field to 60% in the cluster outskirts and to virtually zero in the core region. This relation is redshift dependent and while the fraction of elliptical galaxies ($\sim 15\%$, Vogt et al. 2004) does not change with redshift, the S0 fraction increases with decreasing redshift and the spiral fraction, on the contrary, decreases (Couch et al. 1998). The fraction of spirals with no current star formation activity is significantly larger in clusters than in the field (van den Bergh 1976; Poggianti et al. 1999; Couch et al. 2001; Goto et al. 2003; Verdugo et al. 2008; Sikkema 2009). Also, distant clusters have a larger fraction of star forming galaxies compared to nearby clusters (Butcher & Oemler 1978, 1984; Ellingson et al. 2001; Kodama & Bower 2001). It is well established with these observational studies that spiral galaxies have been transformed into S0s mostly in denser regions of the universe. Then the question is what are the physical processes that are responsible for this morphological transformation. Several mechanisms have been proposed such as gas strip-

ping mechanisms: ram pressure stripping (Gunn & Gott 1972; Quilis et al. 2000; Kronberger et al. 2008; Kapferer et al. 2008, 2009), viscous stripping (Nulsen 1982) and thermal evaporation (Cowie & Songaila 1977); tidal forces due to the cumulative effect of many weak encounters: harassment (Richstone 1976; Moore et al. 1998); removal of the outer gaseous halos by the hydrodynamic interaction with the intracluster medium (ICM) plus the global tidal field of the cluster: starvation (Larson et al. 1980); mergers and strong galaxy-galaxy interactions which are efficient when relative velocities are low, and therefore, they mostly occur in galaxy groups or in the outskirts of clusters (Makino & Hut 1997). It is known that cluster galaxies loose gas because of their interactions with the ICM and as a result, their star formation gets switched off. Local studies show that cluster galaxies are deficient in neutral hydrogen compared to their field counterparts and that becomes significant within the Abell radius (Davies & Lewis 1973; Giovanelli & Haynes 1985; Gavazzi 1987, 1989; Solanes et al. 2001). The HI distribution of these galaxies frequently shows asymmetries and displacement from the optical disk as well (Gavazzi 1989; Cayatte et al. 1994; Bravo-Alfaro et al. 2000; Vogt et al. 2004). It was proposed that passive spiral galaxies in clusters might be the intermediate phase before becoming an S0 (van den Bergh 1976). Later on, it was argued that S0's can not be formed by removing gas from disks of spirals via mechanisms such as ram pressure stripping, since S0's have systematically larger bulge sizes and bulge to disk ratios (B/D) compared to spiral galaxies in all density regimes (Burstein 1979; Dressler 1980; Gisler 1980 but see also Aragón-Salamanca 2008). Tidal interactions (e.g. harassment) on the other hand are expected to trigger gas accretion into the circumnuclear regions (Moore et al. 1996) and therefore increase the bulge size and B/D ratio. Therefore, S0's might have formed via minor mergers, harassment or a combination of the two (Dressler & Sandage 1983; Neistein et al. 1999; Aguerri et al. 2001; Hinz et al. 2003).

All these discussions are pointing out that studying stellar populations and morphologies of cluster galaxies is crucial in understanding the interaction processes. What about their kinematics? In the Virgo cluster, for example, half of 89 spiral galaxies that were observed by Rubin et al. (1999) turned out to have disturbed gas kinematics. Mergers and tidal processes such as harassment are capable of causing disturbances also in stellar velocity fields (Moore et al. 1999; Mihos 2004). ICM-related processes on the other hand, even ram-pressure stripping are insufficient to be able to affect stellar kinematics of spiral galaxies (Quilis et al. 2000). Some attempts have been made to evaluate the effectiveness of the interaction processes as a function of location in the galaxy cluster. Dale et al. (2001) measured Tully-Fisher Relation (TFR) residuals for 510 cluster spirals and concluded that they do not show a dependence on distance from the cluster center. Moran et al. (2007b) constructed the TFR in both K_S and V bands for 40 cluster, 37 field spirals at intermediate redshift and found that the cluster TFR exhibits significantly larger scatter than the field relation in both bands and the residuals do not show a clear trend with R/R_{vir}. They found that the TFR residuals do not correlate with the star formation rate and dust content. They also checked whether central surface mass density of galaxies, which can be used to probe the action of harassment, shows a trend as a function of radius. They found that it shows a break at approximately $1R_{vir}$, outside of which spirals exhibit nearly uniformly low central density values. They argue that a combination of merging in the cluster outskirts with harassment in the intermediate and inner cluster regions might ex-

plain both the TFR scatter and the radial trend in density which persist up to $2R_{vir}$.

As discussed above, galaxy evolution in clusters is rather complex, since there are several interaction mechanisms involved. To understand the nature of these mechanisms, it is important to examine together morphological and kinematical properties of cluster galaxies. In this series of papers we make use of both gas velocity fields and high resolution images of galaxies in four intermediate-redshift clusters and their field to do that. Most studies in the literature rely on long-slit data for identifying kinematical disturbances. Using a velocity map enables us to have a more accurate measure of the kinematical (ir)regularity. A velocity field can be decomposed into velocity, position angle and inclination of circular orbits at each radius (see Krajnović et al. 2006). The deviation of the kinematic major axis (KMA) around its mean value and the misalignment between KMA and the photometric major axes (PMA) both indicate kinematical disturbance. We also make a simple rotating model that has the mean position angle and inclination of the observed velocity map. The residual of the observed and the simple rotating map is fitted with high order Fourier terms and the squared sum of these terms is used as another indicator. We measure these irregularity indicators for both field galaxies and cluster members and compare them with each other to search for the environmental imprint on gas kinematics. We then combine this information with the morphological and photometric properties of these galaxies and investigate whether certain characteristics make galaxies more sensitive to environmental effects. We also use the relations between intrinsic galaxy properties and efficiency of interaction processes, that are known from theory, to investigate which mechanisms are at work on the cluster galaxies in our sample.

We also investigate the evolution of field galaxies by studying their gas kinematics as a function of redshift. We measure the irregularities in their gas kinematics both at intermediate redshifts and in the local universe and compare them with each other. These results are then compared with the studies of spatially resolved gas kinematics at similar or higher redshifts: Shapiro et al. (2008, hereafter S08) analyzed gas velocity fields and velocity dispersion maps of 11 galaxies at $z \sim 2$, observed with SINFONI, and classified these systems into two categories: merging and non-merging. They found that more than 50% of these galaxies are consistent with a single rotating disk interpretation. With FLAMES at the VLT, Yang et al. (2008, hereafter Y08) studied 63 intermediate-mass field galaxies at $0.4 < z < 0.75$. Using spatially resolved gas kinematics of these objects, ($2'' \times 3''$ field of view) they find that both velocity fields and velocity dispersion maps of 26% of these galaxies are incompatible with disk rotation.

Spatially resolved velocity fields are essential for quantifying irregularities in the kinematics. Because the inclination and the position angle of the orbits at each radii can be assessed and the velocity profile along each orbit can be analyzed and compared with a simple rotating case. For Tully-Fisher studies the main problem with the long slit data is the fact that it can be misleading in case the kinematic and photometric axes are misaligned. The conventional way of obtaining the spatially resolved spectra is using integral field (IFU) spectroscopy (e.g. S08, Y08, Puech et al. 2008). We use another approach and place three parallel, adjacent VLT/FORS2 slits on each galaxy. This novel method has the advantage that we can explore the velocity fields up to large radii ($\approx 3''$, which corresponds to 16 kpc at z= 0.4) and it is more efficient than IFUs in terms of observing time. The spatial sampling along the minor and major axes is $1''$

Table 1. Basic galaxy cluster information.

name	z	ref	R_{vir} (h^{-1} Mpc)	ref	σ kms^{-1}	ref	L_X ($10^{44} ergs^{-1}$)	ref	dynamical state	ref	N
MS 0451.6-0305	0.540	(1)	1.17	(5)	1371	(7)	10.19	(10)	relatively relaxed	(12)	4
MS 2137.3-2353	0.313	(2)	1.95	(6)	960	(9)	7.97	(10)	relaxed	(13)	5
MS 1008.1-1224	0.3061	(3)	1.18	(5)	1042	(8)	2.29	(10)	non-relaxed	(14)	5
Cl 0412-65	0.507	(4)	0.62	(5)	700	(4)	0.16	(11)			2

References: (1): (Donahue 1996b); (2): (Stocke et al. 1991); (3): (Yee et al. 1998); (4): (Dressler et al. 1999); (5): (Girardi & Mezzetti 2001); (6): (Allen et al. 2003); (7):(Carlberg et al. 1996); (8):(Borgani et al. 1999); (9):(Kneib et al. 1995); (10): (Luppino et al. 1999); (11): (Smail et al. 1997); (12): (Donahue 1996a); (13): (Jeltema et al. 2005); (14): (Athreya et al. 2002).
The last column (N) gives the number of galaxies in each cluster that are used in the kinematical analysis.
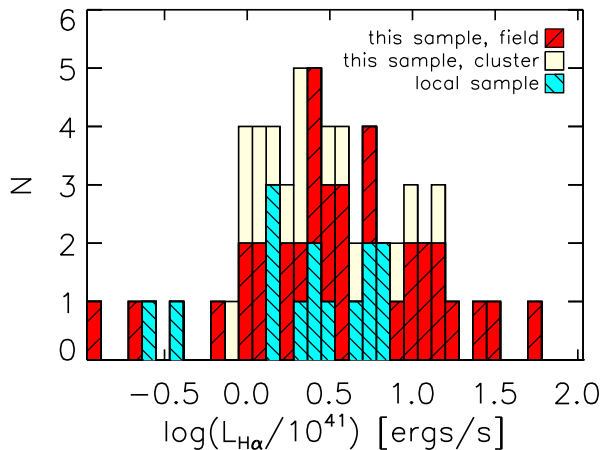
Fig. 1. Distribution of H_α luminosities of both our galaxies and a local sample from SINGS.

and 0.″25 respectively. We described our method and presented the analysis of our MS 0451 sample in Kutdemir et al. (2008, hereafter Paper III). Here, we include in our analysis galaxies in three more intermediate redshift clusters and their field. A plan of the paper follows. In Sect. 2, we describe our sample and the improvements in our data reduction technique in comparison with Paper III. In Sect. 3, we explain the analysis of the data. In Sect. 4, we discuss our results and compare them with the literature. Sect. 5 summarizes the results and our conclusions.

Throughout this paper, we assume that the Hubble constant, the matter density and the cosmological constant are $H_0 = 70$ km s^{-1} Mpc^{-1}, $\Omega_m = 0.3$ and $\Omega_\lambda = 0.7$ respectively (Tonry et al. 2003).

2. Sample and data properties

2.1. Sample

Our sample includes four galaxy clusters which have different properties (Table 1). To be able to compare the galaxies that experience similar environmental conditions, we scale cluster-centric distance by each cluster's virial radius. It is known that even galaxy clusters at the same redshift can be very different from one another. Two well-studied rich clusters in the local universe, Coma and Virgo are a good example for that. While Coma is dynamically relaxed and spiral poor, Virgo on the contrary is unrelaxed and spiral rich (Poggianti 2006).

Here we give some information about each cluster in our sample: MS 0451 is a massive cluster with very high X-ray luminosity. 28% of its spiral population are passive (Moran et al. 2007a); MS 1008 is a very regular and rich cluster (Lewis et al.

1999; Luppino et al. 1999); MS 2137 is a rich and dynamically relaxed cluster (Jeltema et al. 2005); Cl 0412 (F1557.19TC) is a poor cluster that is not well-studied. Our cluster selection depended on the availability of their HST/WFPC2 imaging when the project was initiated in 1999. See Ziegler et al. 2003, hereafter Paper I and Jäger et al. 2004, hereafter Paper II for more detailed information about the sample selection.

During the target selection, we gave priority to galaxies from our previous studies, both in field and cluster environments, that have detectable emission lines for extracting velocities. Further objects were drawn from a catalog provided by the CNOC survey (Ellingson et al. 1998) with either redshift information or measured (g-r) color that matches expectations for spiral templates at $z \approx 0.5$. If there was an unused slitlet in the MXU setup, and no suitable candidate was available, a galaxy was picked at random. For our analysis, we also use a sample from SINGS as a local reference for comparison (see Paper III). SINGS galaxies are a diverse set of local normal galaxies (Kennicutt et al. 2003). Daigle et al. (2006)'s subsample that we use in our analysis consists of galaxies that have star forming regions, so that their H_α kinematics could be extracted. We excluded from our analysis the galaxies in this sample that have luminosities that are very different from the luminosities of our intermediate redshift sample, so that the two samples have comparable stellar masses. In Fig. 1, we compare the H_α luminosities of galaxies in our sample and in the local sample. H_α luminosities of the galaxies in our sample were calculated using the available emission lines in their spectra as explained in Sect. 3.3. Since the galaxies in our sample were selected mainly based on the strength of their emission, several of them have larger H_α luminosities, and therefore, higher star formation rates than the galaxies of the local sample. This raises the question whether our sample is biased towards disturbed galaxies, since perturbations are expected to trigger star formation and consequently increase the strength of emission lines. The Kolmogorov-Smirnov (K-S) test of these distributions does not indicate a significant difference between the H_α luminosities of the two samples (Table 2). However, we check our results by repeating the analysis for a subsample that is in the same H_α luminosity interval as the local sample.

We presented the analysis of our MS 0451 sample in Paper III. We give the basic information about the rest of the sample in Table 3. The first character of a galaxy name indicates the sample (1:MS 0451 ; 2:MS 1008 ; 3:MS 2137 ; 4:Cl 0412). The second character is "C" for cluster members and "F" for field galaxies. The last part of the name assigns a number to each galaxy. We identified galaxies with redshifts between 3σ below and above the cluster redshifts as cluster members. Only for MS 0451, which was analyzed in Paper III, we used the redshift interval defined by Moran et al. (2007b) using the redshift distribution of over 500 objects. That gives an interval which

Table 2. K-S statistics of H_α luminosities of our sample and the local sample.

	D	P
log(H_α luminosity)	0.23	0.580

D: K-S statistics specifying the maximum deviation between the cumulative distribution of the H_α luminosity for the local and intermediate redshift samples; P: significance level of the K-S statistics.

is $\Delta z = 0.006$ larger on both sides than what the 3σ definition gives. For Cl 0412, Dressler et al. (1999) determined cluster membership using the redshift distribution of 22 galaxies. The redshift interval they define selects the same galaxies as the 3σ criterion to be cluster members.

In Sect. B in the Appendix, we give some information about each galaxy. In case the galaxy has emission lines, we present:

a– the HST-ACS image of the galaxy in the $F606W$ (broad V band filter);

b– rotation curves of different emission lines (and for some cases based on the absorption lines) extracted along the central slit without correction for inclination and seeing;

c– position angles of kinematic and photometric axes as a function of radius;

d– rotation curves extracted along the central slit and the kinematic major axis;

e– velocity field obtained using the strongest line in the spectrum;

f– normalized flux map of the line used for constructing the velocity field;

g– velocity map reconstructed using 6 harmonic terms;

h– residual of the velocity map and the reconstructed map;

i– simple rotation map constructed for position angle and ellipticity fixed to their global values;

j– residual of the velocity map and the simple rotation model;

k– position angle and flattening as a function of radius;

l– k_3/k_1 and k_5/k_1 (from the analysis where position angle and ellipticity are fixed to their global values) as a function of radius.

2.2. Spectroscopic data

Our observations were spread across 5 nights in October and November 2004 for Cl 0412 (seeing $0''\!.57$ (*FWHM*)); 7 nights in December 2004 and February 2005 for MS 1008 (seeing $0''\!.73$); 5 nights between May and July 2005 for MS 2137 (seeing $0''\!.76$). Each sample was observed using three masks and the integration time of each mask was split into three exposures. Even in cases where all three exposures were taken during the same night, the frames were not perfectly aligned, therefore, we completed the reduction of each frame before combining them.

The spectral data reduction was done in the same way as explained in Paper III, apart from using a different sky subtraction method, which improved the results considerably. In Paper III, the sky is modelled in spectra that are interpolated along the X axis for wavelength calibration. Here we use the algorithm described in Kelson (2003) which is based on modelling the sky in the original data frame as a function of the rectified coordinates. Modelling the sky before applying any rectification/rebinning to the data reduces the amount of noise that is introduced to the data during the sky-subtraction process (see also Milvang-Jensen et al. 2008). To quantify the difference, we

reduced one of our spectra using both the old and the new methods. We averaged 15 spatial rows, that are far from the galaxy spectrum, and therefore include sky-line residuals only. A third order polynomial was fitted to and then subtracted from this distribution across the wavelength axis and the root mean square of the counts was calculated for both spectra. A comparison of the two shows that the noise is 30% less in case we use the new sky subtraction method.

To be able to compare the H_α emission line fluxes of our sample with the local sample, we applied a rough flux calibration to our data. We used the spectrum of a star that we observed together with our MS 0451 sample for the calibration of all our data, since they were observed with the same instrument. The star that we used is $U0825\_01208341$ in the PMM USNO-A2.0 catalogue of Monet et al. (1998). We transformed the B and R magnitudes of the star given in the catalog onto the standard Johnson-Cousins system using the conversions provided by Kidger (2003).

2.3. Photometric data

Environmental effects on how a galaxy evolves depend on its intrinsic properties. For example it is known that harassment is more efficient on low central surface mass density galaxies (Moore et al. 1999). In this context, it is important to test whether the abnormalities that we see in gas kinematics of a galaxy correlate with its photometrical properties. To investigate this issue, we use both VLT/FORS2 and HST/ACS images. We obtained imaging of the MS 1008, MS 2137 and Cl 0412 samples in the ACS/$F606W$ filter while we exploited existing imaging of MS 0451 in the ACS/$F814W$ filter from the ST−ECF HST archive. Ground based images were taken in the B, V, R and I filters for the whole sample. The FORS2 filters B, V and I are close approximations to the Johnson-Cousins (Bessell 1990) photometric system while the R filter is a special filter for FORS2 that is similar to the Cousins R [1].

3. Analysis

3.1. Photometry

Surface photometry analysis, magnitude measurements, extinction and k-correction were done in the same manner as explained in Paper III. We have not applied an internal dust (inclination) correction. Galactic extinction and k-corrected M_B magnitudes, rest-frame $B − V$, $V − R$ and $R − I$ colors of the galaxies in our sample are given in Table C.1 in the Appendix. k-correction was done using the kcorrect algorithm by Blanton & Roweis (2007).

Abraham et al. (1994) defined concentration and asymmetry parameters to be able to do the morphological classification of galaxies in a quantitative and automated way. The first parameter quantifies how concentrated the light distribution of an object is, and it is larger for earlier type galaxies. The second parameter measures how asymmetric the light distribution of a galaxy is and becomes larger for later type galaxies. We use slightly different definitions for asymmetry and concentration parameters than in Paper III. Here we give the new definitions that are based on Abraham et al. (1996) and Conselice et al. (2000). The concentration is the ratio of the flux within G_1, the area inside the

---

[1] The FORS2 filter curves are given at http://www.eso.org/instruments/fors/inst/Filters/curves.html

Table 3. Basic galaxy information.

ID (1)	z (2)	d (3)	NED name (4)	Type (5)	Type-Ref. (6)	Type (7)	z (8)	z-Ref. (9)
2C1	0.2958	0.7	PPP 001575	Sb-Sc	1	Irr/Pec	0.2968	1
2C2	0.3115	1.0	PPP 001149	Sb-Sc	1	S/Pec	0.2963	1
2C3	0.3024	0.9	PPP 000726	Sb-Sc	1	S	0.3026	1
2C4	0.2975	0.6	–	–		Irr/Pec	–	
2C5	0.2981	0.2	PPP 000847	Sc-Irr	1	Irr/Pec	0.2935	1
2C6	0.3121	0.1	[SED2002] 049	–		Irr/Pec	–	
2C7	0.3136	0.9	PPP 000596	Sc-Irr	1	Irr/Pec	0.3120	1
2C8	0.3164	0.9	PPP 001521	Sb-Sc	1	Irr/Pec	0.3176	1
2C9	0.3082	0.7	PPP 001560	E	1	E	0.3076	1
2C10	0.3093	0.9	PPP 001378	E	1	S0/E	0.3077	1
2C11	0.3049	0.8	PPP 001673	E	1	S	0.3049	1
2C12	–	0.7	FPG 0100 NED02	E	1	S	0.3134	1
2F1	0.6792	–	–	–		Irr/Pec	–	
2F2	0.2082	–	–	–		S/S0	–	
2F3	0.6809	–	–	–		Irr/Pec	–	
2F4	0.6857	–	–	–		S	–	
2F5	0.4642	–	PPP 000566	–		S0	0.4644	4
2F6	0.1669	–	PPP 001815	Sc-Irr	1	S	0.1675	1
2F7	0.4021	–	–	–		Irr/Pec	–	
2F8	0.6781	–	–	–		Irr/Pec	–	
2F9	0.4352	–	–	–		Irr/Pec	–	
2F10	0.3632	–	FPG 0100 NED01	Sc-Irr	1	Irr/Pec	0.3645	1
2F11	0.3618	–	PPP 001627	–		S	0.3623	4
2F12	0.3220	–	PPP 000772	Sc-Irr	1	S	0.3216	1
2F13	–	–	–	–		Irr/Pec	–	
2F14	–	–	–	–		Irr/Pec	–	
2F15	–	–	–	–		–	–	
2F16	–	–	–	–		–	–	
2F17	–	–	–	–		Irr/Pec	–	
2F18	0.1413	–	–	–		E	–	
2F19	0.0052	–	–	–		S0	–	
2F20	0.4247	–	PPP 001823	–		S	0.4256	4
2F21	0.2381	–	–	–		S0	–	
3C1	0.3095	0.7	–	–		S	–	
3C2	0.3152	0.7	[SED2002] 072	–		Irr/Pec	–	
3C3	0.3095	0.7	[SED2002] 065	–		S	–	
3C4	0.3164	0.2	[SED2002] 009	–		S	–	
3C5	0.3172	1.0	–	–		S	–	
3C6	0.3155	0.7	–	–		Irr/Pec	–	
3C7	0.3230	0.9	–	–		S	–	
3C8	0.3137	0.9	–	–		S0	–	
3C9	0.3141	0.9	–	–		S	–	
3F1	0.4528	–	–	–		S/Pec	–	
3F2	0.1501	–	–	–		Irr/Pec	–	
3F3	0.1951	–	–	–		Irr/Pec	–	
3F4	0.5675	–	[SED2002] 069	–		Irr/Pec	–	
3F5	0.2859	–	–	–		Irr/Pec	–	
3F6	0.2822	–	–	–		Irr/Pec	–	
3F7	0.1876	–	–	–		S	–	
3F8	0.5037	–	[SED2002] 053	Irr	2	S	–	
3F9	0.1880	–	[SED2002] 141	–		Irr/Pec	–	
3F10	0.7498	–	–	–		E	–	
3F11	0.8872	–	–	–		S0	–	
3F12	–	–	[SED2002] 121	–		E	–	
3F13	0.4421	–	[SED2002] 104	E/S0	2	S	–	
4C1	0.5027	0.1	–	–		S	–	
4C2	0.5085	1.3	–	–		Irr/Pec	–	
4C3	0.5099	0.6	–	–		Irr/Pec	–	
4F1	0.2918	–	–	–		Irr/Pec	–	
4F2	0.8478	–	–	–		S/Pec	–	
4F3	0.8916	–	–	–		Irr/Pec	–	
4F4	0.3599	–	[DSP99] 024	–		Irr/Pec	0.3600	3
4F5	0.6073	–	–	–		S	–	
4F6	0.6071	–	[DSP99] 017	Sc	3	S	0.6060	3
4F7	0.6083	–	[DSP99] 023	–		Irr/Pec	0.6080	3
4F8	0.4335	–	[DSP99] 022	–		S	0.4331	3
4F9	0.4737	–	[DSP99] 021	–		Irr/Pec	0.4738	3
4F10	0.5478	–	–	–		Irr/Pec	–	
4F11	–	–	–	–		Irr/Pec	–	
4F12	0.5481	–	–	–		S	–	
4F13	0.4993	–	–	–		Irr/Pec	–	
4F14	0.5646	–	–	–		S	–	

Column (1): object ID; Col. (2): redshift; Col. (3): projected distance from the cluster center in Mpc; Col. (4): name of the galaxy in Nasa Extragalactic Database (NED); Col. (5): morphological type of the galaxy; Col. (6) the reference for the morphological type; Col. (7): eye-ball morphological classification (this paper); Col. (8): redshift of the galaxy; Col. (9) the reference for the redshift.
References: (1): (Yee et al. 1998);(2): (Stanford et al. 2002);(3): (Dressler et al. 1999); (4): (Jäger et al. 2004). NED names given in column (4) begin with "MS 1008.1-1224:", "MS 2137.3-2353:" and "F1557.19TC:" for object IDs in the first column that begin with "2", "3" and "4" respectively. For galaxies 2F13, 2F14, 2F17, 2F15, 2F16, 3F12 and 4F11 the redshift could not be determined. Different possibilities for identification of the emission line visible in their spectra rules out that these galaxies are cluster members.

Table 4. Eye-ball morphological classification of the MS 0451 sample.

ID	1C1	1C2	1C3	1C4	1C5	1C6	1C7	1C8	1C9	1C10	1C11
Type	S	S	S/S0	S	S0	Irr/Pec	S	Irr/Pec	Irr/Pec	Irr/Pec	E
ID	1F1	1F2	1F3	1F4	1F5	1F6	1F7	1F8	1F9	1F10	1F11
Type	Irr/Pec	S	Irr/Pec	Irr/Pec	S	S	Irr/Pec	S	S0	Irr/Pec	Irr/Pec
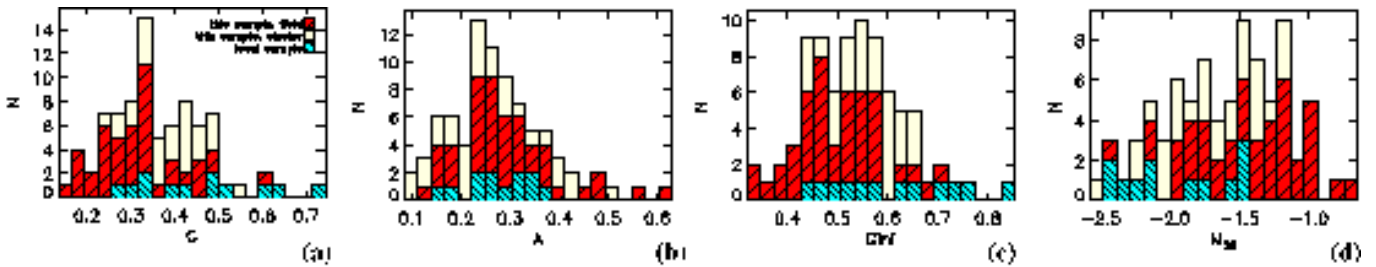
Fig. 2. Distribution of morphological parameters for our sample and the local sample. a: Concentration parameter. b: Asymmetry parameter. c: Gini coefficient. d: M_{20} index.

1σ isophote of the sky level and G_2, the region which has the same axis-ratio as G_1, but has a major-axis size that is 0.3 times the major-axis size of G_1:

$$C = \frac{\sum_{i,j \in G_2} I_{ij}}{\sum_{k,l \in G_1} I_{kl}} \cdot \tag{1}$$

The asymmetry parameter A is the normalized residual of a galaxy image and its 180 degrees rotated counterpart. It is calculated within the 1σ isophote of the galaxy (Eq. 2). The central pixel for the asymmetry measurement is determined by shifting the galaxy on a 50×50 grid and finding the minimum A. The asymmetry of a blank area was measured in the same way in the vicinity of the object to correct for the contribution of the background noise.

$$A = \left(\frac{\sum_{i,j} |I(i,j) - I_{180}(i,j)|}{\sum_{i,j} |I(i,j)|} \right) - \left(\frac{\sum_{k,l} |B(k,l) - B_{180}(k,l)|}{\sum_{i,j} |I(i,j)|} \right) \cdot \tag{2}$$

We measure two additional parameters that we did not use in Paper III: the Gini coefficient and the M_{20} index (Abraham et al. 2003; Lotz et al. 2004). The Gini coefficient quantifies the non-uniformity in the light distribution and strongly correlates with the concentration index for local galaxies. Since the Gini coefficient has no dependence on the definition of the center of an object (Eq. 3), it is often used as an alternative to the concentration parameter in studies of high-redshift galaxies, a large fraction of which are peculiar.

$$G = \left(\frac{1}{|\bar{f}| n(n-1)} \right) \sum_{i=1}^{n} (2i - n - 1)|f_i|, \tag{3}$$

where $|f_i|$ are the absolute flux values of a galaxy's constituent pixels sorted in increasing order, $|\bar{f}|$ is their mean value and n is the number of pixels.

The M_{20} index is based on the total second-order moment M_{TOT}, which is the flux in each pixel f_i multiplied by its squared distance to the galaxy center, summed over all pixels of the galaxy (Eq. 4).

$$M_{TOT} = \sum_{i=1}^{n} M_i = \sum_{i}^{n} f_i((x_i - x_c)^2 + (y_i - y_c)^2) \cdot \tag{4}$$
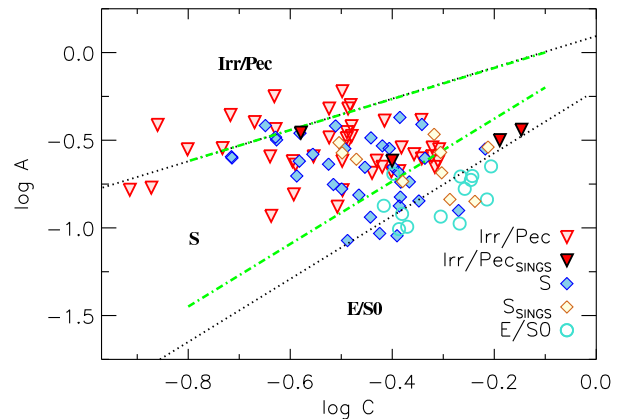
Fig. 3. Distribution of galaxies in our sample and a local sample from SINGS on the $A - C$ plane. Their morphological types, that are determined by our eye-ball classification (Table 3, Col.7.), are indicated with different symbols as shown in the legend. The dash-dotted green lines are the selection limits separating different morphological types determined by Menanteau et al. (2006). The borders that are adjusted by minimizing the amount of contamination from different types in each region are shown with black dotted lines.

x_c and y_c are the coordinates of the galaxy center which are determined in a way to minimize M_{TOT}. M_{20} is the normalized second order moment of the brightest 20% of the galaxy's flux (Eq. 5). To compute M_{20}, the pixels are ordered such that i increases with decreasing flux, and M_i is summed over the brightest pixels until the integrated value reaches 20% of the total galaxy flux:

$$M_{20} = log\left(\frac{\sum_i M_i}{M_{tot}}\right) while \sum_i f_i < 0.2 f_{tot} \cdot \tag{5}$$

M_{20} correlates with the square of the distance of the brightest regions of a galaxy from its center, which makes it sensitive to merger signatures. M_{20} is smaller for centrally concentrated objects (early types) and increases in case of off-center light concentrations, spiral arms, bright nuclei, bars, etc.

We present the asymmetry, concentration, Gini and M_{20} parameters of our galaxies in Table C.1 in the Appendix. The same

Table 5. Photometric parameters for the SINGS sample.

ID	A	C	G	M_{20}
(1)	(2)	(3)	(4)	(5)
NGC0628	0.31	0.31	0.45	-1.54
NGC3031	0.18	0.42	0.57	-2.33
NGC3049	0.27	0.50	0.76	-2.29
NGC3184	0.27	0.32	0.53	-1.45
NGC3521	0.29	0.61	0.70	-2.41
NGC3938	0.34	0.48	0.66	-1.83
NGC4536	0.25	0.34	0.50	-1.50
NGC4569	0.21	0.50	0.65	-1.88
NGC4579	0.14	0.58	0.70	-2.48
NGC4625	0.36	0.71	0.74	-1.81
NGC4725	0.24	0.40	0.54	-2.41
NGC5055	0.15	0.52	0.63	-2.13
NGC5194	0.35	0.26	0.47	-1.42
NGC5713	0.32	0.65	0.83	-2.13

Column (1): object ID; Col. (2): asymmetry index; Col. (3): concentration index; Col. (4): Gini coefficient; Col. (5): M_{20} index.
We could not obtain reliable measurements of the photometric parameters of NGC3621, NGC4236, NGC2976 and NGC7331 because of the large number of stars and artifacts on the images, therefore they are not used in our analysis.

Table 6. K-S statistics of the morphological parameters of our sample and the local sample.

	D	P
distant galaxies: cluster versus field		
M_{20}	0.36	0.013
Gini	0.46	0.000
A	0.31	0.048
C	0.50	0.000
field galaxies: distant versus local		
M_{20}	0.50	0.011
Gini	0.43	0.048
A	0.18	0.898
C	0.48	0.017

D: K-S statistics specifying the maximum deviation between the cumulative distribution of the morphological parameters for distant galaxies: cluster versus field and for field galaxies: distant versus local; P: significance level of the K-S statistics. In this analysis, only the galaxies for which spectroscopic redshifts are available (see Table 3 here and Table 1 in Paper III) and that are late morphological types (spiral/irregular) according to our eye-ball classification (see Table 3 and Table 4) were used. Galaxy 2F19 was also excluded since it is not distant ($z = 0.0052$).

parameters for the SINGS galaxies are given in Table 5. We applied a K-S test to the asymmetry, concentration, Gini and M_{20} distributions of the local versus distant field samples as well as the distant cluster versus field samples. Only the galaxies for which we have spectroscopic redshifts (see Table 3 here and Table 1 in Paper III) and that were classified as late types (spiral or irregular) according to our eye-ball classification (Table 3 and Table 4) were used in this analysis. Galaxy 2F19 was also excluded since it is not distant ($z = 0.0052$). The results are given in Table 6 and the distributions are shown in Fig.2. The distant cluster and field samples have significantly different distributions for the concentration, Gini and M_{20} parameters. For the asymmetry, the difference between the two samples is considerable, but not very significant. The distributions of the local and distant field samples are significantly different for the M_{20} and concentration parameters. The difference is large for the Gini coefficient while the significance level of the statistic is not very high. The asymmetry distributions are similar for the two samples.

The rest-frame wavelength of the ACS images of our sample corresponds to the B band, therefore we used blue KPNO, CTIO, Palomar and Isaac Newton images of the SINGS galaxies for the measurements. These images were convolved with a point spread function and then rebinned to have the same seeing and pixel size in kpc as the HST images of our sample at the mean redshift of our clusters ($z = 0.4$). The asymmetry and concentration parameters can be used for morphological classification. We present our galaxies and local galaxies from SINGS on the $A - C$ plane together with our eye-ball classification of their morphologies in Fig. 3. Selection limits which separate different morphological types on the plane, as determined by Menanteau et al. (2006), are shown on top of this plot. The borders are then adjusted by minimizing the amount of contamination from different types in each region.

3.2. Kinematics

We analyze the gas kinematics of our whole sample in the way that was described in Paper III, using a sample from SINGS as a local reference for comparison (see Paper III). As stated in

the introduction section, we look for indications of disturbance in velocity fields to be able to examine environmental effects. There are three parameters that we use for quantifying these abnormalities:

a– the standard deviation of the kinematic position angle (σ_{PA});
b– the average misalignment between the photometric and kinematic axes ($\Delta\phi$);
c– the mean deviation of the velocity field from a simple rotating disk ($k_{3,5}/k_1$).

The line of sight (LOS) velocity profile of a simple rotating disk is a cosine function (Krajnović et al. 2006). Our last (ir)regularity parameter measures the deviation from the cosine form that can be represented with the third and the fifth order terms of the Fourier series. The exact definition of each of the (ir)regularity parameters is given in Paper III. Their values for each galaxy are listed in Table 7. Examination of the data shows that in some special cases these measurements have to be excluded from the analysis (explained in Sect. 3.8).

3.3. Star Formation Rates

Here we analyze the star formation properties of the galaxies in our sample. We use the total fluxes of available emission lines in the spectra to measure the star formation rates (SFR). The luminosities are calculated using these fluxes and corrected for extinction following Tully & Fouqué (1985). The inclinations are measured from our HST/ACS imaging (Table C.2). For a comparison between different extinction corrections, we have applied the definitions of Giovanelli et al. (1994) and Tully et al. (1998), which makes a factor of 10% difference at most in SFRs. Tully & Fouqué (1985) better matches the extinction law (Cardelli et al. 1989) for reasonable values of E(B-V). Star formation rates that rely on [OII]3727 or H_α line were calculated applying Kennicutt (1992) and for H_β, case B recombination was assumed, which implies a factor 2.86 difference in comparison with H_α. Note that we have not corrected the H_β luminosities for underlying stellar absorption. For the calculations based on [OIII]5007 we have followed Maschietto et al. (2008) and Teplitz et al. (2000).

Table 7. Parameters quantifying the (ir)regularity of the gas kinematics measured for our sample.

ID (1)	$R_{\max}$ (2)	σ_{PA} (3)	$\Delta\phi$ (4)	$k_{3,5}/k_1$ (5)	V_{asym} (6)
1C7	13.8	23	68 ± 26	0.32 ± 0.20	0.25 ± 0.08
1C8	20.9	2	9 ± 6	0.06 ± 0.05	0.08 ± 0.02
1C9	9.2	19	66 ± 20	0.10 ± 0.03	0.13 ± 0.02
1C10	11.7	9	14 ± 9	0.26 ± 0.08	0.19 ± 0.08
1F2	10.5	2	35 ± 37	0.08 ± 0.02	0.08 ± 0.02
1F3	10.0	7	39 ± 9	0.07 ± 0.05	0.05 ± 0.02
1F4	5.5	21	18 ± 20	0.30 ± 0.19	0.21 ± 0.10
1F5	11.3	5	46 ± 9	0.08 ± 0.03	0.09 ± 0.03
1F6	4.4	29	57 ± 44	0.27 ± 0.18	0.20 ± 0.21
1F7	14.1	3	0 ± 11	0.05 ± 0.02	0.06 ± 0.01
1F10	8.4	8	1 ± 7	0.25 ± 0.05	0.23 ± 0.10
1F11	1″7	5	18 ± 5	0.05 ± 0.02	0.20 ± 0.16
2C3	9.7	21	47 ± 60	0.11 ± 0.04	0.10 ± 0.04
2C5	7.5	5	38 ± 37	0.06 ± 0.06	0.02 ± 0.02
2C6	8.8	15	84 ± 14	0.10 ± 0.03	0.12 ± 0.04
2C7	8.3	6	61 ± 18	0.09 ± 0.09	0.03 ± 0.02
2C8	7.6	4	77 ± 17	0.16 ± 0.08	0.11 ± 0.05
2F1	14.2	6	73 ± 5	0.06 ± 0.03	0.08 ± 0.04
2F2	4.2	6	72 ± 34	0.09 ± 0.08	0.12 ± 0.14
2F3	14.4	17	1 ± 34	0.12 ± 0.05	0.17 ± 0.08
2F4	8.0	7	24 ± 35	0.06 ± 0.01	0.07 ± 0.03
2F5	11.3	37	4 ± 36	0.06 ± 0.01	0.10 ± 0.07
2F6	4.6	9	62 ± 13	0.13 ± 0.08	0.11 ± 0.06
2F9	7.4	8	22 ± 8	0.18 ± 0.13	0.17 ± 0.12
2F10	11.6	7	37 ± 10	0.09 ± 0.04	0.11 ± 0.03
2F11	17.0	43	29 ± 49	0.83 ± 0.83	1.05 ± 1.86
2F12	11.4	3	30 ± 36	0.07 ± 0.02	0.05 ± 0.02
2F15&16	1″9	19	–	0.77 ± 0.50	2.38 ± 6.15
3C3	12.2	4	3 ± 4	0.17 ± 0.11	0.13 ± 0.05
3C4	12.7	8	1 ± 9	0.15 ± 0.05	0.08 ± 0.03
3C5	7.5	7	84 ± 7	0.07 ± 0.03	0.11 ± 0.10
3C6	6.5	11	52 ± 8	0.10 ± 0.07	0.18 ± 0.11
3C7	8.8	3	46 ± 2	0.09 ± 0.05	0.20 ± 0.13
3F3	3.7	5	48 ± 5	0.11 ± 0.02	0.10 ± 0.07
3F6	6.7	3	55 ± 3	0.16 ± 0.18	0.15 ± 0.13
3F7	4.8	9	97 ± 25	0.06 ± 0.04	0.06 ± 0.03
3F8	13.2	4	17 ± 37	0.20 ± 0.05	0.30 ± 0.43
3F9	7.7	9	46 ± 9	0.13 ± 0.02	0.13 ± 0.11
4C2	7.4	3	65 ± 2	0.08 ± 0.01	0.07 ± 0.04
4C3	8.9	13	63 ± 12	0.22 ± 0.14	0.14 ± 0.03
4F3	15.0	9	40 ± 20	0.07 ± 0.03	0.14 ± 0.03
4F4	10.8	8	60 ± 9	0.82 ± 1.21	0.57 ± 0.64
4F5	16.5	9	17 ± 32	0.07 ± 0.04	0.04 ± 0.02
4F6	10.7	6	28 ± 31	0.12 ± 0.05	0.09 ± 0.04
4F7	27.5	29	7 ± 53	0.20 ± 0.06	0.17 ± 0.05
4F8	14.5	18	39 ± 31	0.18 ± 0.09	0.10 ± 0.03
4F9	8.7	3	55 ± 3	0.07 ± 0.05	0.05 ± 0.02
4F12	6.4	12	24 ± 18	0.29 ± 0.16	0.17 ± 0.07
4F13	9.1	2	53 ± 6	0.10 ± 0.11	0.04 ± 0.03

Column (1): object ID; Col. (2): maximum radius for which the kinematic parameters could be calculated. The conversion from arcsecond into kpc was done as explained in Wright (2006); Col. (3): standard deviation of the kinematic position angle (σ_{PA}); Col. (4): mean misalignment between the kinematic and photometric position angles ($\Delta\phi$); Col. (5): mean $k_{3,5}/k_1$ of the analysis done while fixing the position angle and the ellipticity to their global values; Col. (6): V_{asym} parameter of S08 measured as described in Sect. 4.6. The error is the standard deviation of the parameter in the range of observations.
For 1F11 and 2F15&16, the spectroscopic redshifts are not available, therefore we give $R_{\max}$ of these objects in arcseconds. $k_{3,5}/k_1$ of galaxy 1F5, $\Delta\phi$ of the galaxies that have $\epsilon \leq 0.1$ (galaxies 1F2, 2F4, 2F12 and 4C3) and all parameters for galaxies 1F10, 2F5, 2F11 and 2F15&16 are rather meaningless as explained in Paper III for the MS 0451 sample and here, in Sect. 3.8 for the rest, therefore they are excluded from the analysis.
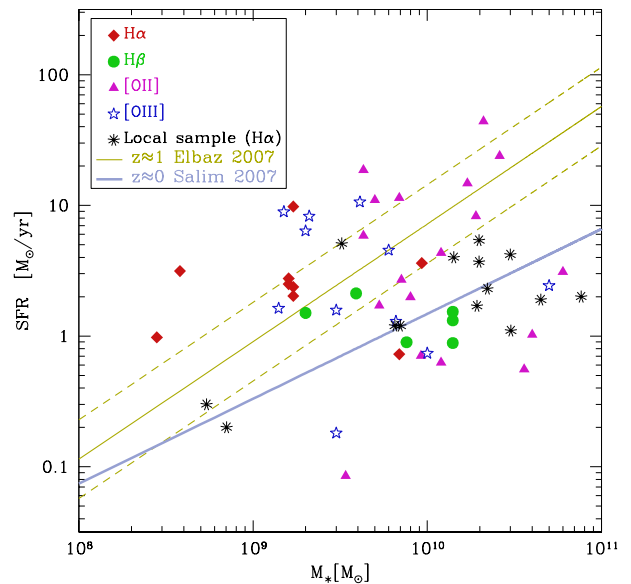

Fig. 4. SFR versus stellar mass for our sample and the local sample from SINGS. The SFR-stellar mass relation based on $z \sim 1$ galaxies from GOODS Elbaz et al. (2007) and the local relation from Salim et al. (2007) are overplotted for comparison. The stellar masses of the SINGS galaxies are calculated using their M_B and B-V as explained in Bell et al. (2005).
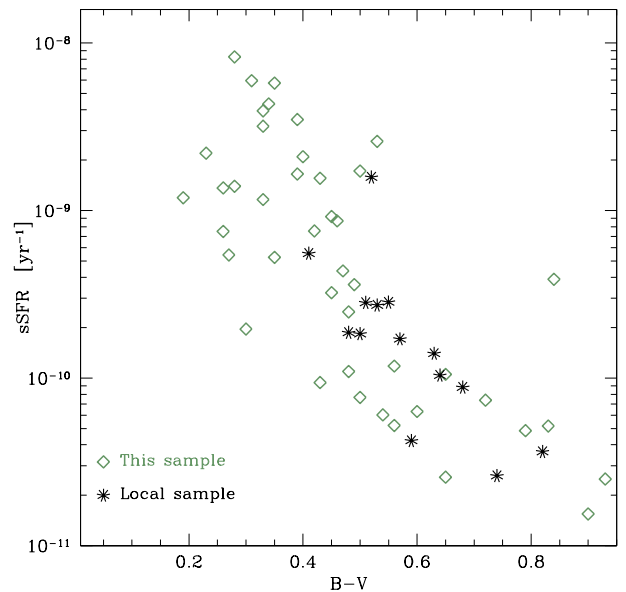

Fig. 5. Specific star formation rate versus rest-frame B-V color for our sample and the local sample from SINGS.

In Fig.4, we plot the SFR versus stellar mass for the galaxies in our sample. A comparison with the relations for $z \sim 1$ and $z \sim 0$ galaxies and the SINGS local sample shows that SF properties of the galaxies in our sample cover a wide range and some galaxies have higher star formation rates than the $z \sim 1$ relation. It should be noted that this relation has a large intrinsic scatter at all redshifts. In Fig.5 we show specific SFR versus rest-frame B-V which follows the expected trend.

Since we calculated the star formation rates using the integrated flux from three adjacent slits that cover a galaxy, aperture effects are negligible. On the other hand, we are forced to use different emission lines for calculating SFRs due to the differ-

ent rest-frame wavelength coverage of the spectra from galaxies at different redshifts. The conversions that are used for this purpose are likely to cause some systematic errors (Moustakas et al. 2006). To check for our sample, how successful it would be to use a constant factor for conversion from one emission line flux to the other, we plot the frequency distribution of emission line flux ratios in Fig. 6. This exercise shows that the uncertainty in H_α luminosities (Table 8) that is caused by these differences (sigma of the distribution) is about a factor 2.

3.4. Frequency Distribution of the Kinematic Irregularities

In Fig. 7 d, e and f, we show the frequency distribution of each (ir)regularity parameter for the field and cluster galaxies in our sample. The same information for local galaxies is given above each plot for comparison (Fig. 7 a, b and c). Cluster and field galaxies are distributed in a similar manner in the (ir)regularity parameters space. Both cluster and field galaxies populate regions inside and outside the area where regular velocity fields of local galaxies are located. The Kolmogorov-Smirnov (K-S) test of the distributions also confirms that field and cluster populations are not significantly different from one another (see Table 9). Here we discuss the origin of the largest parameter values: The two galaxies that have the largest σ_{PA} values are 1F6 and 4F7. 1F6 has a kinematically decoupled core, therefore, it is probably a merger remnant (Paper III, Fig.B.13). 4F7 seems to be a merger too. The residual of its velocity field and reconstructed velocity map reveals the existence of a counter-rotating component in the outer part (see Fig.B.49.g and j). There are tidal structures visible on its HST image as well (Fig.B.49.a). The largest $\Delta\phi$ belongs to 3F7 which has a strong bar (Fig.B.40). Although the kinematic and the photometric position angles match quite well in the disk region, the extent of the observed velocity field does not go far outside the bar (see Fig.B.40.a,c,e), therefore, this galaxy has a very large $\Delta\phi$ value. $\Delta\phi$ clearly has an important contribution of a bar in case of two other galaxies in our sample: 1F6 and 2C3. So a large $\Delta\phi$ either indicates a misalignment between the stellar disk and the kinematic axis of the gas, or the presence of a bar.

In Sect. 3.1, we determined the morphological type of the galaxies by our eye-ball classification (Table 3 & Table 4). Here we check how the (ir)regularity parameter values of different morphological types are distributed (Fig. 8) and find that irregularities in gas kinematics of spiral and irregular/peculiar galaxies are very similar (see Table 10 for the K-S test results).

3.5. Dependence On the Clustercentric Distance

All cluster members in our sample, except for 4C2, are well inside the virial radius, where both tidal processes and ICM-related mechanisms are effective. In Fig. 9, we show the distance of each galaxy from the cluster center in projection (in virial radii) and plot that against (ir)regularity parameters. There are quite a few galaxies within half a virial radius from the center, that are below the irregularity threshold of $k_{3,5}/k_1$ and σ_{PA}. $69 \pm 11\%$ of the cluster galaxies are regular according to both of these parameters while most of them have large $\Delta\phi$ values. The fraction of galaxies within $1\, R_{vir}$ that have regular gas kinematics according to all the three criteria is $13 \pm 8\%$.

Table 8. H_α luminosities.

Name (1)	$L_{H\alpha}/10^{40}[ergs/s]$ (2)	Line (3)
1C7	100	O[II]3727
1C8	20	Hβ
1C9	100	O[II]3727
1C10	100	Hβ
1F2	20	Hβ
1F3	20	Hβ
1F4	40	Hα
1F5	100	Hα
1F6	10	Hα
1F7	600	O[II]3727
1F10	20	O[III]5007
2C3	10	Hβ
2C5	10	Hβ
2C6	30	O[II]3727
2C7	20	O[III]5007
2C8	9	Hα
2F1	30	Hβ
2F2	1	O[II]3727
2F3	100	O[II]3727
2F4	10	O[II]3727
2F5	7	O[II]3727
2F6	30	Hα
2F9	9	O[III]5007
2F10	100	O[III]5007
2F11	9	Hα
2F12	30	O[II]3727
2F15&16	–	O[II]3727
3C3	50	Hα
3C4	30	O[III]5007
3C5	20	O[III]5007
3C6	9	O[II]3727
3C7	15	O[III]5007
3F3	2	O[III]5007
3F6	30	Hα
3F7	30	Hα
3F8	40	O[II]3727
3F9	30	Hα
4C2	20	O[II]3727
4C3	8	O[II]3727
4F3	300	O[II]3727
4F4	100	O[III]5007
4F5	100	O[II]3727
4F6	50	O[II]3727
4F7	200	O[II]3727
4F8	60	O[III]5007
4F9	80	O[III]5007
4F12	200	O[II]3727
4F13	100	O[III]5007
NGC0628	50	
NGC2976	3	
NGC3031	14	
NGC3049	–	
NGC3184	15	
NGC3521	20	
NGC3621	60	
NGC3938	15	
NGC4236	4	
NGC4536	50	
NGC4569	20	
NGC4579	30	
NGC4625	–	
NGC4725	–	
NGC5055	30	
NGC5194	70	
NGC5713	–	
NGC7331	50	

Column (1): galaxy ID; Col. (2): H_α luminosity; Col. (3): emission line that is used for calculating the H_α luminosity.
The errors in H_α luminosities are estimated to be $\sim 50\%$ based on the width of the histograms in Fig. 6.
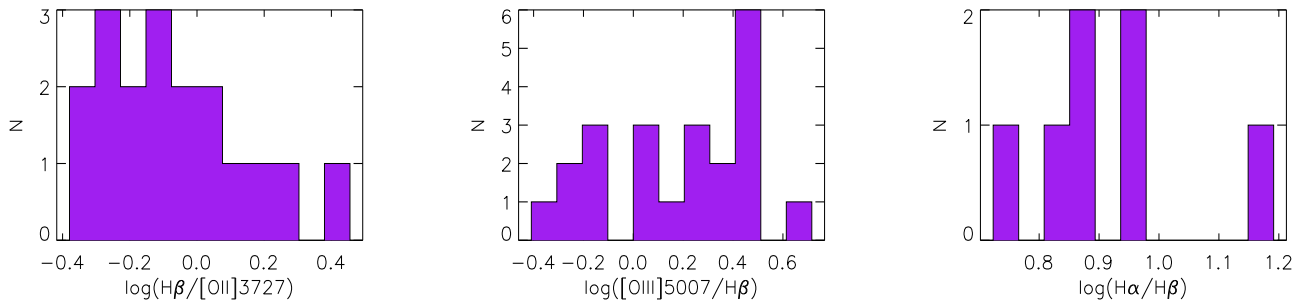
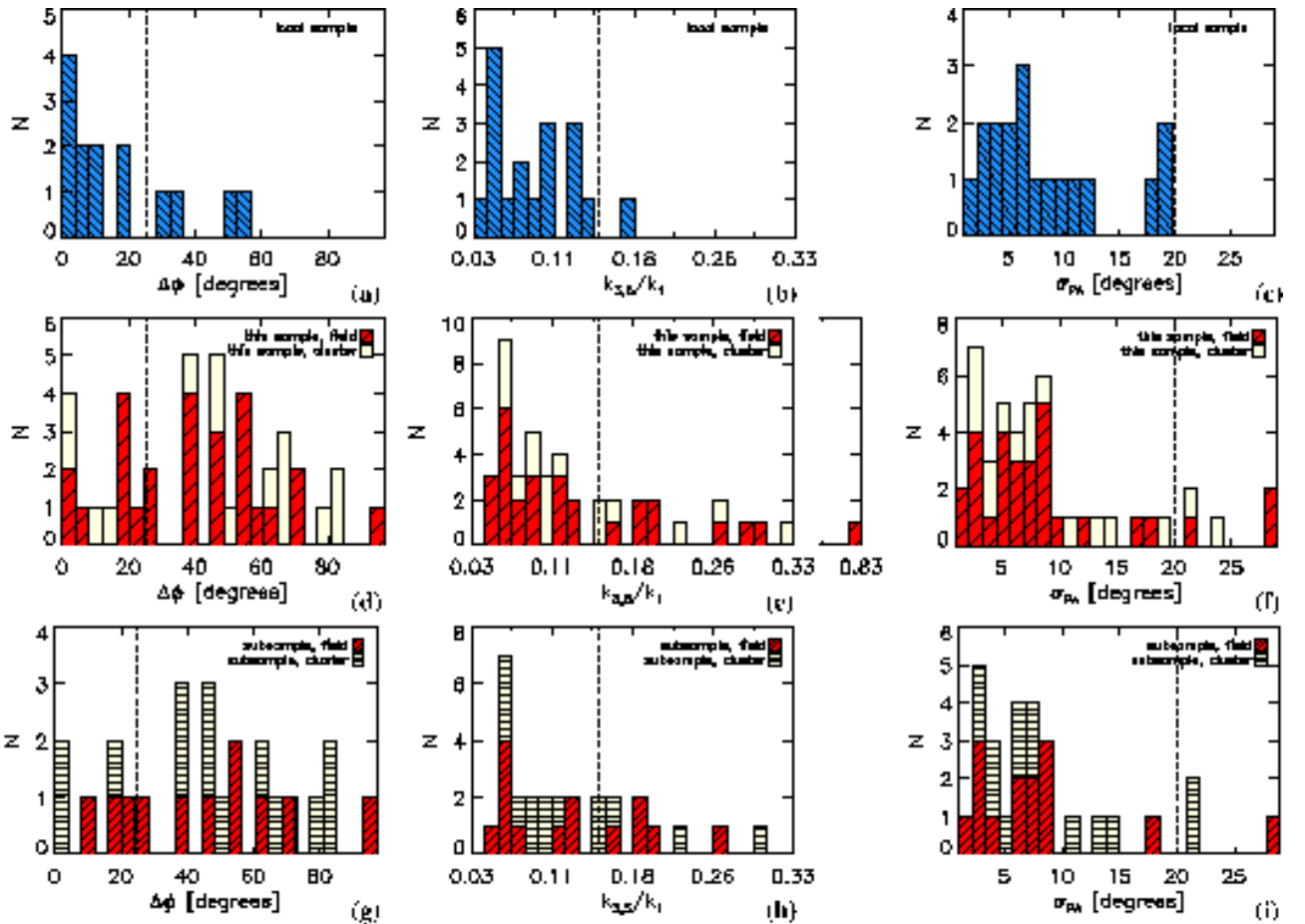**Fig. 6.** Histograms of the emission line flux ratios

Fig. 7. Histograms of the mean misalignment between kinematic and photometric major axes ($\Delta\phi$), mean $k_{3,5}/k_1$ and standard deviation of kinematic position angle (σ_{PA}). The local sample is given in panel. (a), (b) and (c). Our sample is given in panel (d), (e) and (f). In panel (g), (h) and (i) we show the galaxies in our sample that have H_α luminosities in the same interval as the local sample. The regularity borders, that are indicated on each plot, were determined in Paper III using the local sample except for the peculiar galaxies and Virgo members. $\Delta\phi$ of the galaxies that have $\epsilon \leq 0.1$ (galaxies 1F2, 2F4, 2F12 and 4C3 in "this sample", NGC 628, NGC 3184, NGC 3938 and NGC 5713 in the local sample), $k_{3,5}$ of galaxy 1F5 (this sample) and all parameters for galaxies 1F10, 2F5, 2F11 and 2F15&16 (this sample) are doubtful as explained in Paper III for the MS 0451 sample and here, in Sect. 3.8 for the rest, therefore, they are excluded from the histograms.

3.6. Correlations

Here we measure the correlations of the irregularity parameters with the H_α luminosity, with each other and with some photometric parameters using an outlier resistant linear regression fitting technique (Table 11).

3.6.1. Correlations With H_α Luminosity

H_α luminosities are listed in Table 8. In case the H_α line was outside the observed wavelength interval, we converted the fluxes of available emission lines to H_α flux as explained in Sect. 3.3.

For the cluster members, we find significant correlations between the $log(L_{H_\alpha})$ and two indicators of kinematical irregularities: σ_{PA} and $k_{3,5}/k_1$ (Fig.10, a and b). Hα emission mainly stems from HII regions and it indicates star formation (e.g. Kennicutt et al. 1994). B-V color and Hα luminosity are ex-
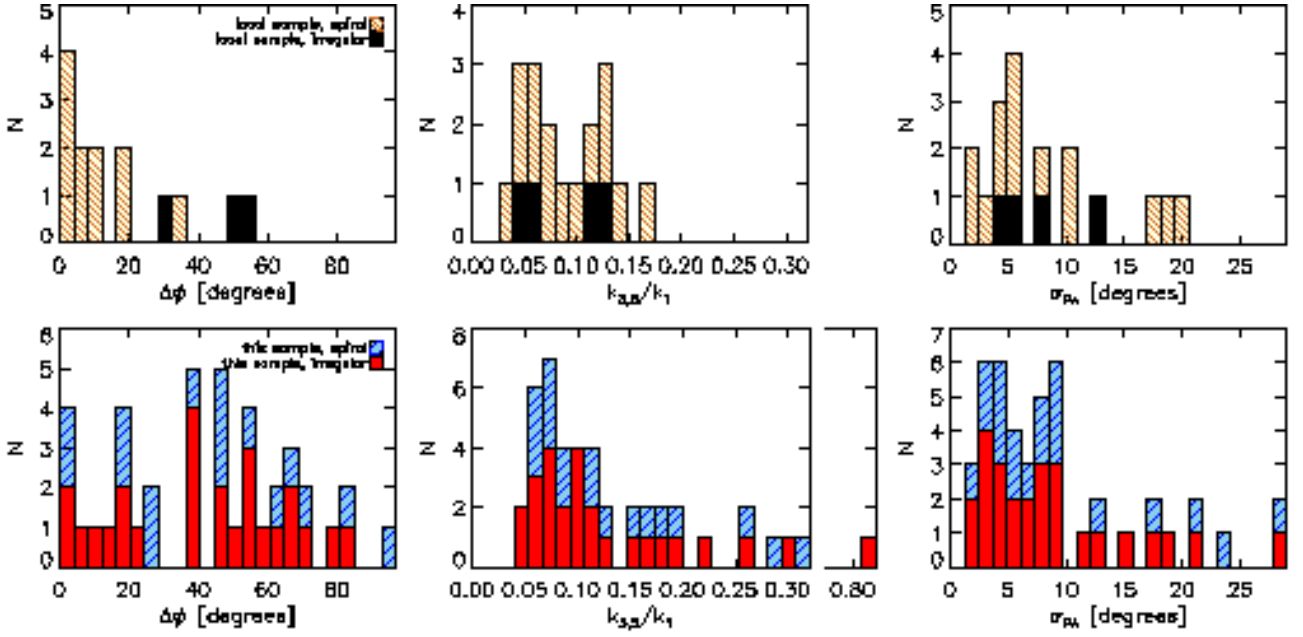
Fig. 8. Histograms of the mean misalignment between the kinematic and photometric major axes ($\Delta\phi$), the mean $k_{3,5}/k_1$ and the standard deviation of the kinematic position angle (σ_{PA}) for spiral versus irregular/peculiar galaxies in the local sample (top) and in our sample (bottom). The morphological types are determined by our eye-ball classification (see Table 3 and Table 4) $\Delta\phi$ of the galaxies that have $\epsilon \leq 0.1$ (galaxies 1F2, 2F4, 2F12 and 4C3 in "this sample", NGC 628, NGC 3184, NGC 3938 and NGC 5713 in the local sample), $k_{3,5}$ of galaxy 1F5 (this sample) and all parameters for galaxies 1F10, 2F5, 2F11 and 2F15&16 (this sample) are doubtful as explained in Paper III for the MS 0451 sample and here, in Sect. 3.8 for the rest; therefore, they are excluded from the histograms.

Table 9. K-S statistics of (ir)regularity parameters of the cluster and field galaxies in our sample.

	D	P
σ_{PA}	0.18	0.874
$k_{3,5}/k_1$	0.18	0.856
$\Delta\phi$	0.32	0.209

D: K-S statistics specifying the maximum deviation between the cumulative distribution of the given parameter for cluster and field galaxies in our sample; P: significance level of the K-S statistics.
Note: $k_{3,5}/k_1$ of galaxy 1F5, $\Delta\phi$ of the galaxies that have $\epsilon \leq 0.1$ (galaxies 1F2, 2F4, 2F12 and 4C3) and all parameters for galaxies 1F10, 2F5, 2F11 and 2F15&16 are excluded from the calculations as explained in Paper III for the MS 0451 sample and here, in Sect. 3.8 for the rest.

Table 10. K-S statistics comparing the kinematic (ir)regularity parameters of the galaxies in our sample classified as spiral or irregular/ peculiar using their photometry.

	D	P
σ_{PA}	0.15	0.995
$k_{3,5}/k_1$	0.10	1.000
$\Delta\phi$	0.25	0.786

D: K-S statistics specifying the maximum deviation between the cumulative distribution of the given parameter for spiral and irregular galaxies in our sample; P: significance level of the K-S statistics.
Note: $k_{3,5}/k_1$ of galaxy 1F5, $\Delta\phi$ of the galaxies that have $\epsilon \leq 0.1$ (1F2, 2F4, 2F12 and 4C3) and all parameters for 1F10, 2F5, 2F11 and 2F15&16 have been excluded from the calculations as explained in Paper III for the MS 0451 sample and here, in Sect. 3.8 for the rest.

pected to anti-correlate with each other for a given morphological type since galaxies with bluer B-V colors have a larger ratio of blue to red stars, and therefore, a better capability of ionizing the gas to form HII regions (Cohen 1976). However, dust extinction can weaken this correlation. For our data, we find a weak anti-correlation between these two quantities only for cluster members (Fig.10, c). The irregularity parameters become larger for bluer galaxies. However the trends are very weak (see Table 11).

3.6.2. Correlations Between (Ir)regularity Parameters

To be able to use the (ir)regularity parameters as a tool to distinguish disturbed velocity fields from regular ones, it is necessary to determine a threshold value for each of them. We did that by measuring each parameter for local, regular velocity fields from SINGS (see Paper III, Sect. 4). In Fig. A.1 in the

Appendix, we show how the galaxies in our sample and in the local sample are distributed in the plane of one parameter versus another. Regularity borders that are defined using the local galaxies are indicated on each plot. We find a weak correlation between $k_{3,5}/k_1$ and σ_{PA} (see Table 11) which agrees with what we found in Paper III using only the MS 0451 sample. If we look at the galaxies that have large $k_{3,5}/k_1$ and σ_{PA} parameters, most of them show signs of an additional kinematic component in the residual of the simple rotating model and the original velocity field (residual maps are presented in Sect. B, part (j) of each figure). These galaxies are 1F4, 1F6, 4F7 and 4F8. In all cases, the existence of a secondary component is clear in the residual map. k_5 is sensitive to extra kinematic components and σ_{PA} is sensitive to their misalignment with the main component. Therefore, the outliers of the $k_{3,5}/k_1$ versus σ_{PA} plot mostly consist of velocity fields that have multiple kinematic components. This explains the weak correlation between these two parameters.
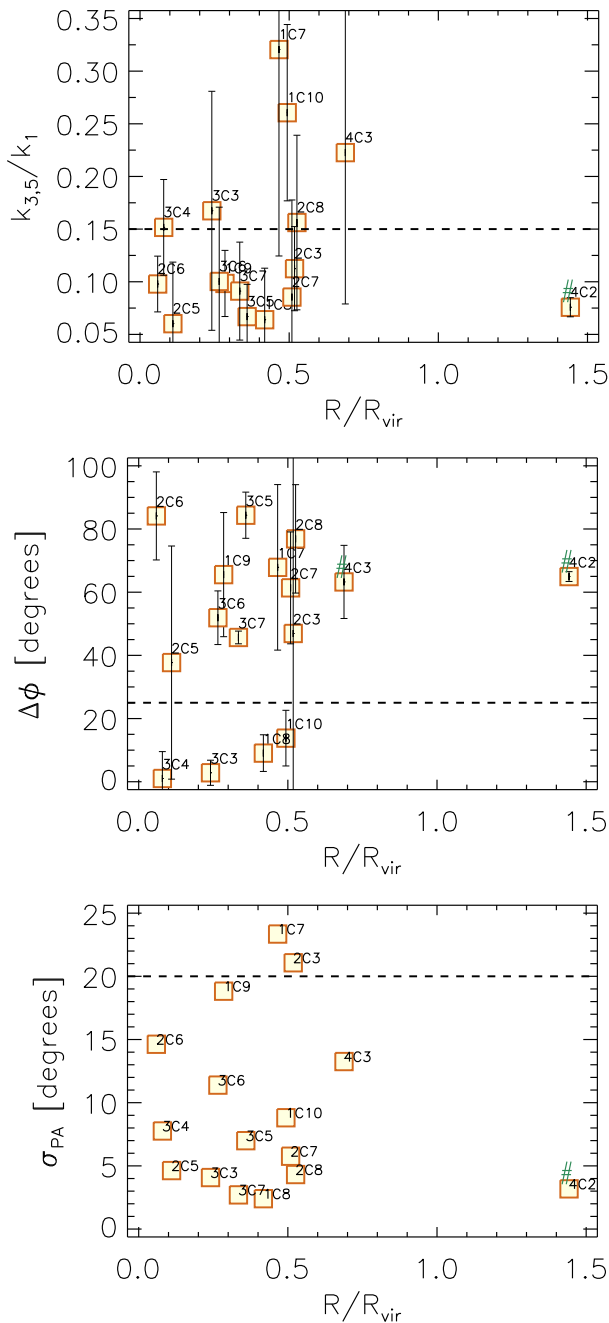
Fig. 9. (Ir)regularity parameters versus R/R_{vir}. The regularity threshold of each parameter is shown with a dashed line. # symbol indicates the galaxies that are not used in correlation measurements. 4C2 is excluded because the correlations are measured inside 1 R_{vir}. 4C3 is excluded from the correlation measurement of $\Delta\phi$ since it has $\epsilon \leq 0.1$ (see Sect. 3.8). *Top*: mean $k_{3,5}/k_1$ versus R/R_{vir}. *Middle*: mean misalignment between kinematic and photometric axes ($\Delta\phi$) versus R/R_{vir}. *Bottom*: standard deviation of kinematic position angle (σ_{PA}) versus R/R_{vir}.

3.6.3. Correlations With Photometric Parameters

Apart from the Gini coefficient, M_{20}, photometric asymmetry and concentration parameters that are defined in Sect. 3.1, the methods we use for measuring the morphological/photometric parameters are explained in Paper III. Photometric and morphological parameters of the galaxies in our sample are given in

Table 11. Linear Pearson correlation coefficients.

	$\sigma_{PA} - k_{3,5}/k_1$	$\Delta\phi - \sigma_{PA}$	$k_{3,5}/k_1 - \Delta\phi$
c+f	**0.5 (Fig. A.1,a)**	0.0	0.0
	$\sigma_{PA} - R/R_{vir}$	$\Delta\phi - R/R_{vir}$	$k_{3,5}/k_1 - R/R_{vir}$
c	0.1	0.2	0.4
	$R_d - k_{3,5}/k_1$	$R_d - \sigma_{PA}$	$R_d - \Delta\phi$
c+f	0.2	0.3	−0.4
c	0.1	**0.5 (Fig. 11,b)**	−0.1
	$M_B - k_{3,5}/k_1$	$M_B - \sigma_{PA}$	$M_B - \Delta\phi$
c+f	0.0	−0.1	0.4
c	−0.3	**−0.5 (Fig. 11,c)**	0.1
	$A - k_{3,5}/k_1$	$A - \sigma_{PA}$	$A - \Delta\phi$
c+f	−0.2	0.1	−0.1
c	−0.1	0.2	0.0
	$C - k_{3,5}/k_1$	$C - \sigma_{PA}$	$C - \Delta\phi$
c+f	0.0	−0.1	0.2
c	0.1	0.0	−0.2
	$log(L_{H_\alpha}) - k_{3,5}/k_1$	$log(L_{H_\alpha}) - \sigma_{PA}$	$log(L_{H_\alpha}) - \Delta\phi$
c+f	0.1	0.1	−0.1
c	**0.8 (Fig. 10,b)**	**0.8 (Fig. 10,a)**	0.0
	$z - k_{3,5}/k_1$	$z - \sigma_{PA}$	$z - \Delta\phi$
f	0.1	0.0	0.1
	$(B-V) - k_{3,5}/k_1$	$(B-V) - \sigma_{PA}$	$(B-V) - \Delta\phi$
c+f	−0.1	−0.2	−0.2
c	−0.2	−0.1	−0.2
	$(V-I) - k_{3,5}/k_1$	$(V-I) - \sigma_{PA}$	$(V-I) - \Delta\phi$
c+f	0.0	0.2	0.0
c	0.4	0.2	0.1
	$(R-I) - k_{3,5}/k_1$	$(R-I) - \sigma_{PA}$	$(R-I) - \Delta\phi$
c+f	−0.1	−0.2	0.0
c	−0.3	−0.3	−0.2
	$Gini - k_{3,5}/k_1$	$Gini - \sigma_{PA}$	$Gini - \Delta\phi$
c+f	−0.1	0.0	0.3
c	0.2	0.1	0.1
	$M_{20} - k_{3,5}/k_1$	$M_{20} - \sigma_{PA}$	$M_{20} - \Delta\phi$
c+f	0.1	0.2	0.0
c	0.1	0.3	**0.5 (Fig. 11,a)**
	$log(M_*[M_\odot]) - k_{3,5}/k_1$	$log(M_*[M_\odot]) - \sigma_{PA}$	$log(M_*[M_\odot]) - \Delta\phi$
c+f	−0.3	−0.2	−0.4
c	−0.2	0.0	−0.3

The figures where $\Delta\phi$ of the galaxies that have $\epsilon \leq 0.1$ (galaxies 1F2, 2F4, 2F12 and 4C3 in "this sample", NGC 628, NGC 3184, NGC 3938 and NGC 5713 in the local sample), $k_{3,5}/k_1$ of galaxy 1F5 (this sample) and all parameters for galaxies 1F10, 2F5, 2F11 and 2F15&16 (this sample) are doubtful as explained in Paper III for the MS 0451 sample and here, in Sect. 3.8 for the rest. Therefore, they are excluded while calculating the correlation coefficients. For the calculation of the correlations with the redshift, only field galaxies were used, so the results do not have the bias of the environment.

Table C.1 and Table C.2 respectively (see Paper III, Table C.2 for the morphological parameters of the MS 0451 sample.). The (ir)regularity parameters of the local sample galaxies are given in Paper III, Table 3. Their photometric parameters are given here, in Table 5.

To focus on the effects of the interactions that take place only in clusters, we now restrict ourselves to our cluster sample, where most galaxies are within half a virial radius from the cluster center. In this region, mergers are rare, while harassment and ICM related mechanisms such as ram pressure stripping are expected to be effective (Moore et al. 1997). We give the correlation measurements of the cluster members that are located within $1R_{vir}$ from the cluster center in Table 11. The parameters that correlate with each other are plotted in Fig. 11 and discussed in Sect. 4.5.

3.7. The Fraction of Irregular Gas Kinematics

We quantified irregularities in gas kinematics using three different parameters, and for each of them, we compared the num-
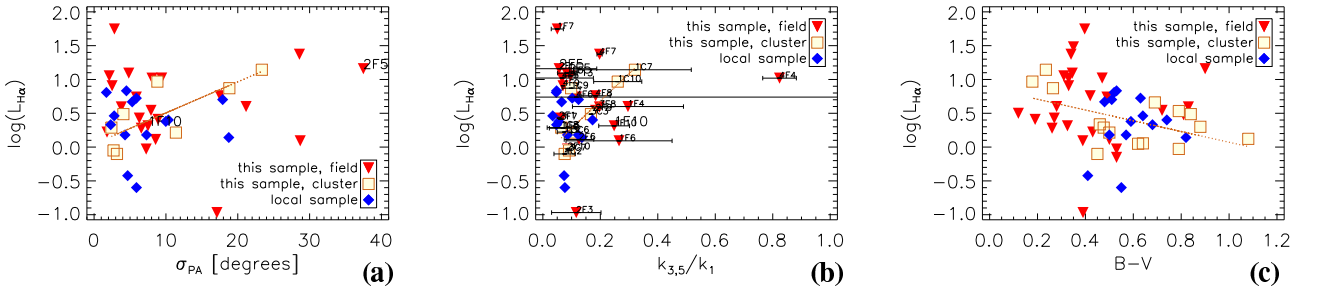
Fig. 10. a) Hα luminosity versus standard deviation of kinematic position angle (σ_{PA}). Correlation coefficient for cluster members is 0.8. **b)** Hα luminosity versus mean $k_{3,5}/k_1$. Correlation coefficient for cluster members is 0.8. **c)** Hα luminosity versus B-V color for our sample and the local sample. Correlation coefficient for cluster members is -0.5. Correlations are shown on top of each plot.

Table 12. Irregularity fraction.

	frac$_{\sigma_{PA}}$	frac$_{\Delta\phi}$	frac$_{k_{3,5}/k_1}$	frac$_{any}$	frac$_{all}$
	(1)	(2)	(3)	(4)	(5)
field & cluster	11 ± 5 %	68 ± 7 %	32 ± 7 %	80 ± 6 %	4 ± 3 %
only field	10 ± 6 %	65 ± 9 %	32 ± 9 %	76 ± 8 %	3 ± 3 %
only cluster	13 ± 8 %	73 ± 11 %	31 ± 12 %	88 ± 8 %	6 ± 6 %

Column (1): fraction of irregular velocity fields according to σ_{PA} criterion; Col. (2): fraction of irregular velocity fields according to $\Delta\phi$ criterion; Col. (3): fraction of irregular velocity fields according to $k_{3,5}/k_1$ criterion; Col. (4): fraction of irregular velocity fields according to at least one of the three criteria; Col. (5): fraction of irregular velocity fields according to all the three criteria together.
Poisson errors are given for each fraction.
Note: $k_{3,5}/k_1$ of galaxy 1F5, $\Delta\phi$ of the galaxies that have $\epsilon \leq 0.1$ (1F2, 2F4, 2F12 and 4C3) and all parameters for 1F10, 2F5, 2F11 and 2F15&16 have been excluded from the calculations as explained in Paper III for the MS 0451 sample and here, in Sect. 3.8 for the rest.

ber distribution of field and cluster galaxies. Now we will look at the fraction of galaxies that have irregular gas kinematics. Fractions that are measured for each irregularity type separately and also without distinguishing between the three types are given in Table 12. We obtain very similar fractions of irregular gas kinematics for cluster and field environments. Each irregularity parameter gives a very different fraction compared to the others, which will be discussed in Sect. 4.3.

3.8. Special Cases

Here we explain the cases that we exclude from our analysis. For the same information on the MS 0451 sample, see Paper III, Sect. 4.1. For face-on galaxies, photometric position angle measurements are very uncertain. Since LOS velocities are very small in such cases, the effect of noise becomes more pronounced in velocity fields. This causes $\Delta\phi$ to be unreliable. Therefore, we excluded such cases from our analysis (2F4, 2F11, 2F12, 4C3). Among those, 2F11 is an extreme case which is completely excluded from the analysis (see Fig.B.29.e). The other galaxies that we did not use in our analysis are 2F5, 2F15&16. 2F5 does not have any signal in the upper slit, which affects the measurements. Looking at the iso-velocity lines on the receding side (Fig.B.23.e), it looks as if the highest positive velocities are located in the top right corner, which is missing on the map. 2F15&16 (see Fig.B.33) are at the same redshift, however it is not clear what kind of objects they are and the emission line they have could not be identified. The velocity field includes information from both, but most of it comes from 2F15. The [OIII]5007 velocity field of 4F4 (see Fig.B.46.e)

looks quite disturbed, although the flux map of the same emission line looks rather regular. Emission from this galaxy is very strong and therefore, we can rely on its (ir)regularity parameters.

4. Discussion

4.1. Frequency Distribution of the Kinematic Irregularities

We analyze together gas kinematics and stellar photometry of spiral galaxies in clusters and in the field. We find that the fraction of galaxies that have irregular gas kinematics is very similar in our cluster and field samples. These two samples also give a very similar frequency distribution of each (ir)regularity parameter. When interpreting the results we have to consider that our sample selection is based on the emission line flux of galaxies. A comparison of our sample with a local sample from SINGS shows that some galaxies in both our cluster and field samples have higher H_α luminosities, and therefore, higher star formation rates (Fig.1). In some of these cases, high star formation activity might be the result of some type of interaction. It has to be considered, however, that H_α luminosity of a galaxy can also increase due to facts that are unrelated to interactions such as regular starbursts (Kennicutt 1998).

In Fig. 7 (g), (h) and (i) we show how the subsample of galaxies that have H_α luminosities within the same interval as the SINGS sample is distributed in the (ir)regularity parameters space. The field galaxies that are populating the high irregularity end of the plots are not necessarily the ones with high H_α luminosities. So, independent from whether the high star formation galaxies are included or not, the distribution of cluster and field galaxies in irregularity space is very similar. The majority of the field galaxies in our sample are more irregular than local field galaxies according to at least one of the three (ir)regularity criteria. This is the case even if we take into account only the ones that have H_α luminosities within the same interval as the SINGS sample, which are mostly in the interval $0.1 \leq z \leq 0.5$. This could be the result of a higher occurence of disk building processes such as mergers and accretion events at these redshifts. Using N-body simulations, Gottlöber et al. (2001) investigate the relative major merger rate of the population of cluster, group and isolated halos as a function of redshift. They find that for cluster galaxies, the relative merger rate increases with redshift while it decreases for isolated galaxies. At $z \sim 0.5$, they find the major merger rate in the field to be two times as high as that in clusters (see Gottlöber et al. 2001, Fig. 9).

In the local universe, evidence has been accumulating, mainly from HI studies, on the importance of cold gas accretion: A large number of galaxies are accompanied by gas-rich dwarfs or are surrounded by HI cloud complexes, tails and filaments

Table 13. Possible dynamical pairs.

Pair	Projected distance [kpc]	ΔV [km/s]
2F10 & 2F11	262	420
4F10 & 4F12	737	90
4F5 & 4F6	842	60
4F6 & 4F7	775	360
4F5 &4 F7	1170	230

Column (1): Names of the galaxies; Col. (2): the projected distance between them; Col. (3): the difference between their radial velocities.

(Sancisi et al. 2008). Most of the high-velocity clouds around the Milky Way are now widely accepted to belong to its halo and direct evidence for infall of intergalactic gas (Wakker et al. 2007, 2008). Recently, accretion of satellites has also been revealed by studies of the distribution and kinematics of stars in the halos of the Milky Way and of M31. The discovery of the Sgr Dwarf galaxy (Ibata et al. 1994) is regarded as proof that accretion is still taking place. It is also possible that the warped outer layers, lopsidedness and the extra-planar gas, which are very common features in galaxies, are related to the accretion process. Observational results suggest cold gas accretion to be a likely formation mechanism for the polar disks (Bravo-Alfaro et al. 2004; Stanonik et al. 2009). Simulations support this picture (Macciò et al. 2006).

The radial velocity difference and angular separation of some galaxies in our sample suggest that they may be gravitationally bound to each other. Since we do not have the spectra of the objects surrounding the galaxies in our sample, we can not make a definite statement of whether they are group members or not. The number statistics in Huchra & Geller (1982) show that velocity dispersions up to 400 kms^{-1} and sizes up to 2 Mpc are likely (with median values of 155 kms^{-1} and 0.7 Mpc) for galaxy groups. For galaxy pairs, it is expected that at least 35 percent of the ones with projected separation of less than 20 h^{-1} kpc and velocity difference of less than 500 kms^{-1} are physically bound (De Propris et al. 2007). On the other hand there are several interacting pairs with a projected separation of around 50 h^{-1} kpc (Barton et al. 1999; Patton et al. 2000). Lambas et al. (2003) find that star formation in galaxy pairs is significantly enhanced over that of isolated galaxies with similar redshifts in the field for projected separations less than 25 h^{-1} kpc and velocity differences of less than 100 kms^{-1}.

Based on this information, the galaxies in our sample that might be gravitationally interacting with each other are listed in Table 13. The average values of each irregularity parameter for these galaxies (excluding the unreliable values that are mentioned in Paper III for the MS 0451 sample and here, in Sect. 3.8 for the rest) are $k_{3,5}/k_1 = 0.15$, $\sigma_{PA} = 13$ and $\Delta\phi = 23$. Among these galaxies, 4F7 has a very large σ_{PA} and 4F12 has a very high $k_{3,5}/k_1$. Excluding the galaxies in Table 13 from the comparison between the irregularity distributions of the cluster and field galaxies (see Sect. 3.4) does not change the results (see Table 14).

4.2. Frequency Distribution of the Morphological Parameters

In Sect. 3.1 we compare the distributions of some morphological parameters: asymmetry, concentration, M_{20} and Gini coefficient for distant cluster versus field samples as well as for local versus distant field samples (see Fig.2 and Table 6). We find a significant difference between the distribution of the concentration, the Gini coefficient and the M_{20} parameter for the cluster

Table 14. K-S statistics of (ir)regularity parameters of the cluster and field galaxies in our sample, excluding possible dynamical pairs.

	D	P
σ_{PA}	0.21	0.740
$k_{3,5}/k_1$	0.20	0.791
$\Delta\phi$	0.30	0.317

D: K-S statistics specifying the maximum deviation between the cumulative distribution of the given parameter for cluster and field galaxies in our sample excluding the galaxies in Table 13; P: significance level of the K-S statistics.
Note: $k_{3,5}/k_1$ of galaxy 1F5, $\Delta\phi$ of the galaxies that have $\epsilon \leq 0.1$ (galaxies 1F2, 2F4, 2F12 and 4C3) and all parameters for galaxies 1F10, 2F5, 2F11 and 2F15&16 are excluded from the calculations as explained in Paper III for the MS 0451 sample and here, in Sect. 3.8 for the rest.

versus field galaxies at intermediate redshifts, in the sense that the cluster sample lacks galaxies with low concentration index. This might be due to the activity of interaction processes such as harassment which causes matter to migrate towards the center.

The local and distant field samples are also different: the concentration, the Gini coefficient and the M_{20} index all suggest that local galaxies have a more centrally-concentrated and less clumpy light distribution with respect to the distant galaxies. This is consistent with what we find studying gas kinematics: it looks as if field galaxies at intermediate redshifts are still in the process of building up their disks.

4.3. The Fraction of Irregular Gas Kinematics

In Y08, the [OII] doublet velocity fields of 63 field galaxies, that are at $z = 0.4 - 0.75$ and that have $M_{stellar} \geq 1.5 \times 10^{10} M_\odot$, are analyzed. They classify galaxy kinematics based on an eye-inspection of the gas velocity map, gas velocity dispersion map and high resolution image together. Their study of velocity fields however is limited to $2'' \times 3''$ field of view while it can be as large as $\sim 3'' \times 6''$ in our case. They call a galaxy "rotating disk" if its velocity field has an ordered gradient, the photometric and the kinematic major axes are aligned and the velocity dispersion map has a single peak close to the kinematic center. If the velocity dispersion map has no peak or has a peak that is offset from the center while the other criteria are satisfied, they classify the case as "perturbed rotation". If both the velocity dispersion map and the velocity map deviate from the regular case, they classify it as "complex kinematics". Deviation from the regular case for a velocity field corresponds here to an irregular velocity gradient and/or a misalignment between the photometric and kinematic axes. Therefore, when the three indications we use are at the level of being detectable by eye within the central part of a galaxy, its kinematics can be classified as complex according to this scheme. Even then they find that 26% of their sample have velocity fields and velocity dispersion maps that are both incompatible with disk rotation. When we calculate the irregularity fractions of the field galaxies in our sample that are within the same redshift interval as their sample, we find $10 \pm 9\%$ (according to σ_{PA}), $60 \pm 15\%$ ($\Delta\phi$), $30 \pm 14\%$ ($k_{3,5}/k_1$). Their result is very close to what we find using the $k_{3,5}/k_1$ criterion. However it should be noted that most of the galaxies in our sample are less massive (see Table C.1, Column 8).

It is known from the local Universe that most galaxies in the central parts of galaxy clusters lack gas. To be able to study velocity fields of galaxies, priority was given to emission line
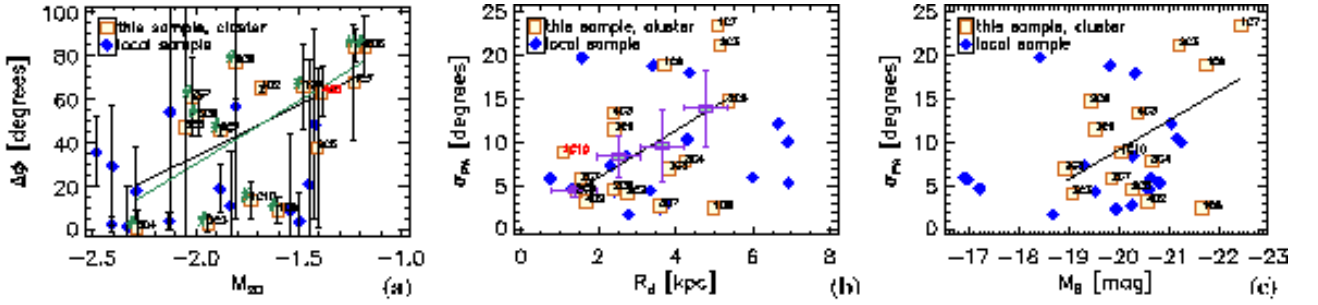
Fig. 11. (Ir)regularity parameters versus some photometric quantities. For each plot, the line shows the correlation between the given parameters. The local galaxies are not used in correlation measurements, but shown as a reference in each plot. The names that are written in red and italic belong to the galaxies that are excluded from the correlation as explained in Paper III for the MS 0451 sample and here, in Sect. 3.8 for the rest. *a*: M_{20} index versus the mean misalignment between the photometric and kinematic major axes ($\Delta\phi$) (correlation coefficient=0.5). The thick green line shows the correlation obtained excluding the cases where the $\Delta\phi$ value mainly indicates a clumpy light distribution or a bar instead of an abnormality in the position of the kinematic axis. The galaxies for which this is the case are indicated with # symbol next to them. Measuring the correlation after excluding these galaxies gives the same result. *b*: The disk scale length (R_d) versus the standard deviation of the kinematic position angle (σ_{PA}) (correlation coefficient=0.5). The standard deviation of σ_{PA} is measured within equal R_d intervals that are indicated with horizontal error bars and the mean σ_{PA} in each bin is given with a rectangular green symbol while the deviation from the mean is given with vertical error bars. *c*: Absolute magnitude in the *B* band (M_B) versus the standard deviation of the kinematic position angle (σ_{PA}) (correlation coefficient= -0.5).

galaxies in our sample selection. Therefore, most cluster galaxies in our sample are perhaps just infalling and have not been severely affected by the cluster environment yet. This would explain the similarity between the gas kinematics of cluster and field galaxies in our sample.

We use $k_{3,5}/k_1$, σ_{PA} and $\Delta\phi$ to trace the effects of the interaction processes on gas kinematics. We find that the irregularity fractions measured using each of these parameters are very different from one another: σ_{PA} gives a value around 10%, $k_{3,5}/k_1$ $\sim$ 30% and $\Delta\phi \sim$ 70% for both cluster and field galaxies. This may have a number of different reasons. One is the effect of lower spatial resolution for intermediate redshift galaxies. Our simulations in Paper III, Appendix A, indicate that small scale irregularities may be smeared out as a result of the resolution effects. A misalignment between the stellar disk and the rotation plane of the gas on the other hand is unlikely to be affected much by low resolution. One should also realize that not all galaxies with high $\Delta\phi$ are irregular. For example, galaxies with bars can have larger $\Delta\phi$ values. Also, some galaxies in the local universe are found showing regular kinematics with an HI polar disk (perpendicular to the stellar disk) (van Gorkom & Schiminovich 1997; Stanonik et al. 2009). Petrosian et al. (2002) observed 18 blue compact dwarf galaxies and for 8 of these they found strong misalignments between the photometric and kinematic position angles although the isovelocity contours do not indicate strong irregularities in gas motions. There are even merger remnants in the local universe that have very regular gas velocity fields such as NGC 3921 (Hibbard & van Gorkom 1996).

4.4. Correlations With the H_α Luminosity

Larger irregularities ($k_{3,5}/k_1$ and σ_{PA}) we find for higher $log(L_{H_\alpha})$ probably show that galaxies which have more irregular gas kinematics have higher star formation rates. These correlations are valid only for cluster members (see Fig.10). According to models, most interaction processes in clusters increase star formation activity at the beginning, before they eventually suppress it. Gravitational interactions are expected first to trigger nuclear gas infall. Models by Fujita (1998) show that in-

creased star formation activity is expected in case of harassment, since high-speed encounters between galaxies cause gas to accumulate to centers of galaxies. Ram-pressure stripping, which is the hydrodynamic interaction between the hot ICM and the cold ISM, leads to an increase of the external pressure, shock formation, thermal instabilities and turbulent motions within the disk. Evrard (1991) and Bekki & Couch (2003), for example, show that all these events increase cloud-cloud collisions and cloud collapse, and therefore, enhance star formation activity. However, in case of ram-pressure stripping, there are not many observations supporting this picture. Some examples in A1367 that experience ram-pressure stripping are CGCG 97-023, where enhanced star formation activity per unit mass, compared to galaxies of similar type and luminosity is confirmed (Gavazzi et al. 1995), CGCG 97-073 and CGCG 97-079 (Boselli & Gavazzi 2006). Models of Fujita (1998) and Fujita & Nagashima (1999) that quantify the variations of the star formation activity, show that on short timescales ($\sim 10^8$ yr) in high-density, rich clusters, the star formation activity can increase by up to a factor of 2 at most. But on longer timescales, removal of the HI gas leads to a decrease of the fuel feeding the star formation, and galaxies become quiescent (Fujita 1998; Fujita & Nagashima 1999; Okamoto & Nagashima 2001).

4.5. Correlations With Photometric Parameters

We find a weak correlation between M_{20} and $\Delta\phi$ for cluster members (Fig. 11a). M_{20} becomes very large in case the galaxy light has a clumpy distribution. Since clumpiness is mainly caused by star forming regions, it means that galaxies that have irregular gas kinematics have more star formation. M_{20} also increases towards later types. Since galaxies that have high mass concentration (earlier types) are more resistant to tidal mechanisms, the correlation we find is expected as a result of this fact as well. The concentration parameter on the other hand, which is another indicator of galaxy type, does not give any correlation with the irregularity in gas kinematics. Therefore, the substructures must be the main cause of the correlation that we find.

We need to note that $\Delta\phi$ cannot be considered as a pure indicator of interactions since it is sensitive to bars that are misaligned with the disk. Even though the formation of a bar can be triggered by environmentally induced gravitational instabilities, such as tidal interactions between galaxies and the cluster potential well, it can also just be the result of a misalignment between the disk and the triaxial halo of the galaxy itself (Kodama & Smail 2001; Bekki & Freeman 2002). Since a bar is not necessarily formed by an interaction process, we remeasured the correlation of $\Delta\phi$ with the other parameters excluding the cases where we see that a bar has an important contribution to the $\Delta\phi$ value (3F7, 1F6 and 2C3). The results remained the same.

We find a correlation between the disk scale length and σ_{PA} (Fig. 11b). However, what we see on the plot is an increasing deviation of σ_{PA} values with increasing R_d rather than a correlation. While small galaxies are all regular, there are both regular and irregular cases among larger galaxies. It is known that some interaction processes are more effective on larger galaxies such as interactions between galaxies and the cluster potential well, viscous stripping and thermal evaporation. Tidal interactions between galaxies, on the other hand, are more efficient on smaller galaxies (Byrd & Valtonen 1990). What we see in our data might be an indication of the activity of some of the first group processes in the central $1R_{vir}$ of the clusters in our sample.

We find that M_B and σ_{PA} anti-correlate with each other (Fig. 11c) showing that more massive galaxies have more irregular gas kinematics. Since larger galaxies are also more massive (Trujillo et al. 2004), the interpretation of this correlation is the same as the correlation that we find for the disk scale length. One or a combination of the following mechanisms might be effective on the cluster members in our sample: viscous stripping, thermal evaporation and tidal interactions between galaxies and the cluster potential well.

We investigated whether morphological peculiarities correlate with irregularities in the gas kinematics. Among the galaxies that have irregular/peculiar morphology according to our eyeball classification (see Table 3 and Table 4), there is no trend towards larger kinematical irregularities (see Fig. 8). We find very similar distributions of the irregularity parameters for spirals and irregular/peculiar galaxies (Table 10). We also do not find a correlation between the photometric asymmetry and irregularities in the gas kinematics. Neichel et al. (2008) on the other hand find a good agreement between their morphological and kinematical classifications.

For the correlations that we find for cluster galaxies, where the σ_{PA} parameter is involved, it should be considered that there are only two galaxies that are slightly above the irregularity threshold of σ_{PA} (Fig.11b&c). Therefore, although we discuss the possibility of these correlations being a result of cluster specific interaction mechanisms, this is not a strong result.

4.6. Comparison With High Redshift Studies

S08 uses a method that is based on kinemetry to distinguish merging and non-merging systems. They quantify the asymmetries in both the velocity field and the velocity dispersion map of ionized gas. Using the measurements of these two parameters for template galaxies, they determine where merging and non-merging systems are located on the plane of these parameters versus each other and define a criterion to distinguish them from one another: $K_{asym} = \sqrt{V_{asym}^2 + \sigma_{asym}^2} = 0.5$. We measured the V_{asym} parameter of our velocity fields (Table 7) and compared
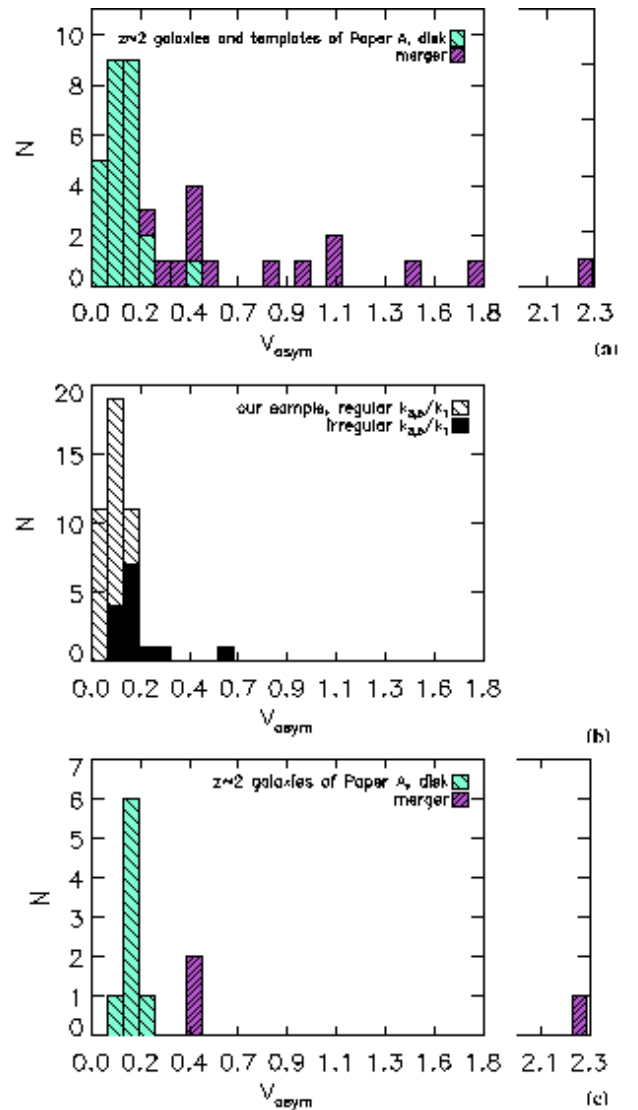

Fig. 12. Number distribution of the V_{asym} parameter that is described in S08. *a*: Galaxies and the templates in S08 that are classified as disk and merger. *b*: The galaxies in our sample that are classified as regular or irregular depending on their $k_{3,5}/k_1$ values. The galaxies that have doubtful $k_{3,5}/k_1$ values as explained in Paper III for the MS 0451 sample and here, in Sect. 3.8 for the rest are excluded from this histogram. *c*: $z \sim 2$ SINS galaxies in S08 that are classified as disk and merger.

these with the V_{asym} of the merging and non-merging galaxies and models in S08 (see Fig. 12). The quality of our sigma-maps is not satisfactory for an analysis. However, the possibility that σ_{asym} and V_{asym} give contradictory results is very low (see Fig. 5 in S08). Therefore, we use V_{asym} alone with the purpose of making a comparison between the methods. To measure a global ellipticity and a global inclination, which are used while measuring the V_{asym} parameter, we calculate the median of their values outside half the full width at half maximum of the seeing.

If we look at the V_{asym} distribution of our galaxies, we see that most of them are located in the region of the non-merging galaxies, as defined by S08 (Fig. 12a, b). V_{asym} is similar to $k_{3,5}/k_1$ and a comparison between these parameters for our galaxies shows that they correlate with each other (Fig. 13, correlation coefficient=0.86). On the other hand, the classification thresholds are quite different for the two criteria. Following S08,

Our analysis shows that distant field galaxies have more irregular gas kinematics than their local counterparts. This suggests a higher frequency of disk-building processes such as accretion events and mergers in the distant universe. Morphological properties of these galaxies lead us to the same conclusion. The concentration, the Gini coefficient and the M_{20} index measurements indicate that distant field galaxies are more clumpy and less centrally concentrated than local field galaxies.

We make a comparison between gas kinematics of our intermediate redshift sample and the $z \sim 2$ sample of S08 using the V_{asym} parameter, which is defined in S08 to distinguish merging and non merging systems. We find that our sample, that includes both field and cluster galaxies within $0.10 \leq z \leq 0.91$, have more regular gas kinematics than the $z \sim 2$ galaxies.

Y08 shows that a large fraction of spiral galaxies with $M_{stellar} \geq 1.5 \times 10^{10} M_{\odot}$ at $z = 0.4 - 0.75$ have irregular gas kinematics. When they exclude these galaxies with irregular kinematics, they find no evolution in the scatter and the slope of the K-band TFR (Puech et al. 2008). Our analysis shows that a large fraction of less massive distant spirals at a median redshift of $z = 0.36$ also have irregular gas kinematics.

We find that cluster and field galaxies are distributed in a similar manner in the (ir)regularity parameters space. We also measure the fraction of irregular velocity fields. For each parameter, we find remarkably similar fractions for cluster members and field galaxies. This shows that the cluster galaxies in our sample are not severely affected by the cluster environment. Galaxies in the central parts of clusters are expected to have an important fraction of their gas stripped via interaction processes and it is difficult to obtain velocity fields of these galaxies, especially at high redshifts. Therefore, it is probable that some cluster galaxies in our sample, for which the velocity fields could be analyzed, are just infalling. If this is the case, that explains the similarity we find between the gas kinematics of cluster and field galaxies. On the other hand, a comparison between the morphological properties of the cluster and field galaxies in our sample reveals a clear difference between them: the cluster sample lacks galaxies with low concentration index. This might be due to the activity of interaction processes such as harassment which causes matter to migrate towards the center. We compare the gas kinematics of spiral and irregular galaxies as well and find no significant difference between these morphological classes.

We find that galaxies with higher H_{α} luminosities have larger $k_{3,5}/k_1$ and σ_{PA} values. In addition to that, galaxies with more substructures have larger average misalignment between their kinematic and photometric axes ($\Delta\phi$). Since substructures mostly are star forming regions, all these correlations mean that galaxies which have more irregular gas kinematics have high star formation rates. This is consistent with the theory since most interaction mechanisms in clusters increase star formation activity at the beginning, before they eventually supress it.

Fig. 13. V_{asym} parameter that is described in S08 versus $k_{3,5}/k_1$. Data points that are far out of the general distribution are shown separately, on top of the main plot. # sign indicates the galaxies for which, both parameters are unreliable (see Sect. 3.8). These galaxies are not used in the correlation measurement.

most of our objects would be regular while many more galaxies are classified as irregular with our method. This is visible in Fig. 12 where the V_{asym} distribution of our galaxies is given together with non-mergers and mergers in S08. Classification of these galaxies according to the $k_{3,5}/k_1$ criterion is indicated on the same plot. While the method of S08 aims at separating mergers from non-mergers, it would not fulfill our requirement of tracing the imprints of environmental processes. 4F7 (in the non-merger region with V_{asym}=0.17) is a good example to explain that since the deviation of the position angle, the residual map of the velocity field and the simple rotating disk model and also the galaxy image itself provide signs of a merger.

We find that the $z \sim 2$ galaxies in S08 are more irregular than our complete sample that includes both cluster and field galaxies in $0.10 \leq z \leq 0.91$ (see Fig. 12b and c). The K-S test results show that the maximum deviation between these two distributions is 59% and the probability that the samples are similar is 0.002.

5. Summary and conclusions

Using gas velocity fields, we trace the activity of interaction processes both in galaxy clusters and in the field. To measure the irregularities in velocity fields, we use three different indicators: the standard deviation of the kinematic position angle (σ_{PA}), the mean deviation of the LOS velocity profile from a cosine function which is measured using high order Fourier terms ($k_{3,5}/k_1$) and the average misalignment between the kinematical and photometric major axes ($\Delta\phi$). A regularity threshold for each of these parameters is defined using local field galaxies from SINGS. 16 cluster members ($z \sim 0.3$ and $z \sim 0.5$) and 29 field galaxies (at $0.10 \leq z \leq 0.91$) are then analyzed and studied with respect to the local galaxies in the field and compared with each other to evaluate the effect of interaction processes on gas kinematics.

References

Abraham, R. G., Valdes, F., Yee, H. K. C., & van den Bergh, S. 1994, ApJ, 432, 75

Abraham, R. G., van den Bergh, S., Glazebrook, K., et al. 1996, ApJS, 107, 1

Abraham, R. G., van den Bergh, S., & Nair, P. 2003, ApJ, 588, 218

Aguerri, J. A. L., Balcells, M., & Peletier, R. F. 2001, A&A, 367, 428

Allen, S. W., Schmidt, R. W., Fabian, A. C., & Ebeling, H. 2003, MNRAS, 342, 287

Aragón-Salamanca, A. 2008, in IAU Symposium, Vol. 245, IAU Symposium, ed. M. Bureau, E. Athanassoula, & B. Barbuy, 285–288

Athreya, R. M., Mellier, Y., van Waerbeke, L., et al. 2002, A&A, 384, 743

Barton, E. J., Bromley, B. C., & Geller, M. J. 1999, ApJ, 511, L25

Bekki, K. & Couch, W. J. 2003, ApJ, 596, L13

Bekki, K. & Freeman, K. C. 2002, ApJ, 574, L21

Bell, E. F., Papovich, C., Wolf, C., et al. 2005, ApJ, 625, 23

Bessell, M. S. 1990, PASP, 102, 1181

Blanton, M. R. & Roweis, S. 2007, AJ, 133, 734

Borgani, S., Girardi, M., Carlberg, R. G., Yee, H. K. C., & Ellingson, E. 1999, ApJ, 527, 561

Boselli, A. & Gavazzi, G. 2006, PASP, 118, 517

Bravo-Alfaro, H., Brinks, E., Baker, A. J., Walter, F., & Kunth, D. 2004, AJ, 127, 264

Bravo-Alfaro, H., Cayatte, V., van Gorkom, J. H., & Balkowski, C. 2000, AJ, 119, 580

Burstein, D. 1979, ApJ, 234, 435

Butcher, H. & Oemler, Jr., A. 1978, ApJ, 226, 559

Butcher, H. & Oemler, Jr., A. 1984, ApJ, 285, 426

Byrd, G. & Valtonen, M. 1990, ApJ, 350, 89

Cardelli, J. A., Clayton, G. C., & Mathis, J. S. 1989, ApJ, 345, 245

Carlberg, R. G., Yee, H. K. C., Ellingson, E., et al. 1996, ApJ, 462, 32

Cayatte, V., Kotanyi, C., Balkowski, C., & van Gorkom, J. H. 1994, AJ, 107, 1003

Cohen, J. G. 1976, ApJ, 203, 587

Conselice, C. J., Bershady, M. A., & Jangren, A. 2000, ApJ, 529, 886

Couch, W. J., Balogh, M. L., Bower, R. G., et al. 2001, ApJ, 549, 820

Couch, W. J., Barger, A. J., Smail, I., Ellis, R. S., & Sharples, R. M. 1998, ApJ, 497, 188

Cowie, L. L. & Songaila, A. 1977, Nature, 266, 501

Daigle, O., Carignan, C., Amram, P., et al. 2006, MNRAS, 367, 469

Dale, D. A., Giovanelli, R., Haynes, M. P., Hardy, E., & Campusano, L. E. 2001, AJ, 121, 1886

Davies, R. D. & Lewis, B. M. 1973, MNRAS, 165, 231

De Propris, R., Conselice, C. J., Liske, J., et al. 2007, ApJ, 666, 212

Donahue, M. 1996a, in Astronomical Society of the Pacific Conference Series, Vol. 88, Clusters, Lensing, and the Future of the Universe, ed. V. Trimble & A. Reisenegger, 76–+

Donahue, M. 1996b, ApJ, 468, 79

Dressler, A. 1980, ApJ, 236, 351

Dressler, A. & Sandage, A. 1983, ApJ, 265, 664

Dressler, A., Smail, I., Poggianti, B. M., et al. 1999, ApJS, 122, 51

Elbaz, D., Daddi, E., Le Borgne, D., et al. 2007, A&A, 468, 33

Ellingson, E., Lin, H., Yee, H. K. C., & Carlberg, R. G. 2001, ApJ, 547, 609

Ellingson, E., Yee, H. K. C., Abraham, R. G., Morris, S. L., & Carlberg, R. G. 1998, ApJS, 116, 247

Evrard, A. E. 1991, MNRAS, 248, 8P

Fujita, Y. 1998, ApJ, 509, 587

Fujita, Y. & Nagashima, M. 1999, ApJ, 516, 619

Gavazzi, G. 1987, ApJ, 320, 96

Gavazzi, G. 1989, ApJ, 346, 59

Gavazzi, G., Contursi, A., Carrasco, L., et al. 1995, A&A, 304, 325

Giovanelli, R. & Haynes, M. P. 1985, ApJ, 292, 404

Giovanelli, R., Haynes, M. P., Salzer, J. J., et al. 1994, AJ, 107, 2036

Girardi, M. & Mezzetti, M. 2001, ApJ, 548, 79

Gisler, G. R. 1980, AJ, 85, 623

Goto, T., Okamura, S., Sekiguchi, M., et al. 2003, PASJ, 55, 757

Gottlöber, S., Klypin, A., & Kravtsov, A. V. 2001, ApJ, 546, 223

Gunn, J. E. & Gott, J. R. I. 1972, ApJ, 176, 1

Hibbard, J. E. & van Gorkom, J. H. 1996, AJ, 111, 655

Hinz, J. L., Rieke, G. H., & Caldwell, N. 2003, AJ, 126, 2622

Huchra, J. P. & Geller, M. J. 1982, ApJ, 257, 423

Ibata, R. A., Gilmore, G., & Irwin, M. J. 1994, Nature, 370, 194

Jäger, K., Ziegler, B. L., Böhm, A., et al. 2004, A&A, 422, 907 (Paper II)

Jeltema, T. E., Canizares, C. R., Bautz, M. W., & Buote, D. A. 2005, ApJ, 624, 606

Kapferer, W., Kronberger, T., Ferrari, C., Riser, T., & Schindler, S. 2008, MNRAS, 389, 1405

Kapferer, W., Sluka, C., Schindler, S., Ferrari, C., & Ziegler, B. 2009, A&A, 499, 87

Kelson, D. D. 2003, PASP, 115, 688

Kennicutt, Jr., R. C. 1992, ApJ, 388, 310

Kennicutt, Jr., R. C. 1998, ARA&A, 36, 189

Kennicutt, Jr., R. C., Armus, L., Bendo, G., et al. 2003, PASP, 115, 928

Kennicutt, Jr., R. C., Tamblyn, P., & Congdon, C. E. 1994, ApJ, 435, 22

Kidger, M. R. 2003, http://www.britastro.org/asteroids/USNO photometry.htm

Kneib, J. P., Mellier, Y., Pello, R., et al. 1995, A&A, 303, 27

Kodama, T. & Bower, R. G. 2001, MNRAS, 321, 18

Kodama, T. & Smail, I. 2001, MNRAS, 326, 637

Krajnović, D., Cappellari, M., de Zeeuw, P. T., & Copin, Y. 2006, MNRAS, 366, 787

Kronberger, T., Kapferer, W., Unterguggenberger, S., Schindler, S., & Ziegler, B. L. 2008, A&A, 483, 783

Kutdemir, E., Ziegler, B. L., Peletier, R. F., et al. 2008, A&A, 488, 117 (Paper III)

Lambas, D. G., Tissera, P. B., Alonso, M. S., & Coldwell, G. 2003, MNRAS, 346, 1189

Larson, R. B., Tinsley, B. M., & Caldwell, C. N. 1980, ApJ, 237, 692

Lewis, A. D., Ellingson, E., Morris, S. L., & Carlberg, R. G. 1999, ApJ, 517, 587

Lotz, J. M., Primack, J., & Madau, P. 2004, AJ, 128, 163

Luppino, G. A., Gioia, I. M., Hammer, F., Le Fèvre, O., & Annis, J. A. 1999, A&AS, 136, 117

Macciò, A. V., Moore, B., & Stadel, J. 2006, ApJ, 636, L25

Makino, J. & Hut, P. 1997, ApJ, 481, 83

Maschietto, F., Hatch, N. A., Venemans, B. P., et al. 2008, MNRAS, 389, 1223

Menanteau, F., Ford, H. C., Motta, V., et al. 2006, AJ, 131, 208

Mihos, J. C. 2004, in Clusters of Galaxies: Probes of Cosmological Structure and Galaxy Evolution, ed. J. S. Mulchaey, A. Dressler, & A. Oemler, 277–+

Milvang-Jensen, B., Noll, S., Halliday, C., et al. 2008, A&A, 482, 419

Monet et al., D. 1998, VizieR Online Data Catalog, 1252, 0

Moore, B., Ghigna, S., Governato, F., et al. 1997, ArXiv Astrophysics e-prints

Moore, B., Katz, N., Lake, G., Dressler, A., & Oemler, A. 1996, Nature, 379, 613

Moore, B., Lake, G., & Katz, N. 1998, ApJ, 495, 139

Moore, B., Lake, G., Quinn, T., & Stadel, J. 1999, MNRAS, 304, 465

Moran, S. M., Ellis, R. S., Treu, T., et al. 2007a, ApJ, 671, 1503

Moran, S. M., Miller, N., Treu, T., Ellis, R. S., & Smith, G. P. 2007b, ApJ, 659, 1138

Moustakas, J., Kennicutt, Jr., R. C., & Tremonti, C. A. 2006, ApJ, 642, 775

Neichel, B., Hammer, F., Puech, M., et al. 2008, A&A, 484, 159

Neistein, E., Maoz, D., Rix, H.-W., & Tonry, J. L. 1999, AJ, 117, 2666

Nulsen, P. E. J. 1982, MNRAS, 198, 1007

Okamoto, T. & Nagashima, M. 2001, ApJ, 547, 109

Patton, D. R., Carlberg, R. G., Marzke, R. O., et al. 2000, ApJ, 536, 153

Petrosian, A. R., Movsessian, T., Comte, G., Kunth, D., & Dodonov, S. 2002, A&A, 391, 487

Poggianti, B. M. 2006, in The Many Scales in the Universe: JENAM 2004 Astrophysics Reviews, ed. J. C. Del Toro Iniesta, E. J. Alfaro, J. G. Gorgas, E. Salvador-Sole, & H. Butcher, 71–+

Poggianti, B. M., Smail, I., Dressler, A., et al. 1999, ApJ, 518, 576

Puech, M., Flores, H., Hammer, F., et al. 2008, A&A, 484, 173

Quilis, V., Moore, B., & Bower, R. 2000, Science, 288, 1617

Richstone, D. O. 1976, ApJ, 204, 642

Rubin, V. C., Waterman, A. H., & Kenney, J. D. P. 1999, AJ, 118, 236

Salim, S., Rich, R. M., Charlot, S., et al. 2007, ApJS, 173, 267

Sancisi, R., Fraternali, F., Oosterloo, T., & van der Hulst, T. 2008, ARAA, 15, 189

Shapiro, K. L., Genzel, R., Förster Schreiber, N. M., et al. 2008, ApJ, 682, 231 (S08)

Sikkema, G. 2009, Phd thesis, Kapteyn Astronomical Institute, Groningen

Smail, I., Ellis, R. S., Dressler, A., et al. 1997, ApJ, 479, 70

Solanes, J. M., Manrique, A., García-Gómez, C., et al. 2001, ApJ, 548, 97

Stanford, S. A., Eisenhardt, P. R., Dickinson, M., Holden, B. P., & De Propris, R. 2002, ApJS, 142, 153

Stanonik, K., Platen, E., Aragón-Calvo, M. A., et al. 2009, ApJ, 696, L6

Stocke, J. T., Morris, S. L., Gioia, I. M., et al. 1991, ApJS, 76, 813

Teplitz, H. I., Malkan, M. A., Steidel, C. C., et al. 2000, ApJ, 542, 18

Tonry, J. L., Schmidt, B. P., Barris, B., et al. 2003, ApJ, 594, 1

Trujillo, I., Rudnick, G., Rix, H.-W., et al. 2004, ApJ, 604, 521

Tully, R. B. & Fouqué, P. 1985, ApJS, 58, 67

Tully, R. B., Pierce, M. J., Huang, J.-S., et al. 1998, AJ, 115, 2264

van den Bergh, S. 1976, ApJ, 206, 883

van Gorkom, J. & Schiminovich, D. 1997, in Astronomical Society of the Pacific Conference Series, Vol. 116, The Nature of Elliptical Galaxies; 2nd Stromlo Symposium, ed. M. Arnaboldi, G. S. Da Costa, & P. Saha, 310–+

Verdugo, M., Ziegler, B. L., & Gerken, B. 2008, A&A, 486, 9

Vogt, N. P., Haynes, M. P., Giovanelli, R., & Herter, T. 2004, AJ, 127, 3300

Wakker, B. P., York, D. G., Howk, J. C., et al. 2007, ApJL, 670, L113

Wakker, B. P., York, D. G., Wilhelm, R., et al. 2008, ApJ, 672, 298

Wright, E. L. 2006, PASP, 118, 1711

Yang, Y., Flores, H., Hammer, F., et al. 2008, A&A, 477, 789 (Y08)

Yee, H. K. C., Ellingson, E., Morris, S. L., Abraham, R. G., & Carlberg, R. G. 1998, ApJS, 116, 211

Ziegler, B. L., Böhm, A., Jäger, K., Heidt, J., & Möllenhoff, C. 2003, ApJL, 598, L87 (Paper I)

Online Material

Appendix A: Relations between kinematic (ir)regularity parameters
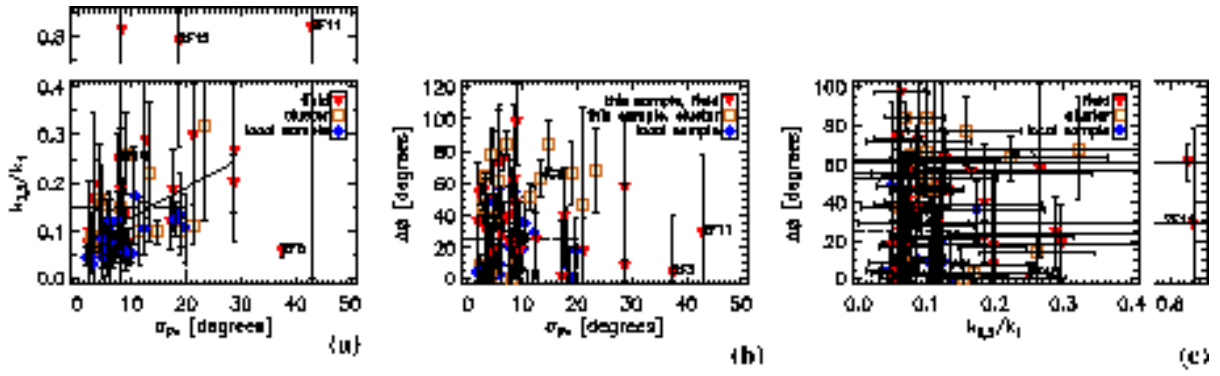
Fig. A.1. (Ir)regularity parameters versus each other. The regularity threshold of each parameter is shown with a dashed line. The galaxies in the local sample are used only for determination of the regularity thresholds as explained in Paper III. They are not used in correlation measurements. The galaxies that are excluded from the correlation as explained in Sect. 3.8 are indicated with their names on the plot. *a*: standard deviation of the kinematic position angle (σ_{PA}) versus mean $k_{3,5}/k_1$. The correlation we find between the two for our cluster+field sample (correlation coefficient=0.5) is indicated on the plot. Data points that are far out of the general distribution are shown separately, on top of the main plot. *b*: standard deviation of kinematic position angle (σ_{PA}) versus mean misalignment between kinematic and photometric axes ($\Delta\phi$). *c*: mean $k_{3,5}/k_1$ versus mean misalignment between kinematic and photometric axes ($\Delta\phi$). Data points that are far out of the general distribution are shown separately, on the right side of the main plot.

Appendix B: Individual galaxies

Here we present some figures showing the data and its analysis for each object in our sample. The HST image and the velocity field of each galaxy have the same orientation (the slit position is parallel to the *x*-axis). The velocities and the positions are given with respect to the continuum center of the galaxies.

B.1. Cluster galaxies
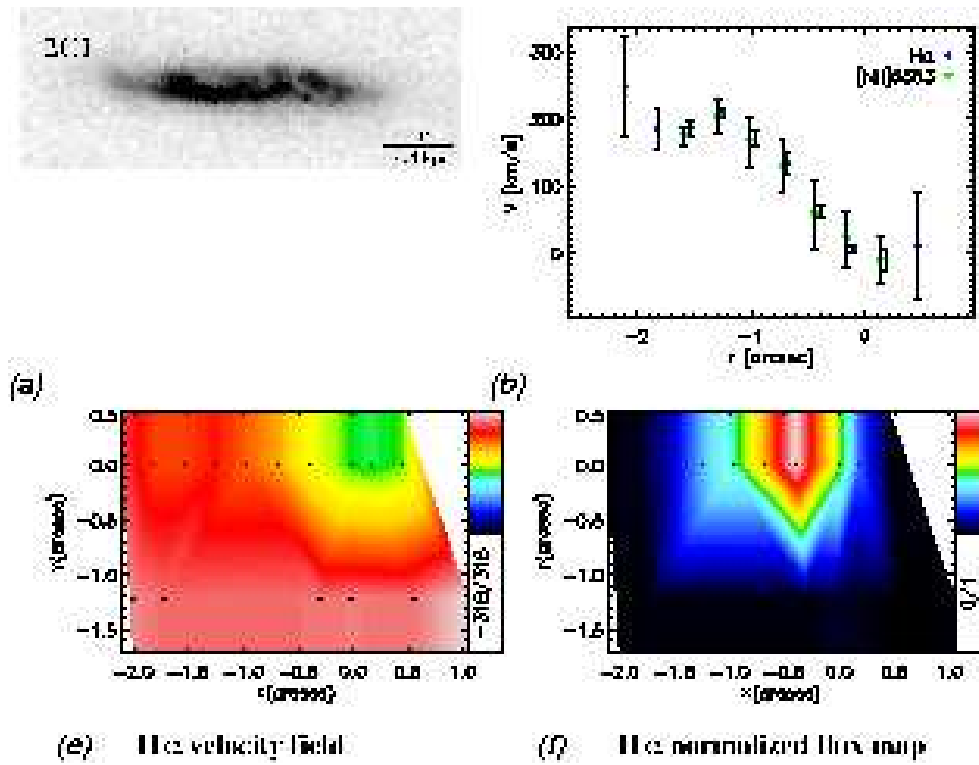
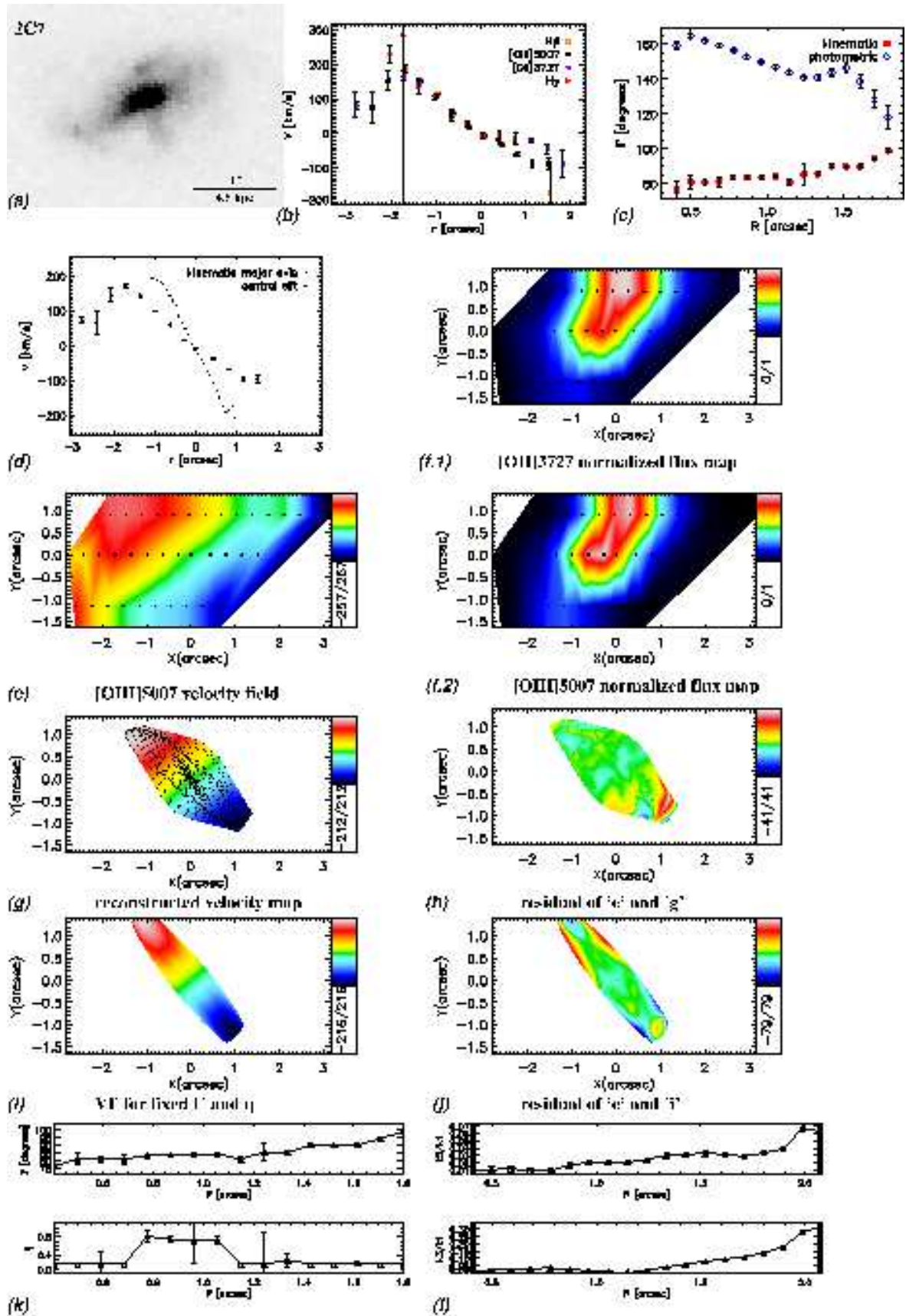**Fig. B.1. a)** HST-ACS image of the galaxy in the *V* band. **b)** Rotation curves of different emission lines extracted along the central slit. **e)** Hα velocity field. **f)** Normalized Hα flux map.
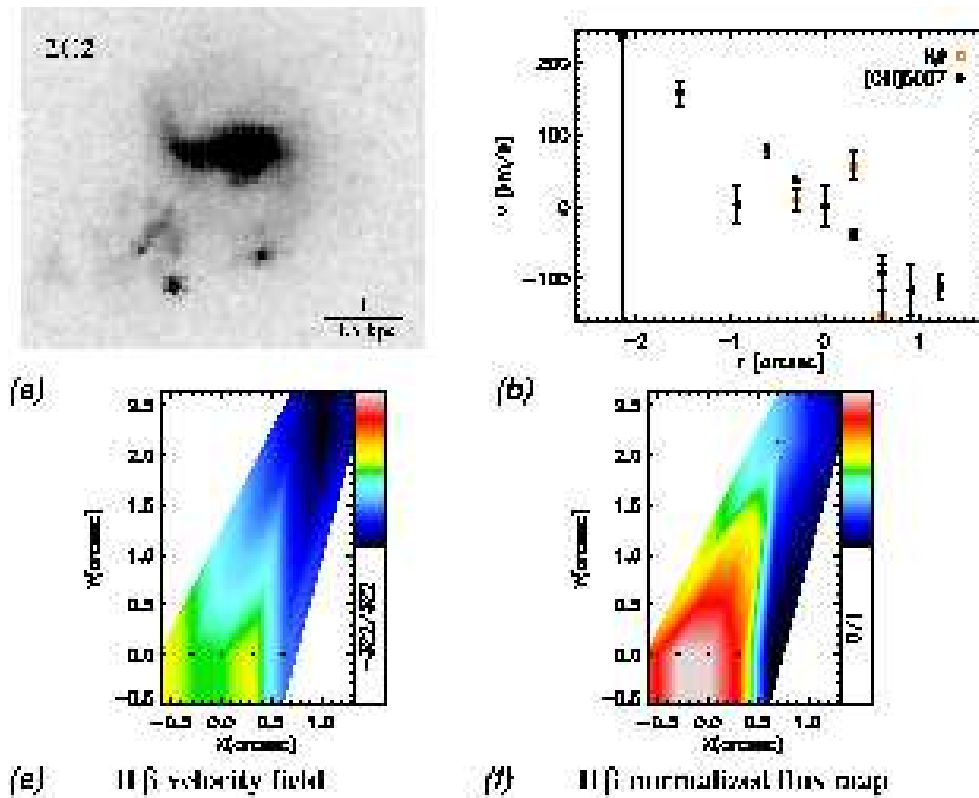
Fig. B.2. a) HST-ACS image of the galaxy in the *V* band. **b)** Rotation curves of different emission lines extracted along the central slit. **e)** Hβ velocity field. **f)** Normalized Hβ flux map.
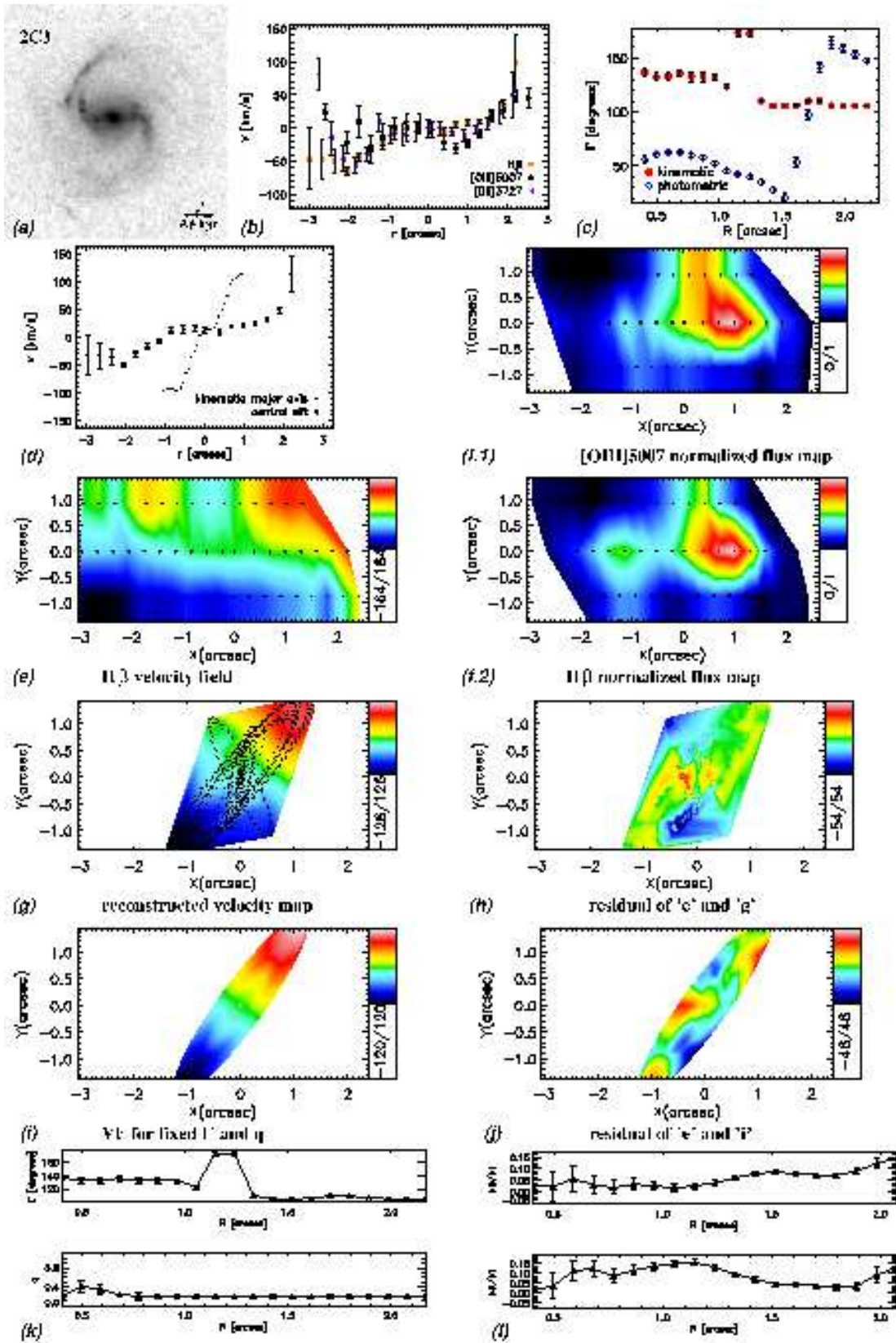
Fig. B.3. a) HST-ACS image of the galaxy in the *V* band. **b)** Rotation curves of different emission lines extracted along the central slit. **c)** Position angles of kinematic and photometric axes as a function of radius. **d)** Rotation curves extracted along the central slit and the kinematic major axis. **e)** Hβ velocity field. **f.1)** Normalized [OIII]5007 flux map. **f.2)** Normalized Hβ flux map. **g)** Velocity map reconstructed using 6 harmonic terms. **h)** Residual of the velocity map and the reconstructed map. **i)** Simple rotation map constructed for position angle and ellipticity fixed to their global values. **j)** Residual of the velocity map and the simple rotation map. **k)** Position angle and flattening as a function of radius. **l)** k_3/k_1 and k_5/k_1 (from the analysis where position angle and ellipticity are fixed to their global values) as a function of radius.
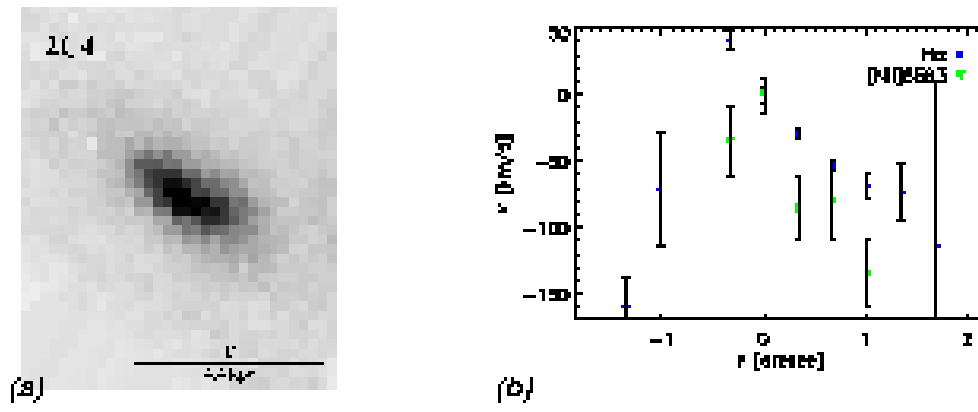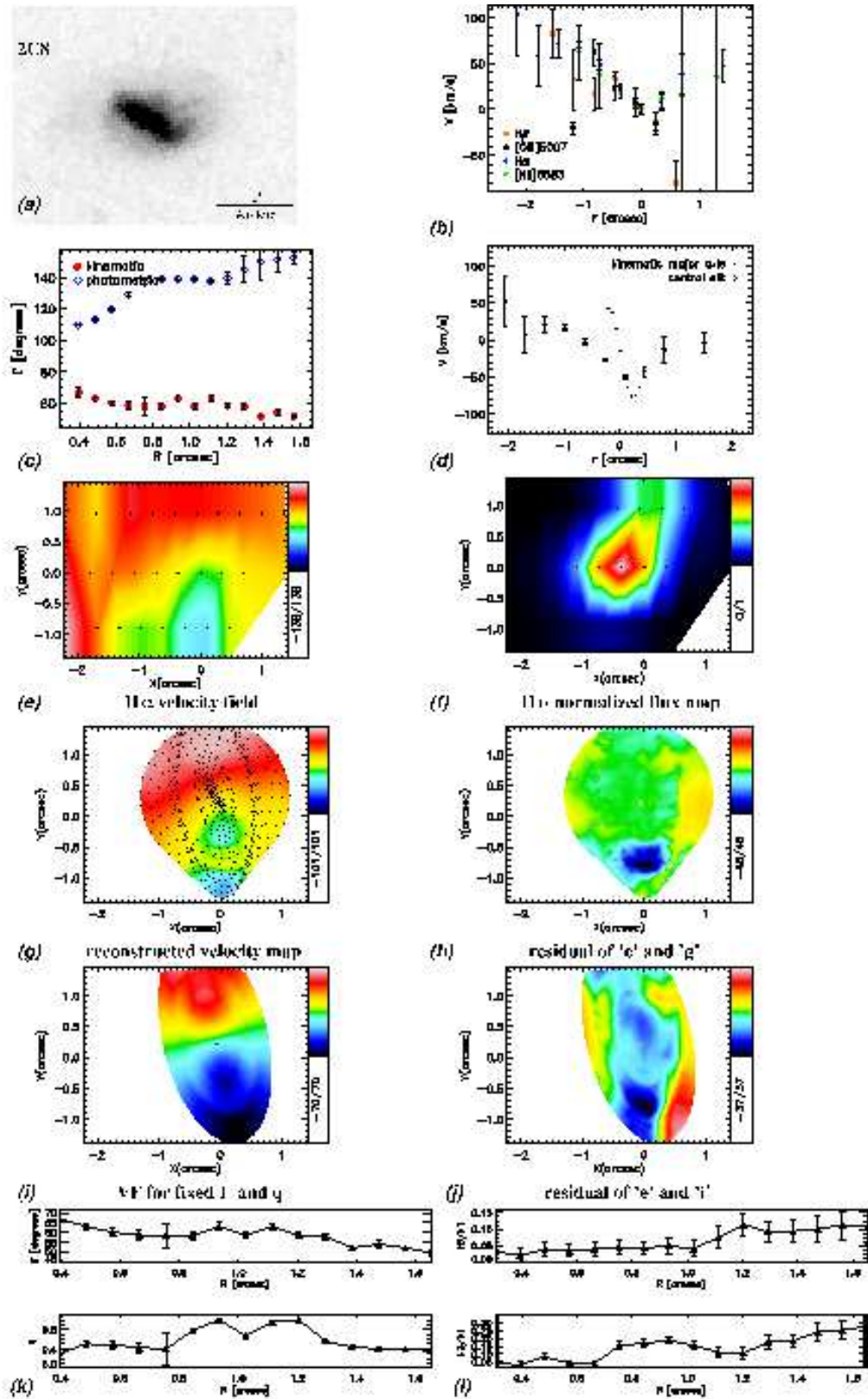
Fig. B.4. a) HST-ACS image of the galaxy in the *V* band. **b)** Rotation curves of different emission lines extracted along the centralslit.

Fig. B.5. a) HST-ACS image of the galaxy in the *V* band. **b)** Rotation curves of different emission lines extracted along the central slit. **c)** Position angles of kinematic and photometric axes as a function of radius. **d)** Rotation curves extracted along the central slit and the kinematic major axis. **e)** Hβ velocity field. **f)** Normalized Hβ flux map. **g)** Velocity map reconstructed using 6 harmonic terms. **h)** Residual of the velocity map and the reconstructed map. **i)** Simple rotation map constructed for position angle and ellipticity fixed to their global values. **j)** Residual of the velocity map and the simple rotation map. **k)** Position angle and flattening as a function of radius. **l)** k_3/k_1 and k_5/k_1 (from the analysis where position angle and ellipticity are fixed to their global values) as a function of radius.
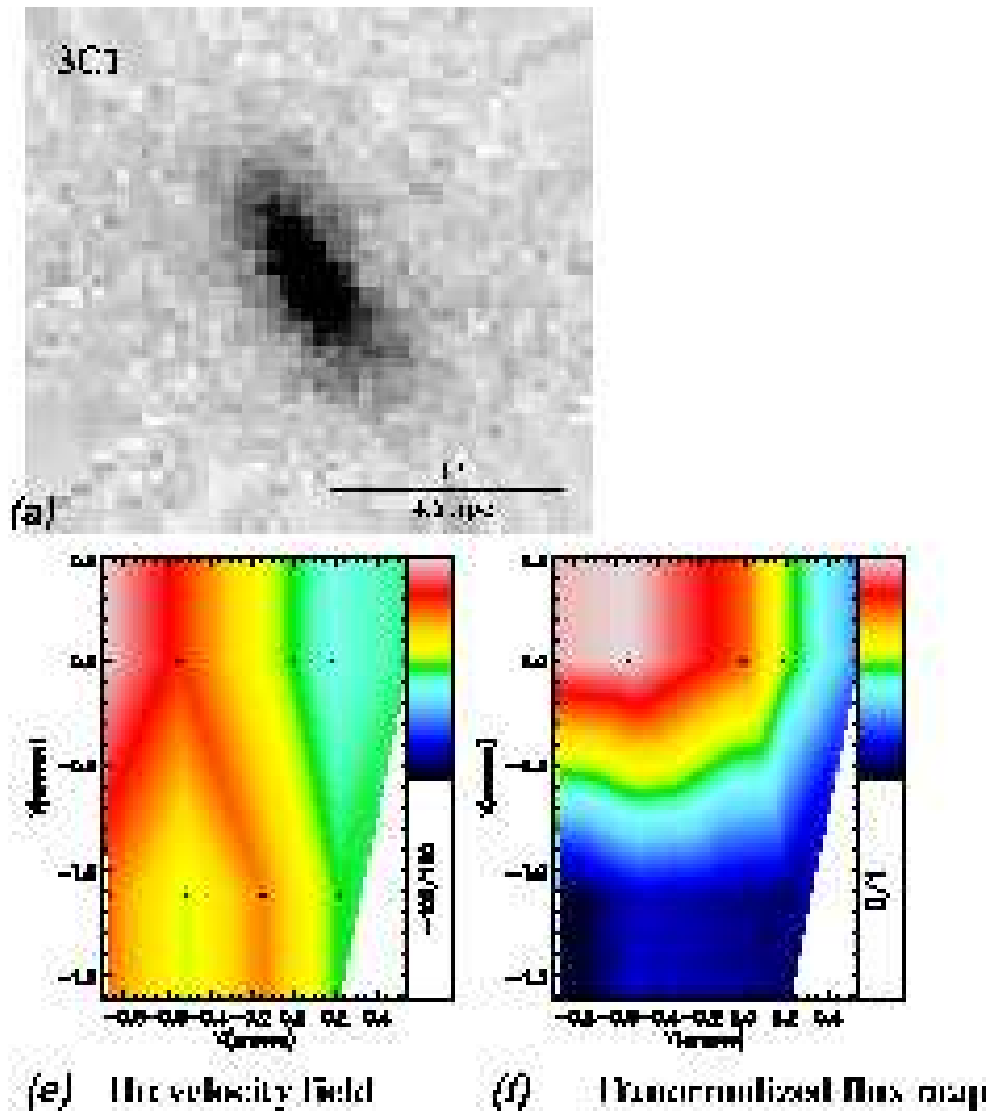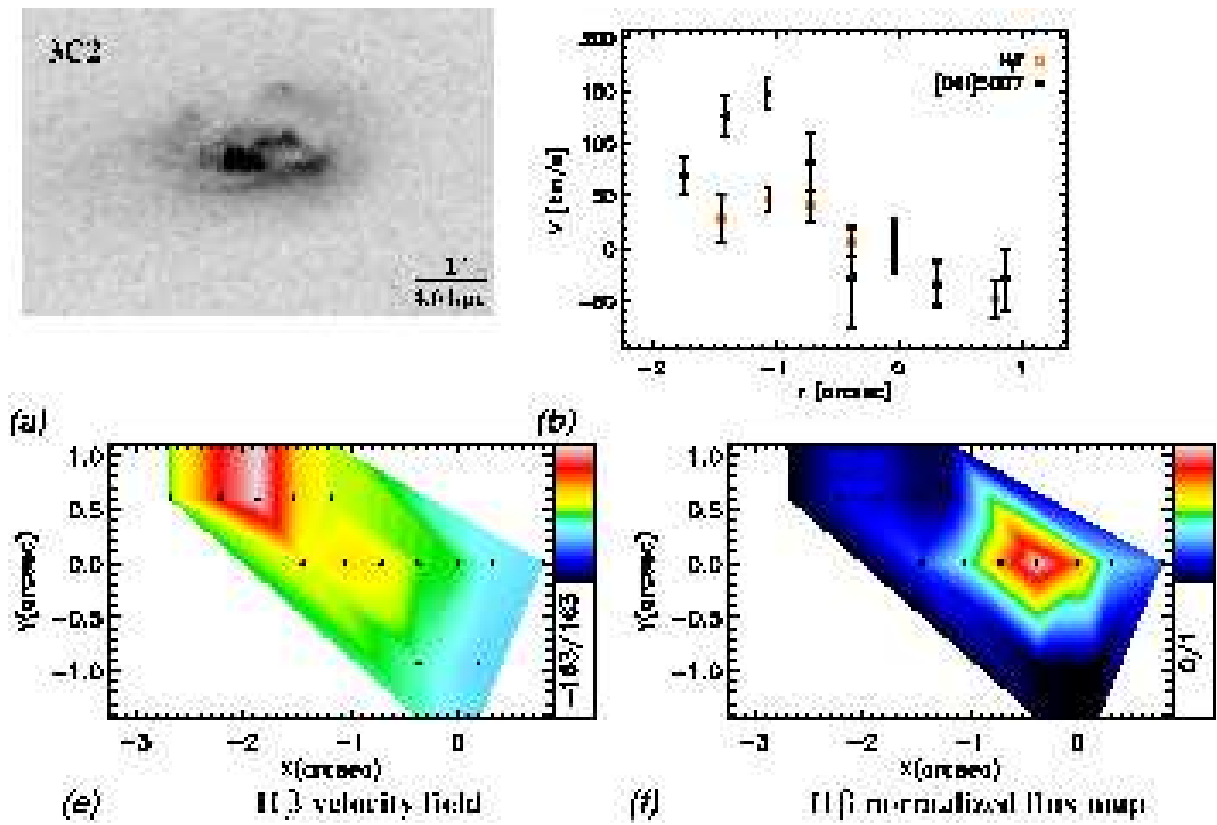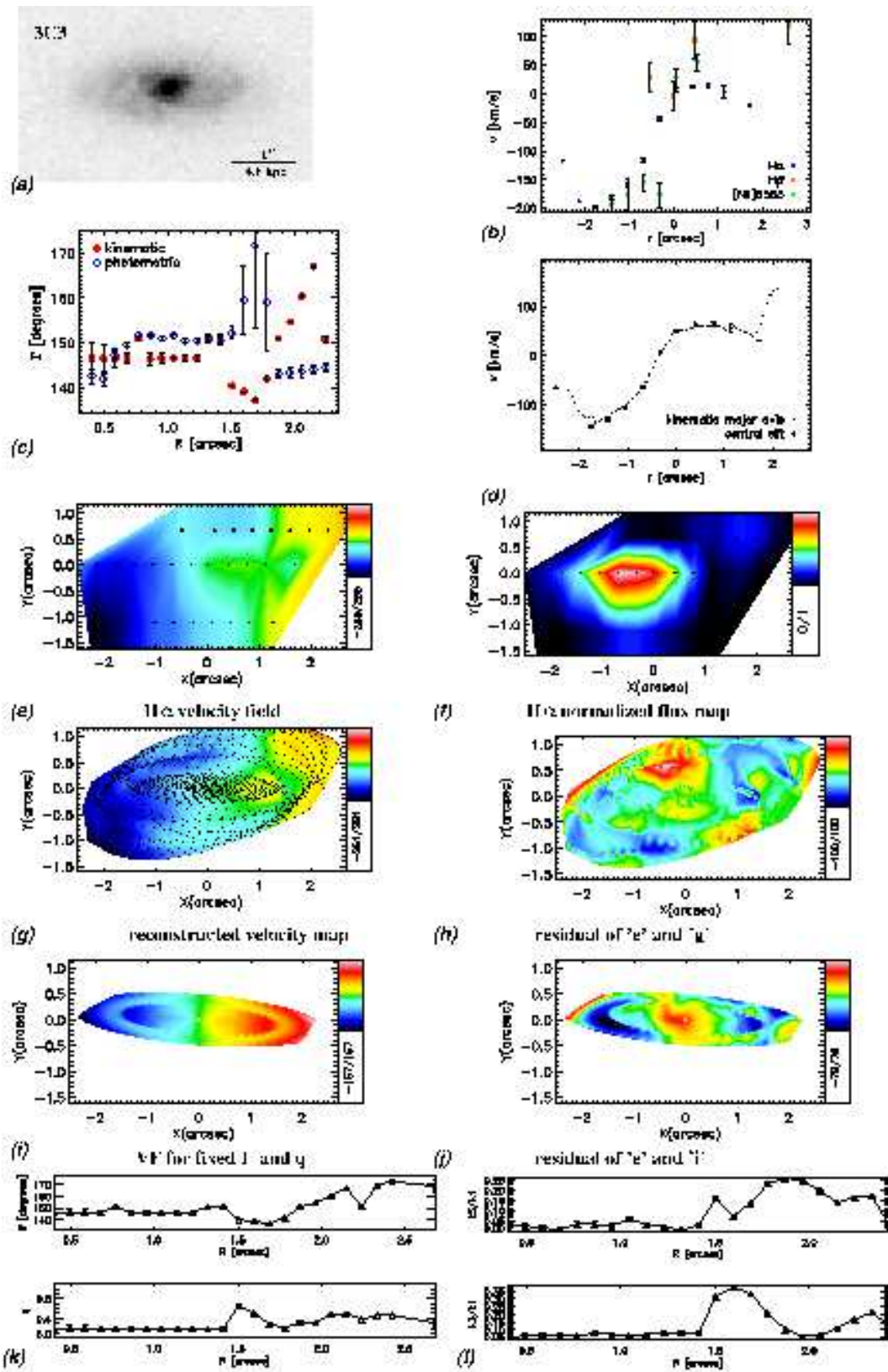
Fig. B.6. a) HST-ACS image of the galaxy in the *V* band. **b)** Rotation curves of different emission lines extracted along the central slit. **c)** Position angles of kinematic and photometric axes as a function of radius. **d)** Rotation curves extracted along the central slit and the kinematic major axis. **e)** [OII]3727 velocity field. **f)** Normalized [OII]3727 flux map. **g)** Velocity map reconstructed using 6 harmonic terms. **h)** Residual of the velocity map and the reconstructed map. **i)** Simple rotation map constructed for position angle and ellipticity fixed to their global values. **j)** Residual of the velocity map and the simple rotation map. **k)** Position angle and flattening as a function of radius. **l)** k_3/k_1 and k_5/k_1 (from the analysis where position angle and ellipticity are fixed to their global values) as a function of radius.

Fig. B.7. a) HST-ACS image of the galaxy in the *V* band. **b)** Rotation curves of different emission lines extracted along the central slit. **c)** Position angles of kinematic and photometric axes as a function of radius. **d)** Rotation curves extracted along the central slit and the kinematic major axis. **e)** [OIII]5007 velocity field. **f.1)** Normalized [OII]3727 flux map. **f.2)** Normalized [OIII]5007 flux map. **g)** Velocity map reconstructed using 6 harmonic terms. **h)** Residual of the velocity map and the reconstructed map. **i)** Simple rotation map constructed for position angle and ellipticity fixed to their global values. **j)** Residual of the velocity map and the simple rotation map. **k)** Position angle and flattening as a function of radius. **l)** k_3/k_1 and k_5/k_1 (from the analysis where position angle and ellipticity are fixed to their global values) as a function of radius.
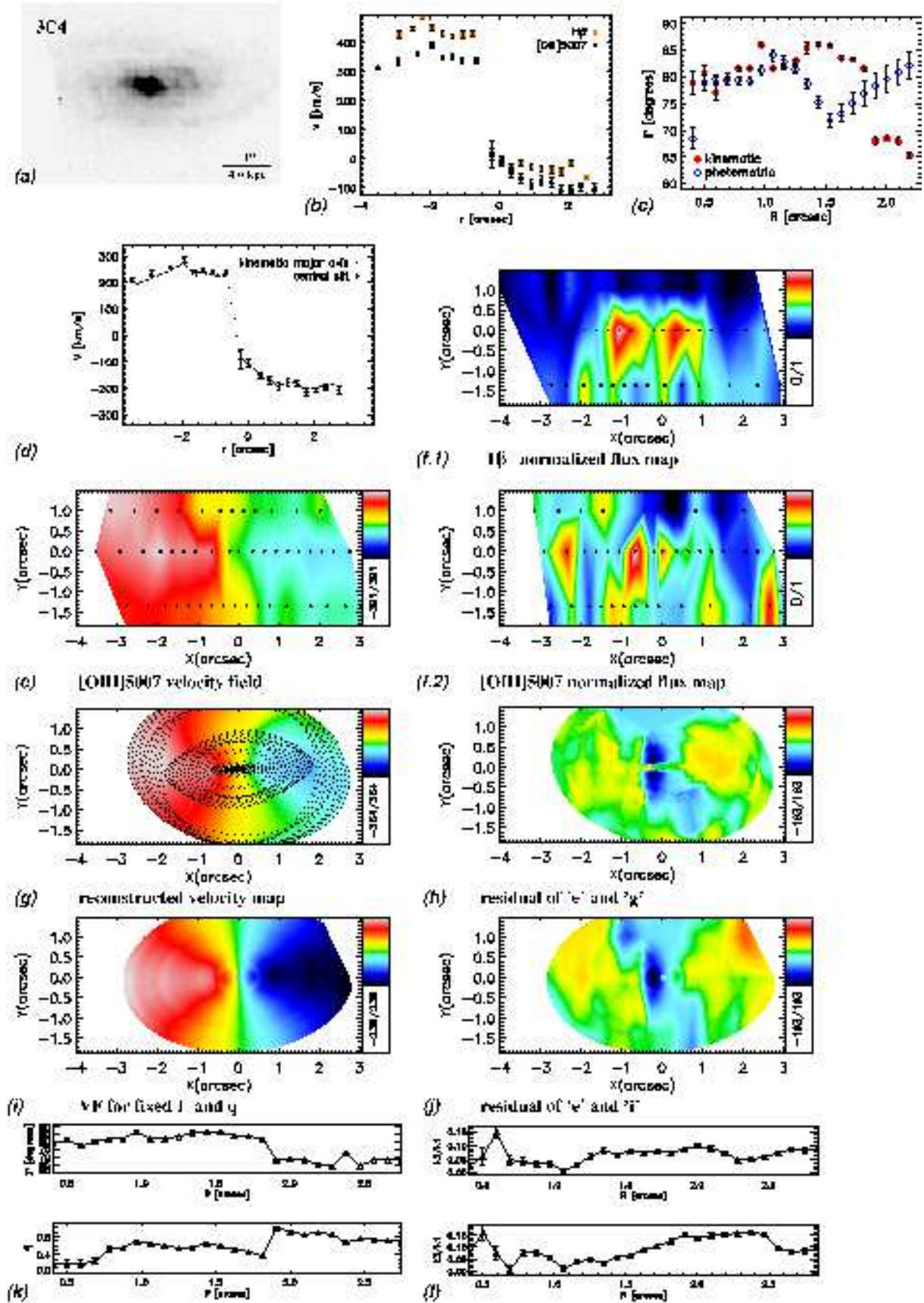
Fig. B.8. a) HST-ACS image of the galaxy in the *V* band. **b)** Rotation curves of different emission lines extracted along the central slit. **c)** Position angles of kinematic and photometric axes as a function of radius. **d)** Rotation curves extracted along the central slit and the kinematic major axis. **e)** Hα velocity field. **f)** Normalized Hα flux map. **g)** Velocity map reconstructed using 6 harmonic terms. **h)** Residual of the velocity map and the reconstructed map. **i)** Simple rotation map constructed for position angle and ellipticity fixed to their global values. **j)** Residual of the velocity map and the simple rotation map. **k)** Position angle and flattening as a function of radius. **l)** k_3/k_1 and k_5/k_1 (from the analysis where position angle and ellipticity are fixed to their global values) as a function of radius.
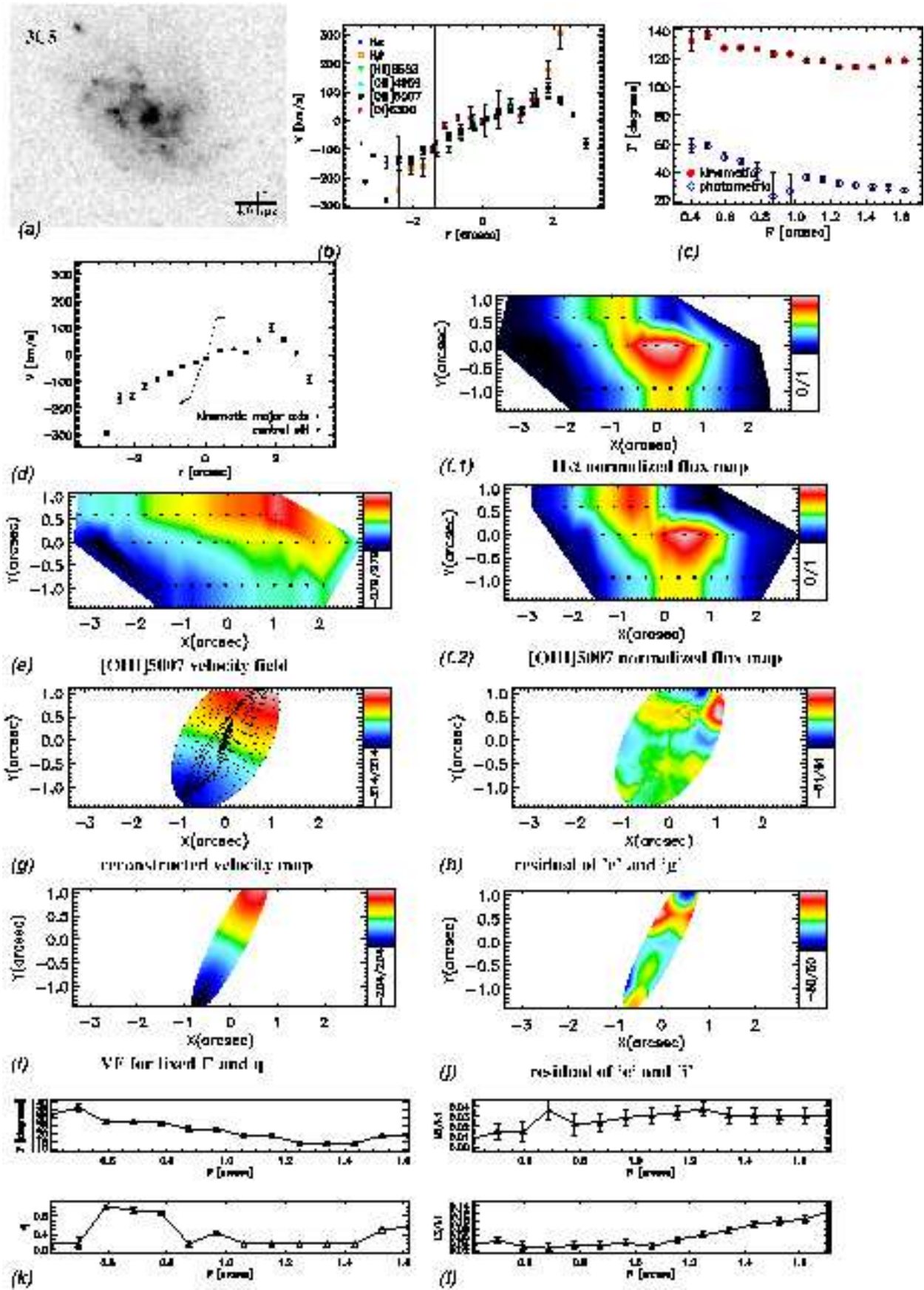
Fig. B.9. a) HST-ACS image of the galaxy in the *V* band. **e)** Hα velocity field. **f)** Normalized Hα flux map.

Fig. B.10. a) HST-ACS image of the galaxy in the *V* band. **b)** Rotation curves of different emission lines extracted along the central slit. **e)** Hβ velocity field. **f)** Normalized Hβ flux map.

Fig. B.11. a) HST-ACS image of the galaxy in the *V* band. **b)** Rotation curves of different emission lines extracted along the central slit. **c)** Position angles of kinematic and photometric axes as a function of radius. **d)** Rotation curves extracted along the central slit and the kinematic major axis. **e)** Hα velocity field. **f)** Normalized Hα flux map. **g)** Velocity map reconstructed using 6 harmonic terms. **h)** Residual of the velocity map and the reconstructed map. **i)** Simple rotation map constructed for position angle and ellipticity fixed to their global values. **j)** Residual of the velocity map and the simple rotation map. **k)** Position angle and flattening as a function of radius. **l)** k_3/k_1 and k_5/k_1 (from the analysis where position angle and ellipticity are fixed to their global values) as a function of radius.
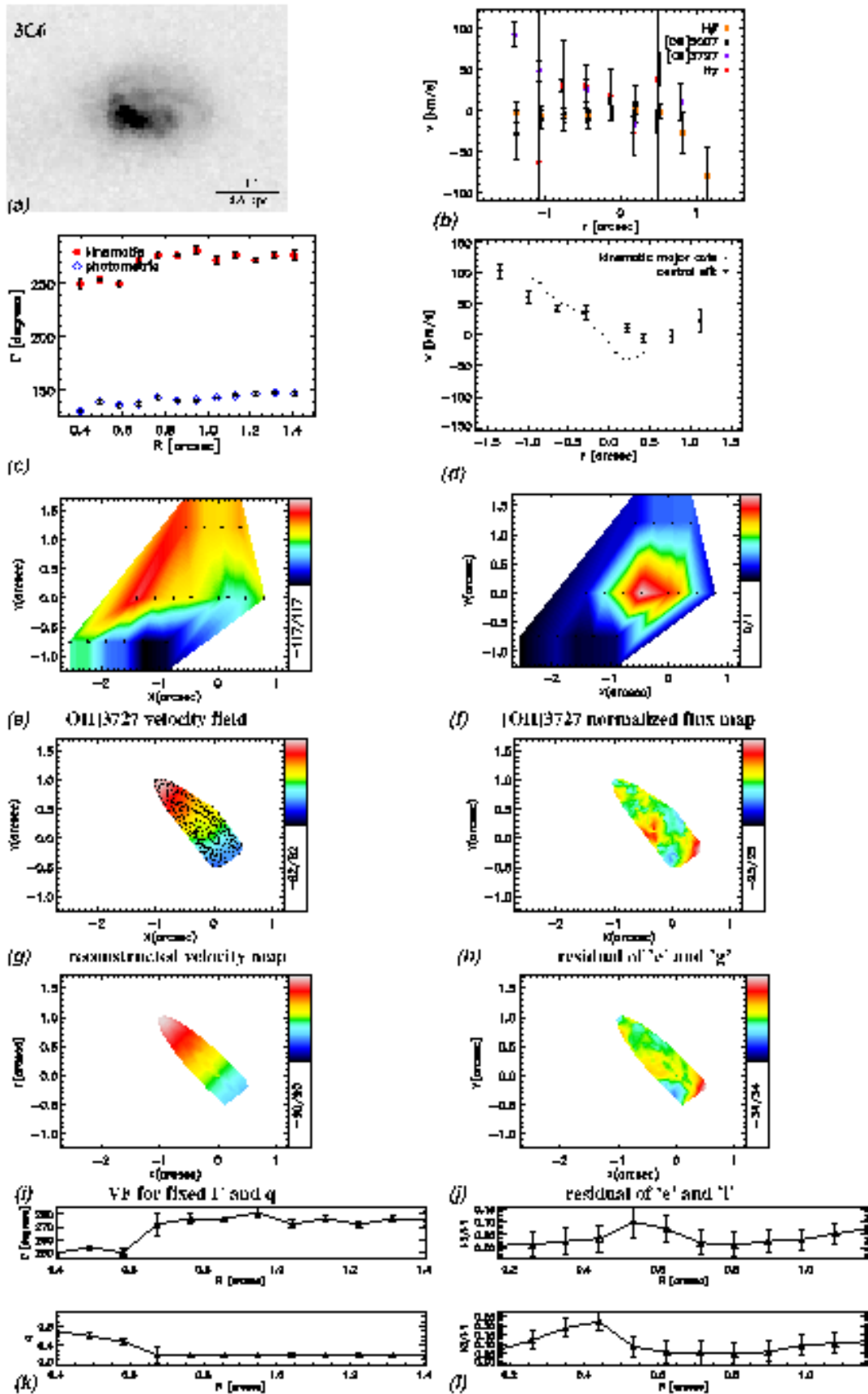
Fig. B.12. a) HST-ACS image of the galaxy in the *V* band. **b)** Rotation curves of different emission lines extracted along the central slit. **c)** Position angles of kinematic and photometric axes as a function of radius. **d)** Rotation curves extracted along the central slit and the kinematic major axis. **e)** [OIII]5007 velocity field. **f.1)** Normalized Hβ flux map. **f.2)** Normalized [OIII]5007 flux map. **g)** Velocity map reconstructed using 6 harmonic terms. **h)** Residual of the velocity map and the reconstructed map. **i)** Simple rotation map constructed for position angle and ellipticity fixed to their global values. **j)** Residual of the velocity map and the simple rotation map. **k)** Position angle and flattening as a function of radius. **l)** k_3/k_1 and k_5/k_1 (from the analysis where position angle and ellipticity are fixed to their global values) as a function of radius.
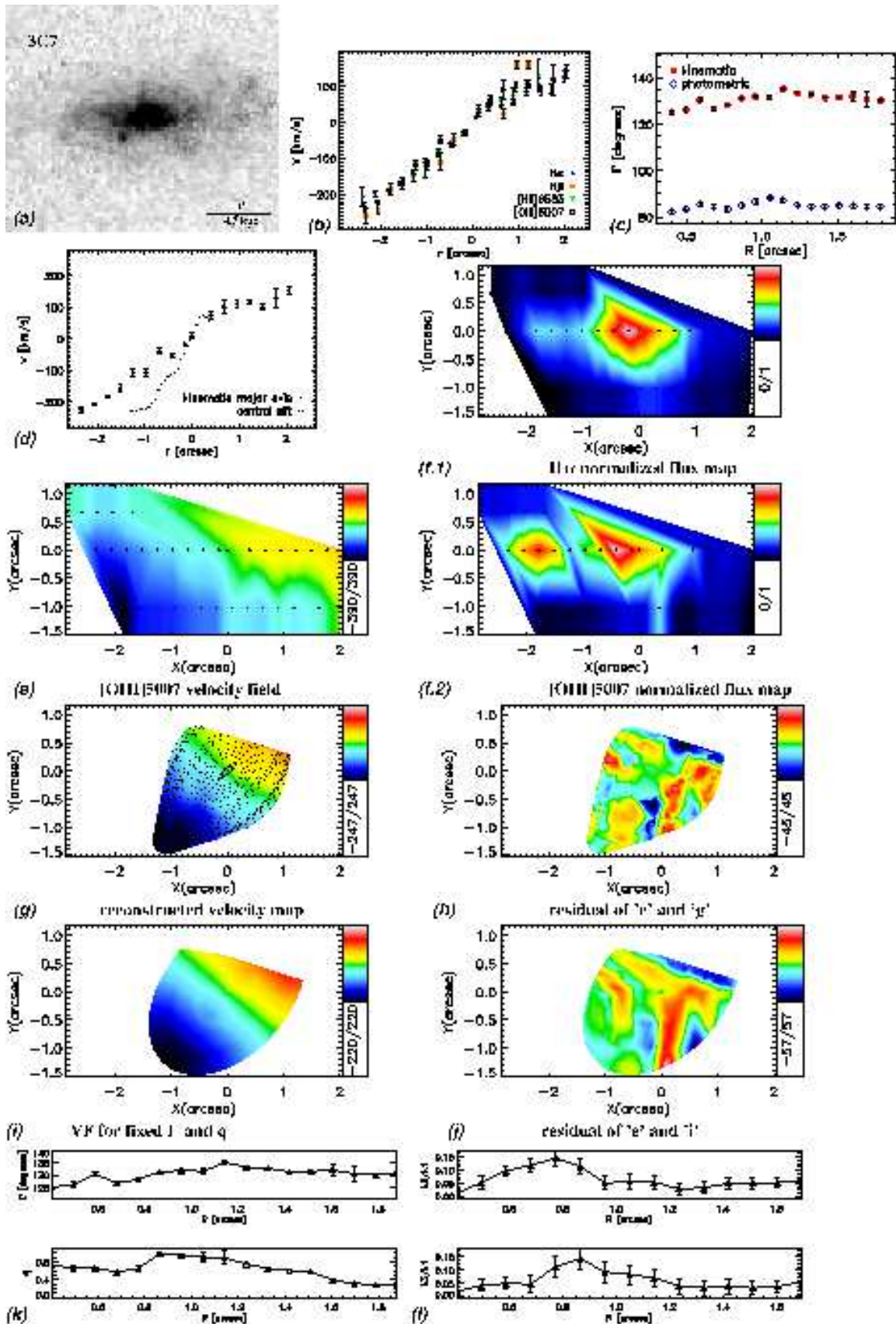
Fig. B.13. a) HST-ACS image of the galaxy in the *V* band. **b)** Rotation curves of different emission lines extracted along the central slit. **c)** Position angles of kinematic and photometric axes as a function of radius. **d)** Rotation curves extracted along the central slit and the kinematic major axis. **e)** [OIII]5007 velocity field. **f.1)** Normalized Hα flux map. **f.2)** Normalized [OIII]5007 flux map. **g)** Velocity map reconstructed using 6 harmonic terms. **h)** Residual of the velocity map and the reconstructed map. **i)** Simple rotation map constructed for position angle and ellipticity fixed to their global values. **j)** Residual of the velocity map and the simple rotation map. **k)** Position angle and flattening as a function of radius. **l)** k_3/k_1 and k_5/k_1 (from the analysis where position angle and ellipticity are fixed to their global values) as a function of radius.
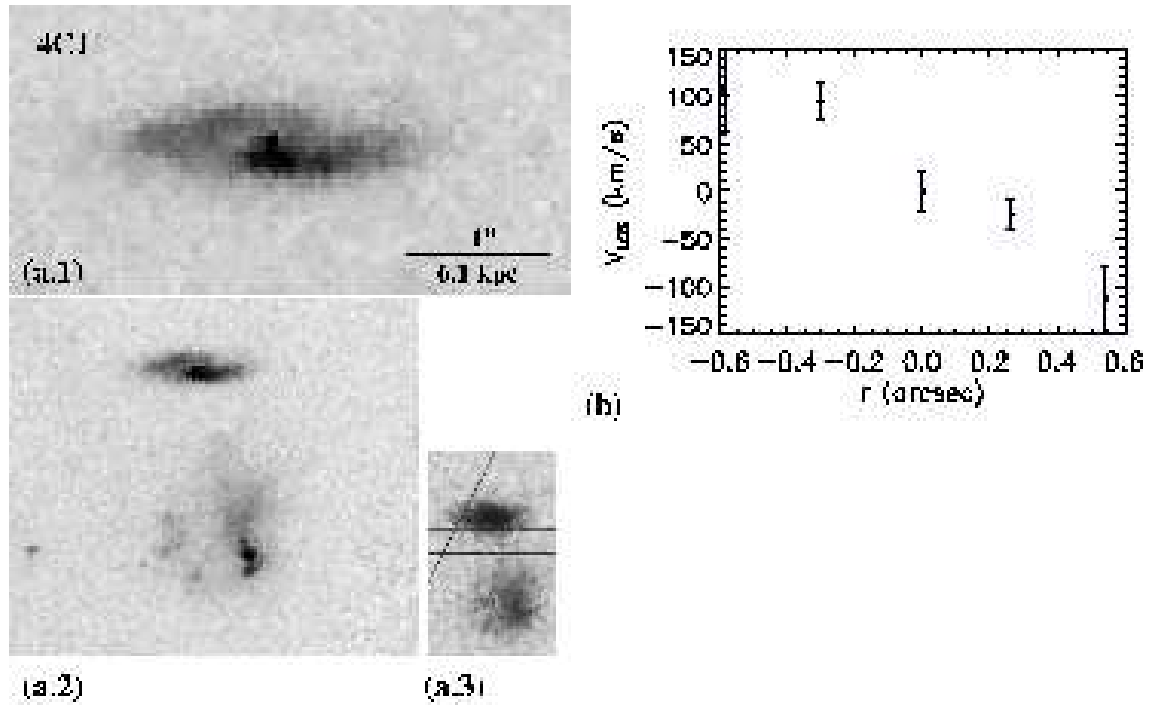
Fig. B.14. a) HST-ACS image of the galaxy in the *V* band. **b)** Rotation curves of different emission lines extracted along the central slit. **c)** Position angles of kinematic and photometric axes as a function of radius. **d)** Rotation curves extracted along the central slit and the kinematic major axis. **e)** [OII]3727 velocity field. **f)** Normalized [OII]3727 flux map. **g)** Velocity map reconstructed using 6 harmonic terms. **h)** Residual of the velocity map and the reconstructed map. **i)** Simple rotation map constructed for position angle and ellipticity fixed to their global values. **j)** Residual of the velocity map and the simple rotation map. **k)** Position angle and flattening as a function of radius. **l)** k_3/k_1 and k_5/k_1 (from the analysis where position angle and ellipticity are fixed to their global values) as a function of radius.
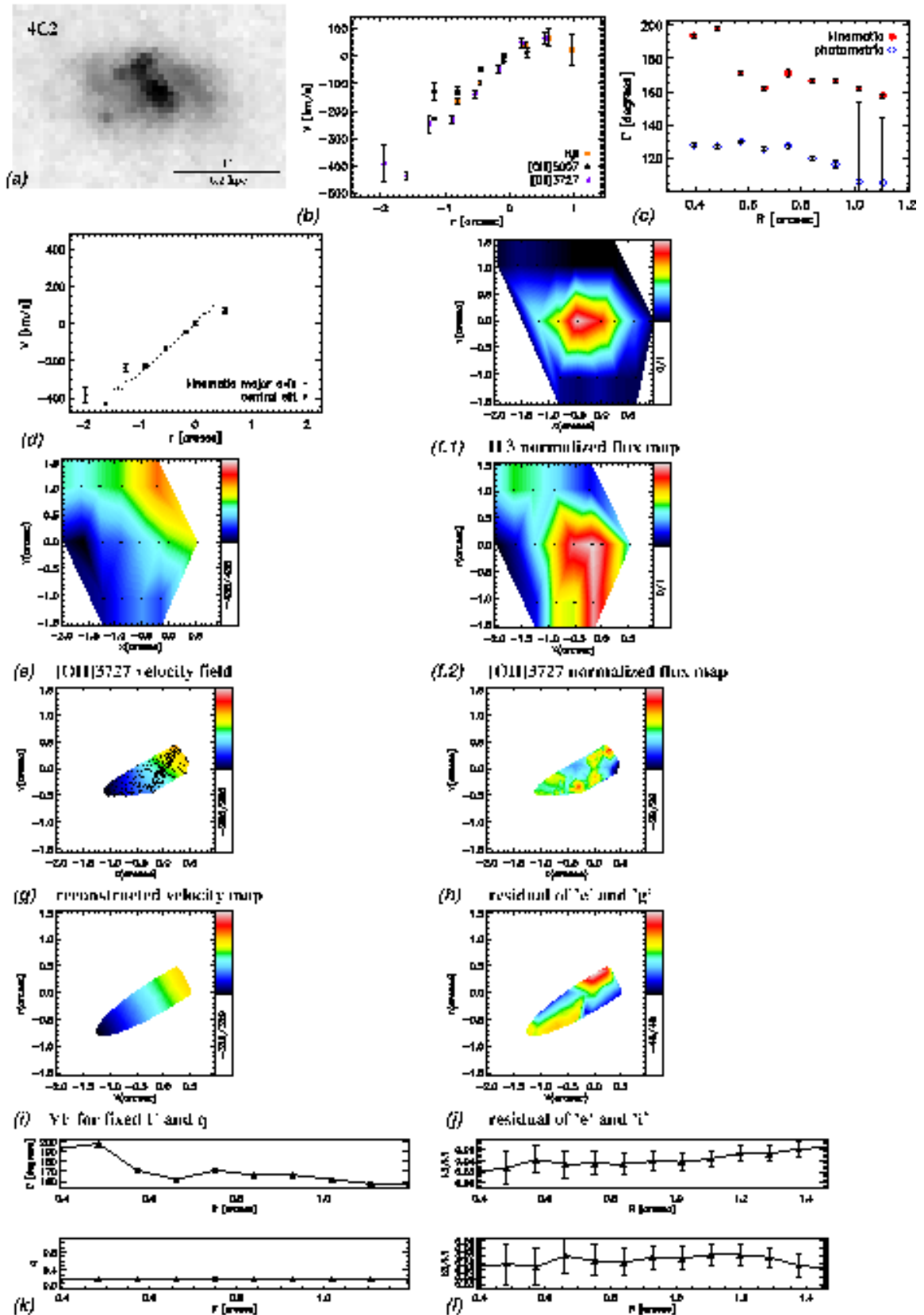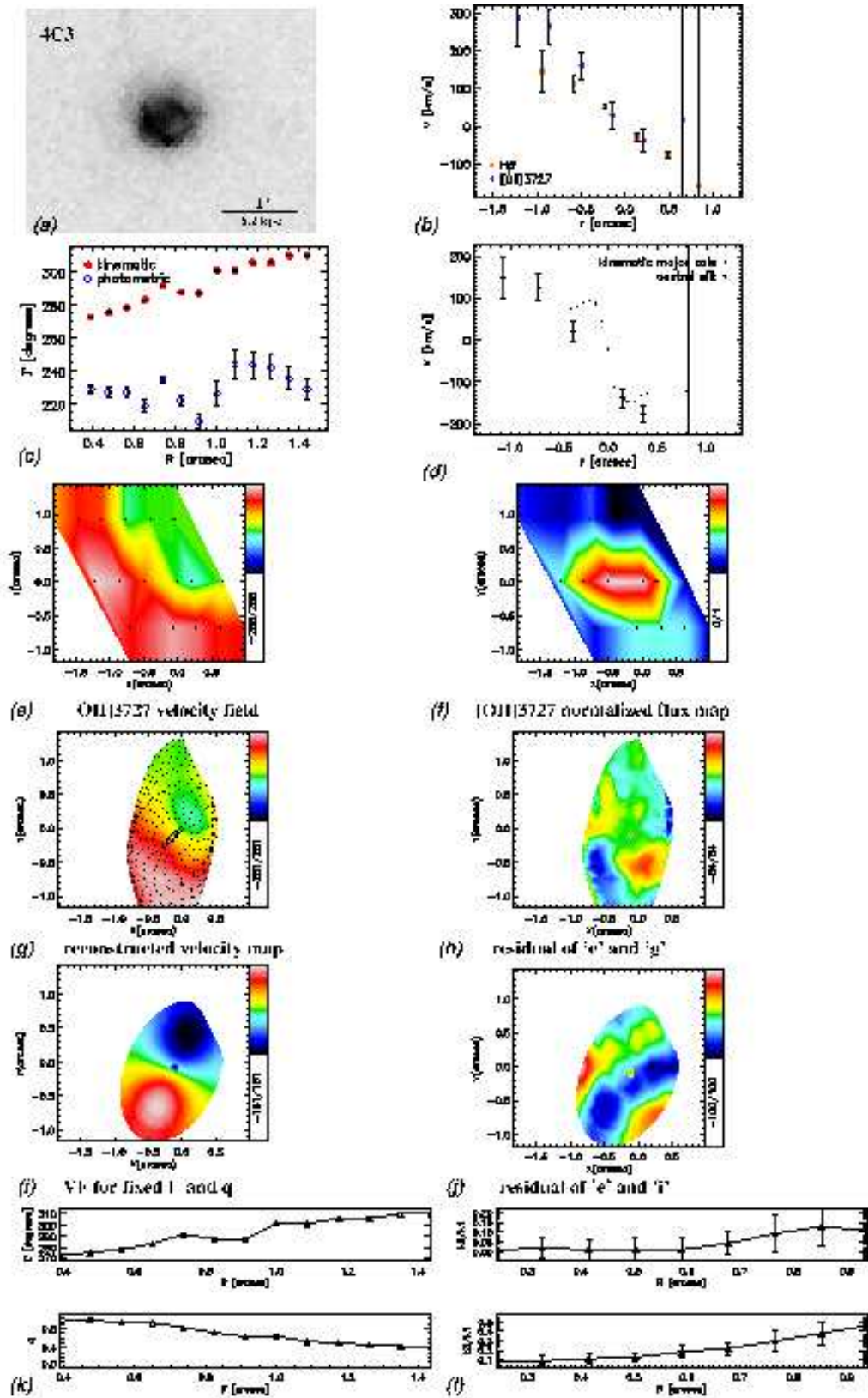
Fig. B.15. **a)** HST-ACS image of the galaxy in the *V* band. **b)** Rotation curves of different emission lines extracted along the central slit. **c)** Position angles of kinematic and photometric axes as a function of radius. **d)** Rotation curves extracted along the central slit and the kinematic major axis. **e)** [OIII]5007 velocity field. **f.1)** Normalized Hα flux map. **f.2)** Normalized [OIII]5007 flux map. **g)** Velocity map reconstructed using 6 harmonic terms. **h)** Residual of the velocity map and the reconstructed map. **i)** Simple rotation map constructed for position angle and ellipticity fixed to their global values. **j)** Residual of the velocity map and the simple rotation map. **k)** Position angle and flattening as a function of radius. **l)** k_3/k_1 and k_5/k_1 (from the analysis where position angle and ellipticity are fixed to their global values) as a function of radius.

Fig. B.16. a.1) HST-ACS image of the galaxy in the *V* band. **a.2)** This cluster galaxy does not have emission lines. The spectra include an emission line from the galaxy below the target that is seen in the HST image. The redshift of this galaxy could not be determined from the composite spectrum. **a.3)** FORS2 image of the galaxies. Parallel lines represent the bottom slit which gives a composite spectrum of both galaxies together. **b)** Rotation curve of the galaxy that is below the target. It is obtained from the slit positioned inbetween the two galaxies (see a.3). Velocities were measured with respect to the velocity at the continuum center of the bottom slit. Signal level in the other two slits was not high enough to obtain a rotation curve.

Fig. B.17. a) HST-ACS image of the galaxy in the *V* band. **b)** Rotation curves of different emission lines extracted along the central slit. **c)** Position angles of kinematic and photometric axes as a function of radius. **d)** Rotation curves extracted along the central slit and the kinematic major axis. **e)** [OII]3727 velocity field. **f.1)** Normalized Hβ flux map. **f.2)** Normalized [OII]3727 flux map. **g)** Velocity map reconstructed using 6 harmonic terms. **h)** Residual of the velocity map and the reconstructed map. **i)** Simple rotation map constructed for position angle and ellipticity fixed to their global values. **j)** Residual of the velocity map and the simple rotation map. **k)** Position angle and flattening as a function of radius. **l)** k_3/k_1 and k_5/k_1 (from the analysis where position angle and ellipticity are fixed to their global values) as a function of radius.
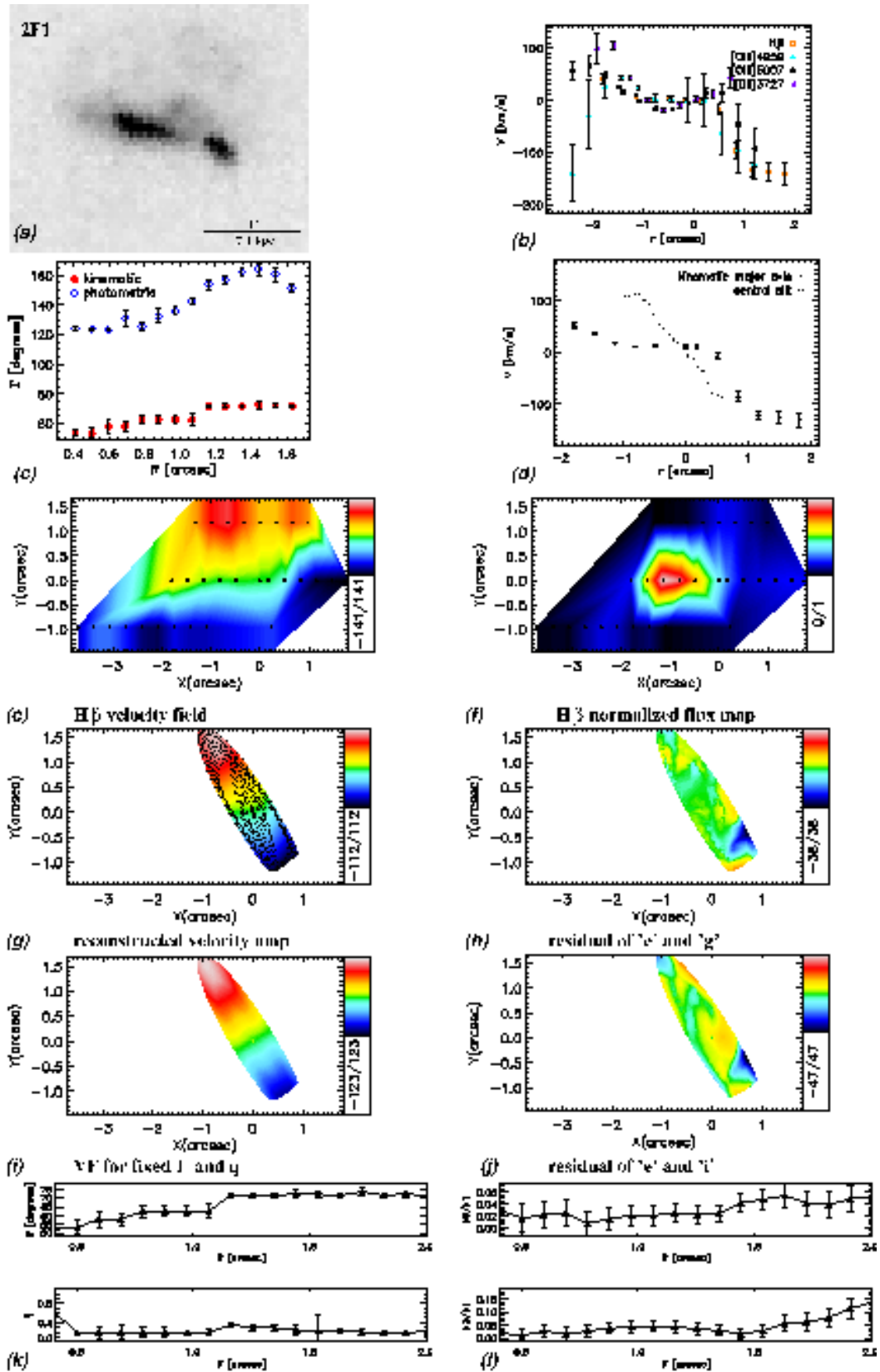
Fig. B.18. a) HST-ACS image of the galaxy in the *V* band. **b)** Rotation curves of different emission lines extracted along the central slit. **c)** Position angles of kinematic and photometric axes as a function of radius. **d)** Rotation curves extracted along the central slit and the kinematic major axis. **e)** [OII]3727 velocity field. **f)** Normalized [OII]3727 flux map. **g)** Velocity map reconstructed using 6 harmonic terms. **h)** Residual of the velocity map and the reconstructed map. **i)** Simple rotation map constructed for position angle and ellipticity fixed to their global values. **j)** Residual of the velocity map and the simple rotation map. **k)** Position angle and flattening as a function of radius. **l)** k_3/k_1 and k_5/k_1 (from the analysis where position angle and ellipticity are fixed to their global values) as a function of radius.
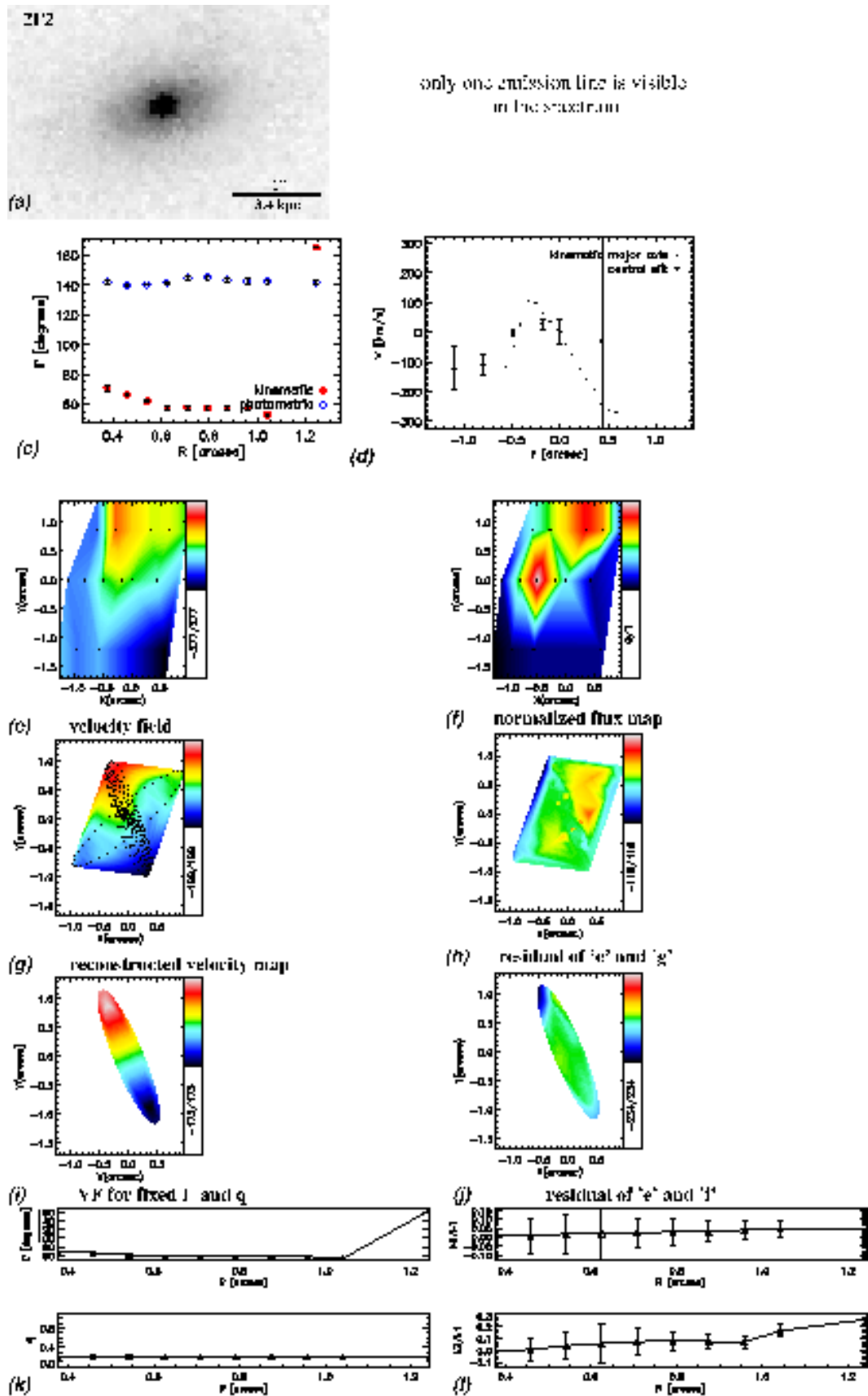
B.2. Field galaxies

Fig. B.19. a) HST-ACS image of the galaxy in the *V* band. **b)** Rotation curves of different emission lines extracted along the central slit. **c)** Position angles of kinematic and photometric axes as a function of radius. **d)** Rotation curves extracted along the central slit and the kinematic major axis. **e)** Hβ velocity field. **f)** Normalized Hβ flux map. **g)** Velocity map reconstructed using 6 harmonic terms. **h)** Residual of the velocity map and the reconstructed map. **i)** Simple rotation map constructed for position angle and ellipticity fixed to their global values. **j)** Residual of the velocity map and the simple rotation map. **k)** Position angle and flattening as a function of radius. **l)** k_3/k_1 and k_5/k_1 (from the analysis where position angle and ellipticity are fixed to their global values) as a function of radius.
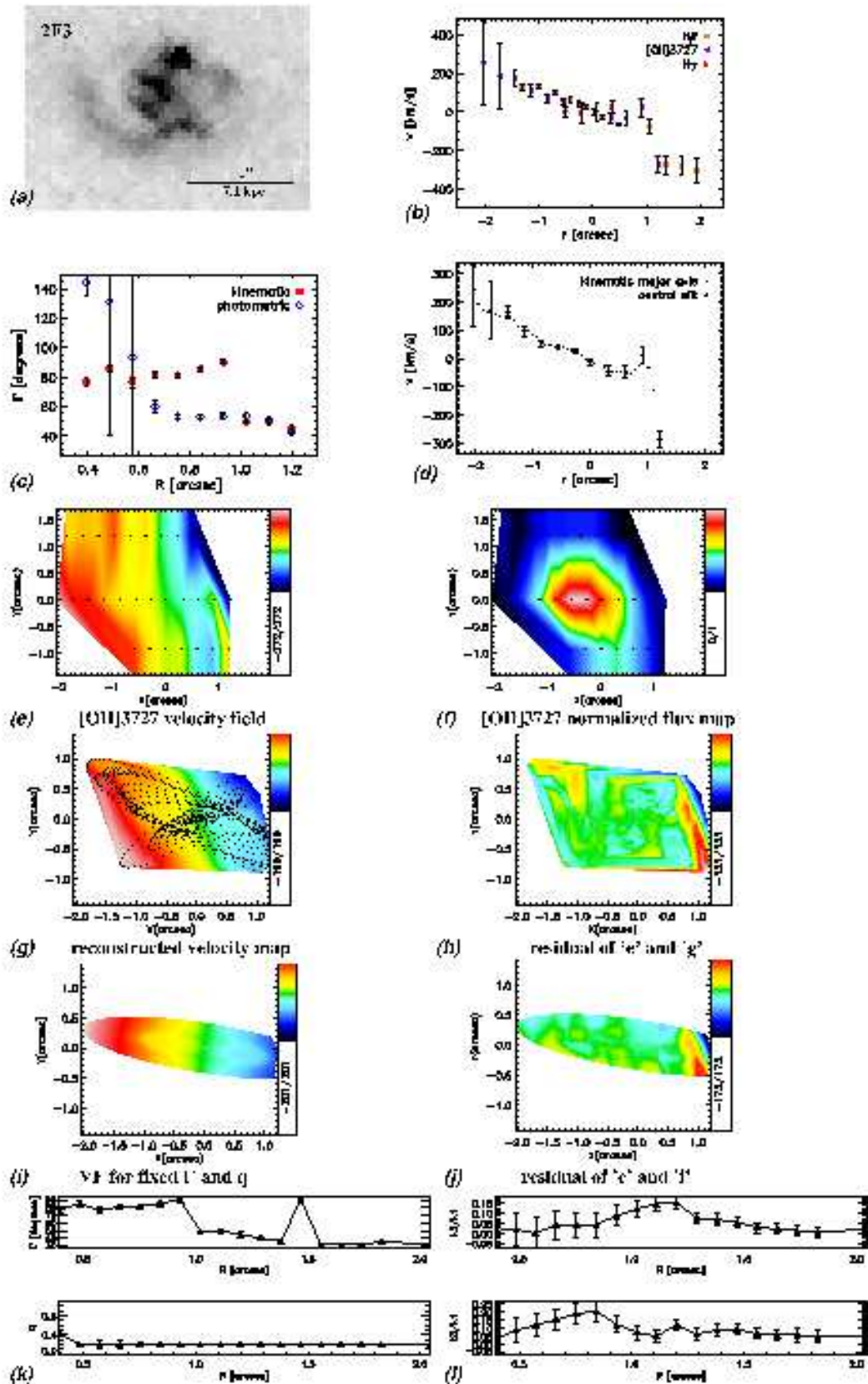
Fig. B.20. a) HST-ACS image of the galaxy in the *V* band. **c)** Position angles of kinematic and photometric axes as a function of radius. **d)** Rotation curves extracted along the central slit and the kinematic major axis. **e)** Velocity field constructed using the emission line which could not be identified. **f)** Normalized flux map of the emission line which could not be identified. **g)** Velocity map reconstructed using 6 harmonic terms. **h)** Residual of the velocity map and the reconstructed map. **i)** Simple rotation map constructed for position angle and ellipticity fixed to their global values. **j)** Residual of the velocity map and the simple rotation map. **k)** Position angle and flattening as a function of radius. **l)** k_3/k_1 and k_5/k_1 (from the analysis where position angle and ellipticity are fixed to their global values) as a function of radius.
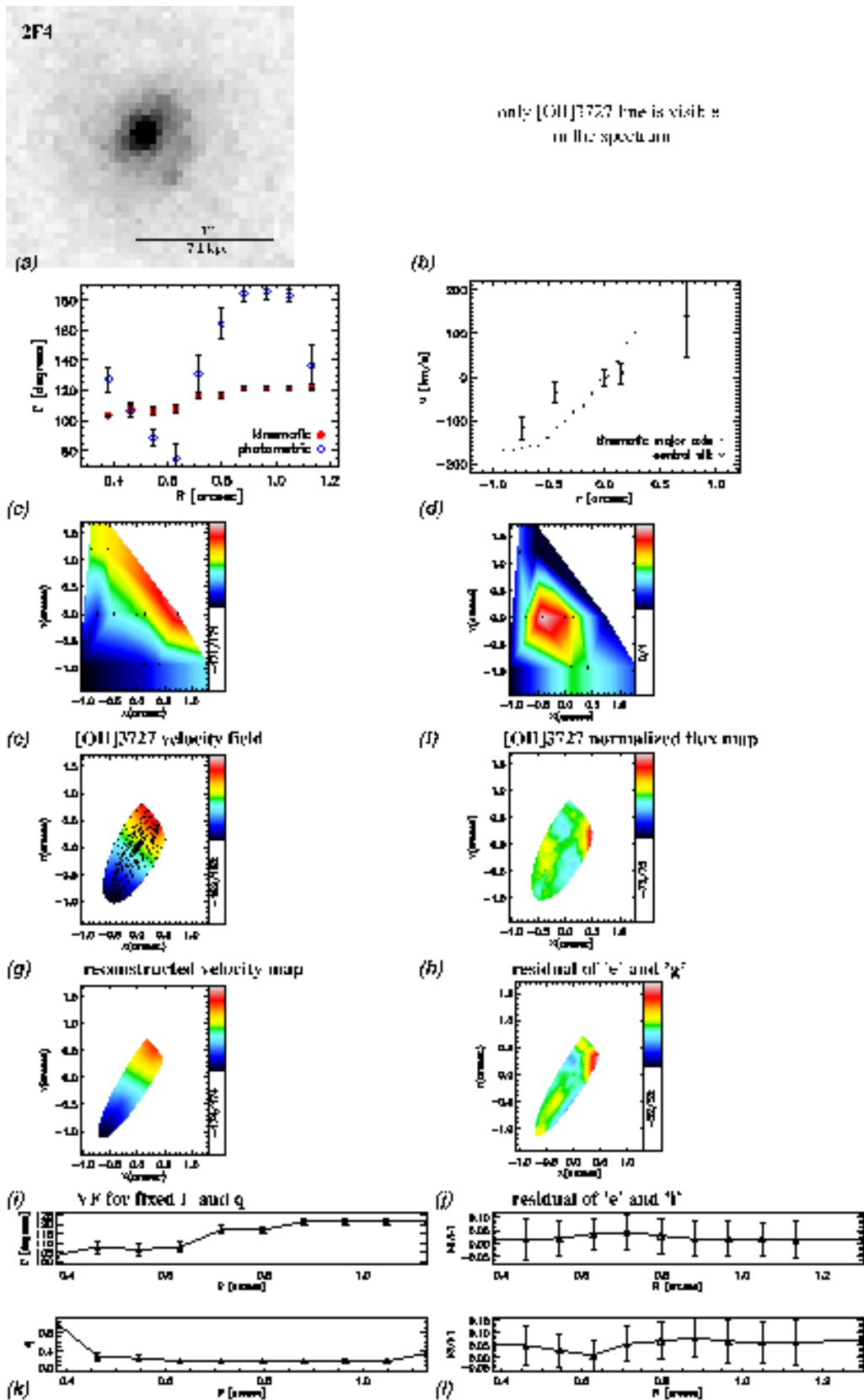
Fig. B.21. a) HST-ACS image of the galaxy in the *V* band. **b)** Rotation curves of different emission lines extracted along the central slit. **c)** Position angles of kinematic and photometric axes as a function of radius. **d)** Rotation curves extracted along the central slit and the kinematic major axis. **e)** [OII]3727 velocity field. **f)** Normalized [OII]3727 flux map. **g)** Velocity map reconstructed using 6 harmonic terms. **h)** Residual of the velocity map and the reconstructed map. **i)** Simple rotation map constructed for position angle and ellipticity fixed to their global values. **j)** Residual of the velocity map and the simple rotation map. **k)** Position angle and flattening as a function of radius. **l)** k_3/k_1 and k_5/k_1 (from the analysis where position angle and ellipticity are fixed to their global values) as a function of radius.
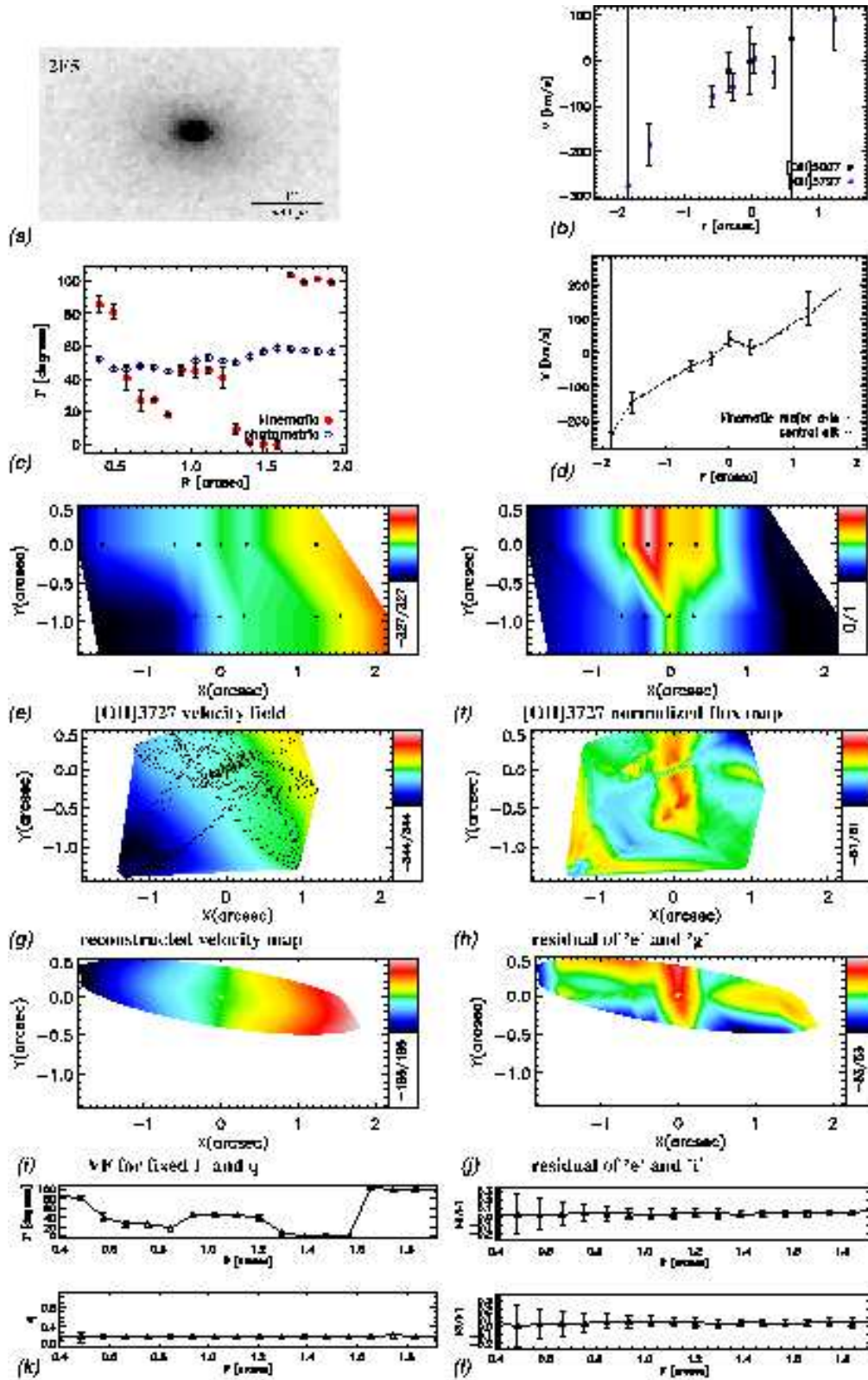
Fig. B.22. a) HST-ACS image of the galaxy in the *V* band. **b)** Rotation curves of different emission lines extracted along the central slit. **c)** Position angles of kinematic and photometric axes as a function of radius. **d)** Rotation curves extracted along the central slit and the kinematic major axis. **e)** [OII]3727 velocity field. **f)** Normalized [OII]3727 flux map. **g)** Velocity map reconstructed using 6 harmonic terms. **h)** Residual of the velocity map and the reconstructed map. **i)** Simple rotation map constructed for position angle and ellipticity fixed to their global values. **j)** Residual of the velocity map and the simple rotation map. **k)** Position angle and flattening as a function of radius. **l)** k_3/k_1 and k_5/k_1 (from the analysis where position angle and ellipticity are fixed to their global values) as a function of radius.
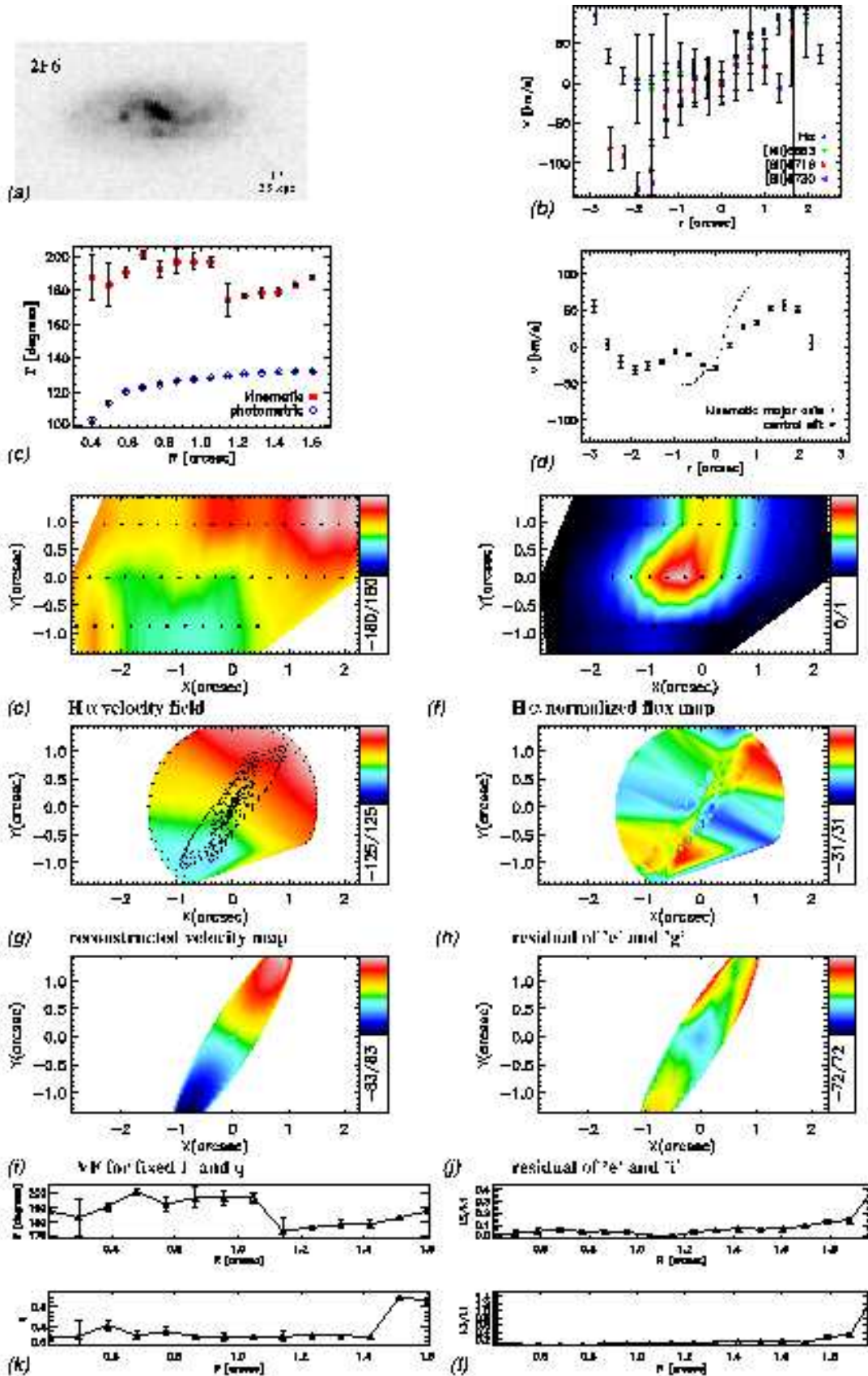
Fig. B.23. a) HST-ACS image of the galaxy in the *V* band. **b)** Rotation curves of different emission lines extracted along the central slit. **c)** Position angles of kinematic and photometric axes as a function of radius. **d)** Rotation curves extracted along the central slit and the kinematic major axis. **e)** [OII]3727 velocity field. **f)** Normalized [OII]3727 flux map. **g)** Velocity map reconstructed using 6 harmonic terms. **h)** Residual of the velocity map and the reconstructed map. **i)** Simple rotation map constructed for position angle and ellipticity fixed to their global values. **j)** Residual of the velocity map and the simple rotation map. **k)** Position angle and flattening as a function of radius. **l)** k_3/k_1 and k_5/k_1 (from the analysis where position angle and ellipticity are fixed to their global values) as a function of radius.

Fig. B.24. a) HST-ACS image of the galaxy in the *V* band. **b)** Rotation curves of different emission lines extracted along the central slit. **c)** Position angles of kinematic and photometric axes as a function of radius. **d)** Rotation curves extracted along the central slit and the kinematic major axis. **e)** Hα velocity field. **f)** Normalized Hα flux map. **g)** Velocity map reconstructed using 6 harmonic terms. **h)** Residual of the velocity map and the reconstructed map. **i)** Simple rotation map constructed for position angle and ellipticity fixed to their global values. **j)** Residual of the velocity map and the simple rotation map. **k)** Position angle and flattening as a function of radius. **l)** k_3/k_1 and k_5/k_1 (from the analysis where position angle and ellipticity are fixed to their global values) as a function of radius.
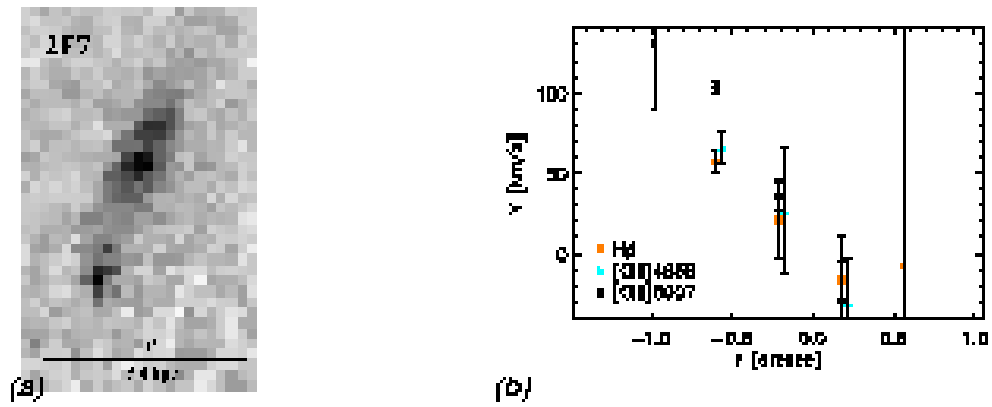
Fig. B.25. a) HST-ACS image of the galaxy in the *V* band. **b)** Rotation curves of different emission lines extracted along the central slit.
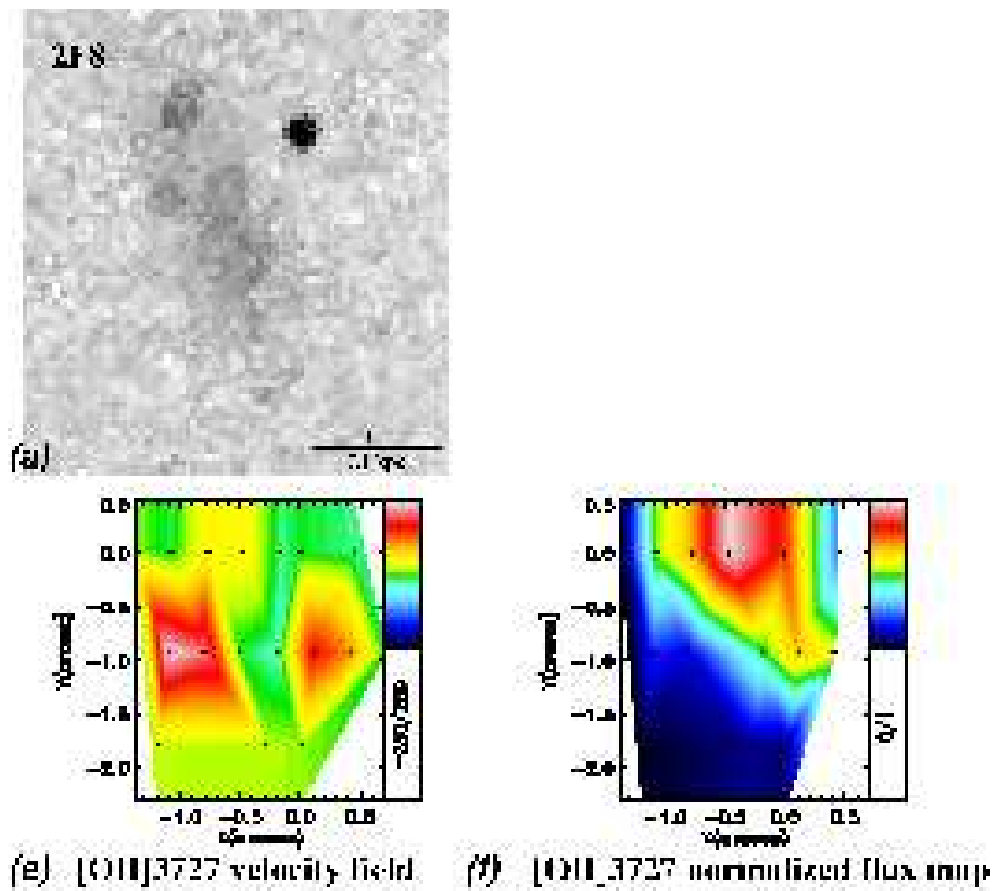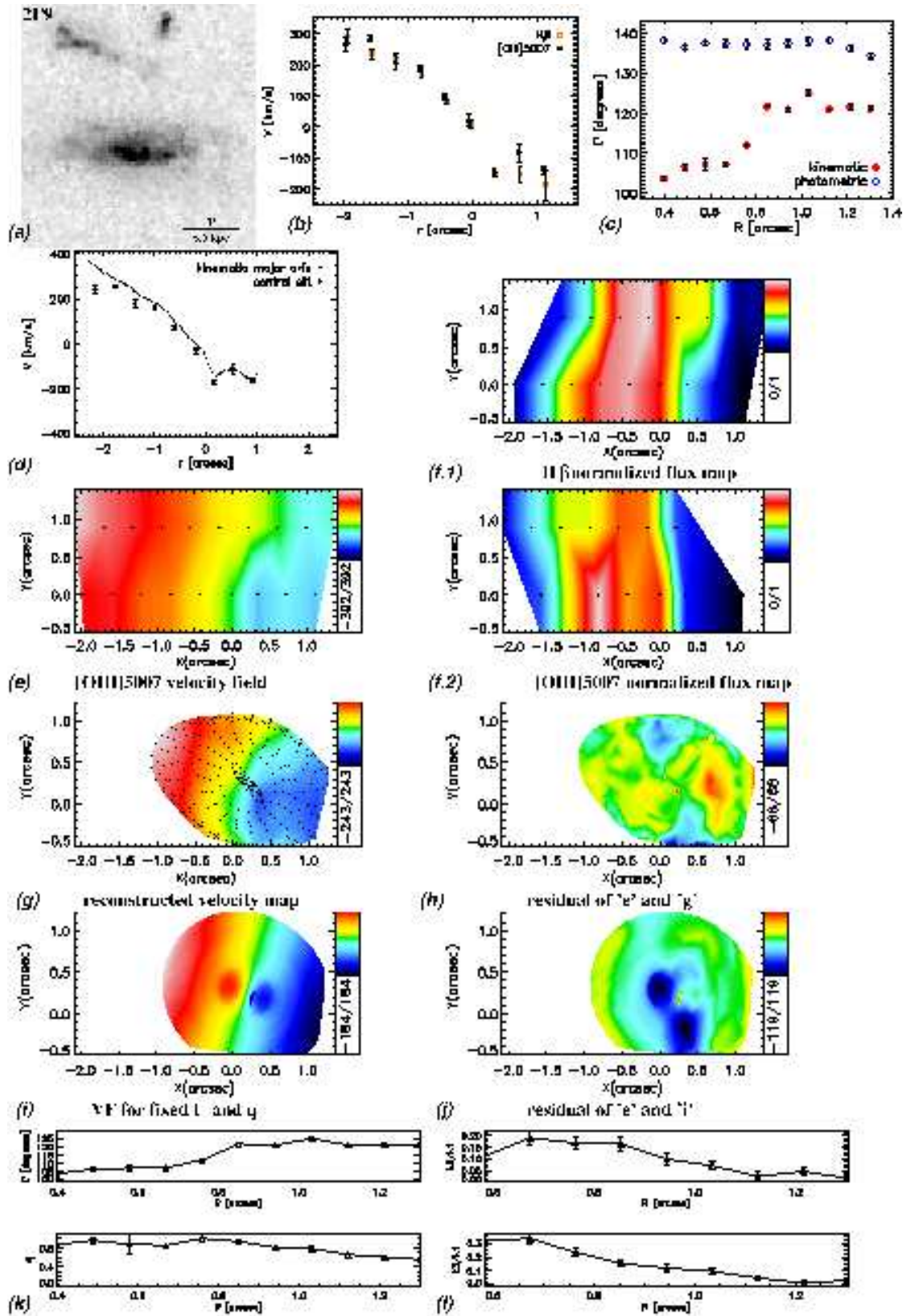

Fig. B.26. a) HST-ACS image of the galaxy in the *V* band. **e)** [OII]3727 velocity field. **f)** Normalized [OII]3727 flux map.

Fig. B.27. a) HST-ACS image of the galaxy in the *V* band. **b)** Rotation curves of different emission lines extracted along the central slit. **c)** Position angles of kinematic and photometric axes as a function of radius. **d)** Rotation curves extracted along the central slit and the kinematic major axis. **e)** [OIII]5007 velocity field. **f.1)** Normalized Hβ flux map. **f.2)** Normalized [OIII]5007 flux map. **g)** Velocity map reconstructed using 6 harmonic terms. **h)** Residual of the velocity map and the reconstructed map. **i)** Simple rotation map constructed for position angle and ellipticity fixed to their global values. **j)** Residual of the velocity map and the simple rotation map. **k)** Position angle and flattening as a function of radius. **l)** k_3/k_1 and k_5/k_1 (from the analysis where position angle and ellipticity are fixed to their global values) as a function of radius.
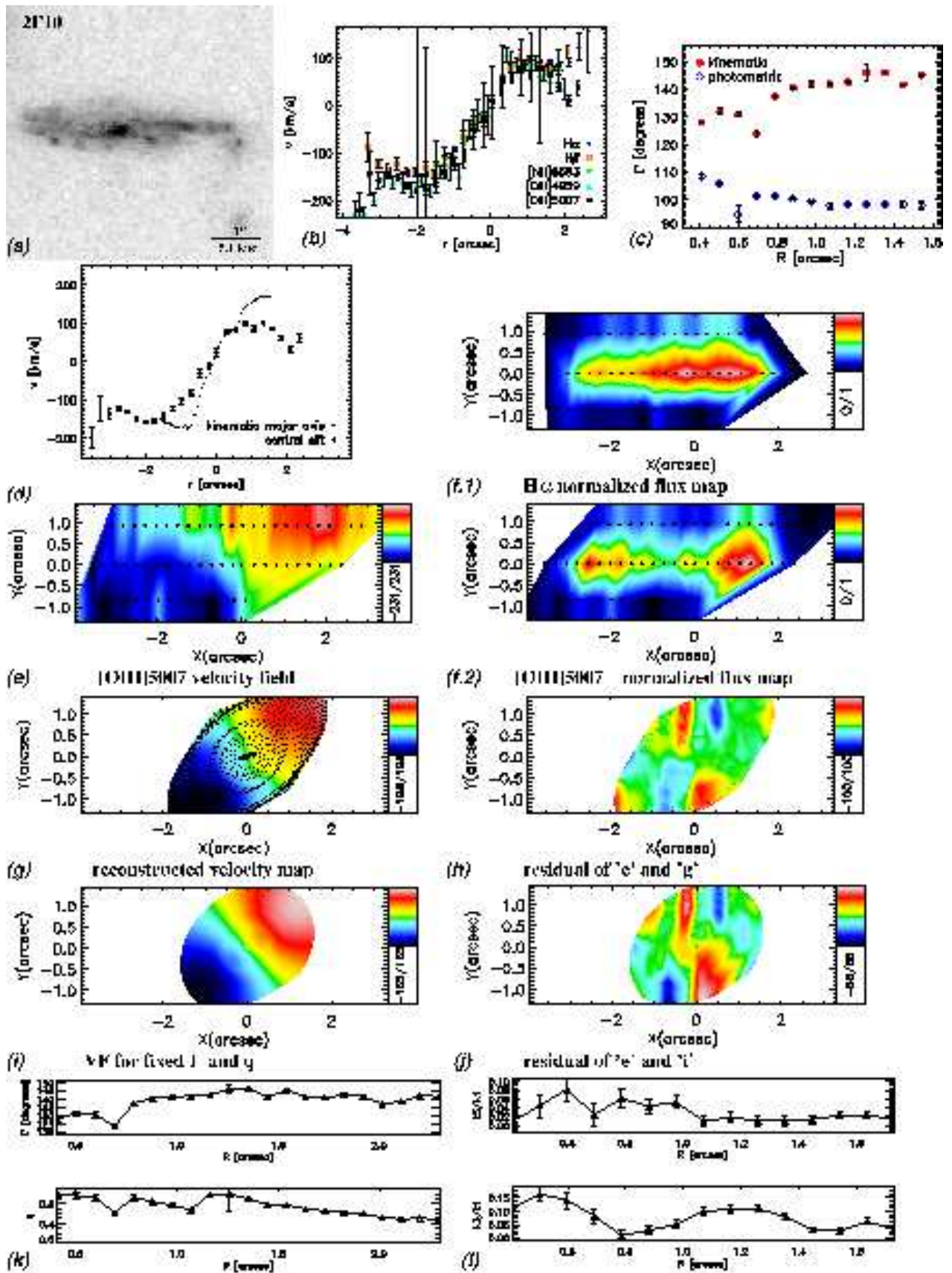
Fig. B.28. a) HST-ACS image of the galaxy in the *V* band. **b)** Rotation curves of different emission lines extracted along the central slit. **c)** Position angles of kinematic and photometric axes as a function of radius. **d)** Rotation curves extracted along the central slit and the kinematic major axis. **e)** [OIII]5007 velocity field. **f.1)** Normalized Hα flux map. **f.2)** Normalized [OIII]5007 flux map. **g)** Velocity map reconstructed using 6 harmonic terms. **h)** Residual of the velocity map and the reconstructed map. **i)** Simple rotation map constructed for position angle and ellipticity fixed to their global values. **j)** Residual of the velocity map and the simple rotation map. **k)** Position angle and flattening as a function of radius. **l)** k_3/k_1 and k_5/k_1 (from the analysis where position angle and ellipticity are fixed to their global values) as a function of radius.
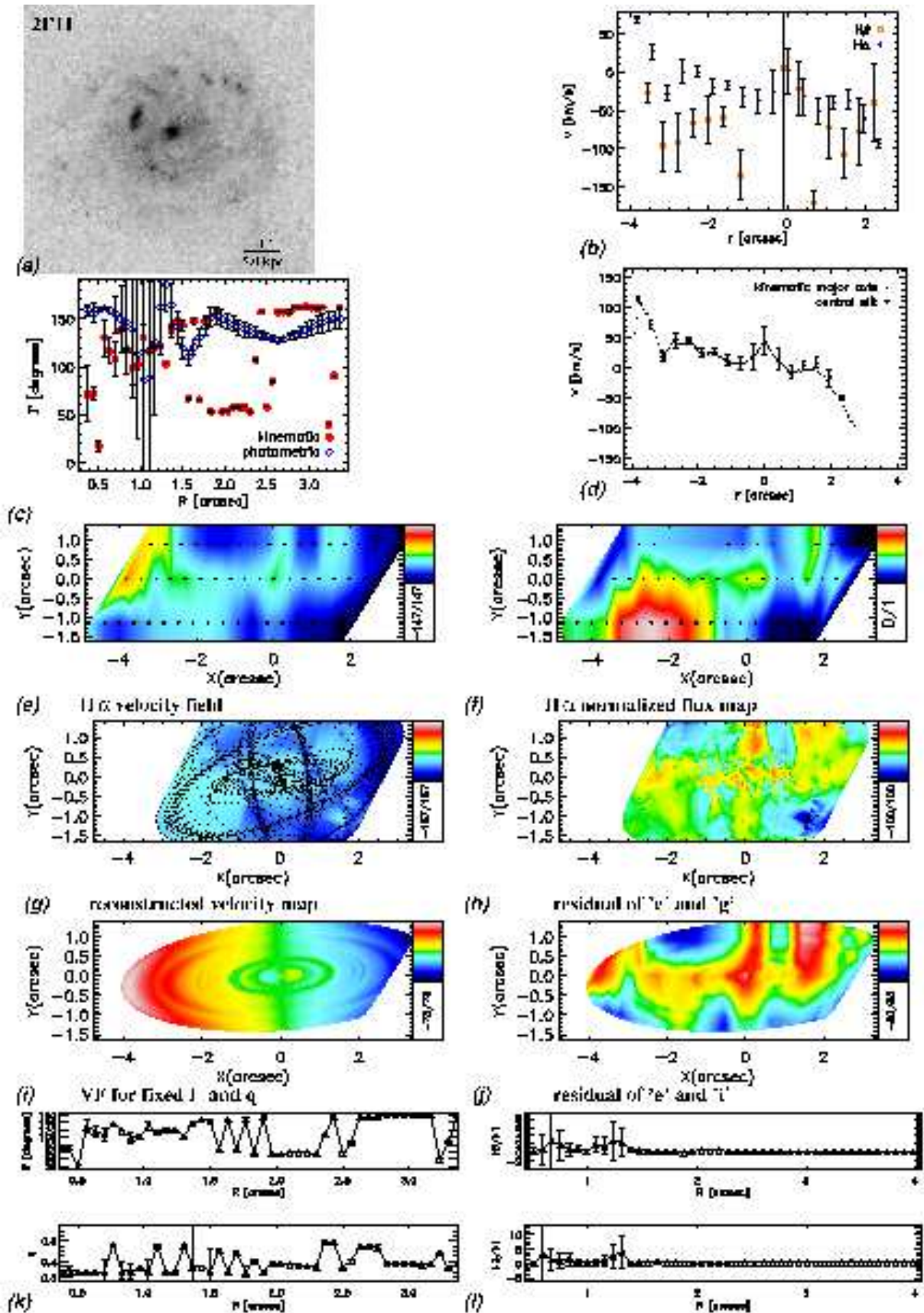
Fig. B.29. a) HST-ACS image of the galaxy in the *V* band. **b)** Rotation curves of different emission lines extracted along the central slit. **c)** Position angles of kinematic and photometric axes as a function of radius. **d)** Rotation curves extracted along the central slit and the kinematic major axis. **e)** Hα velocity field. **f)** Normalized Hα flux map. **g)** Velocity map reconstructed using 6 harmonic terms. **h)** Residual of the velocity map and the reconstructed map. **i)** Simple rotation map constructed for position angle and ellipticity fixed to their global values. **j)** Residual of the velocity map and the simple rotation map. **k)** Position angle and flattening as a function of radius. **l)** k_3/k_1 and k_5/k_1 (from the analysis where position angle and ellipticity are fixed to their global values) as a function of radius.
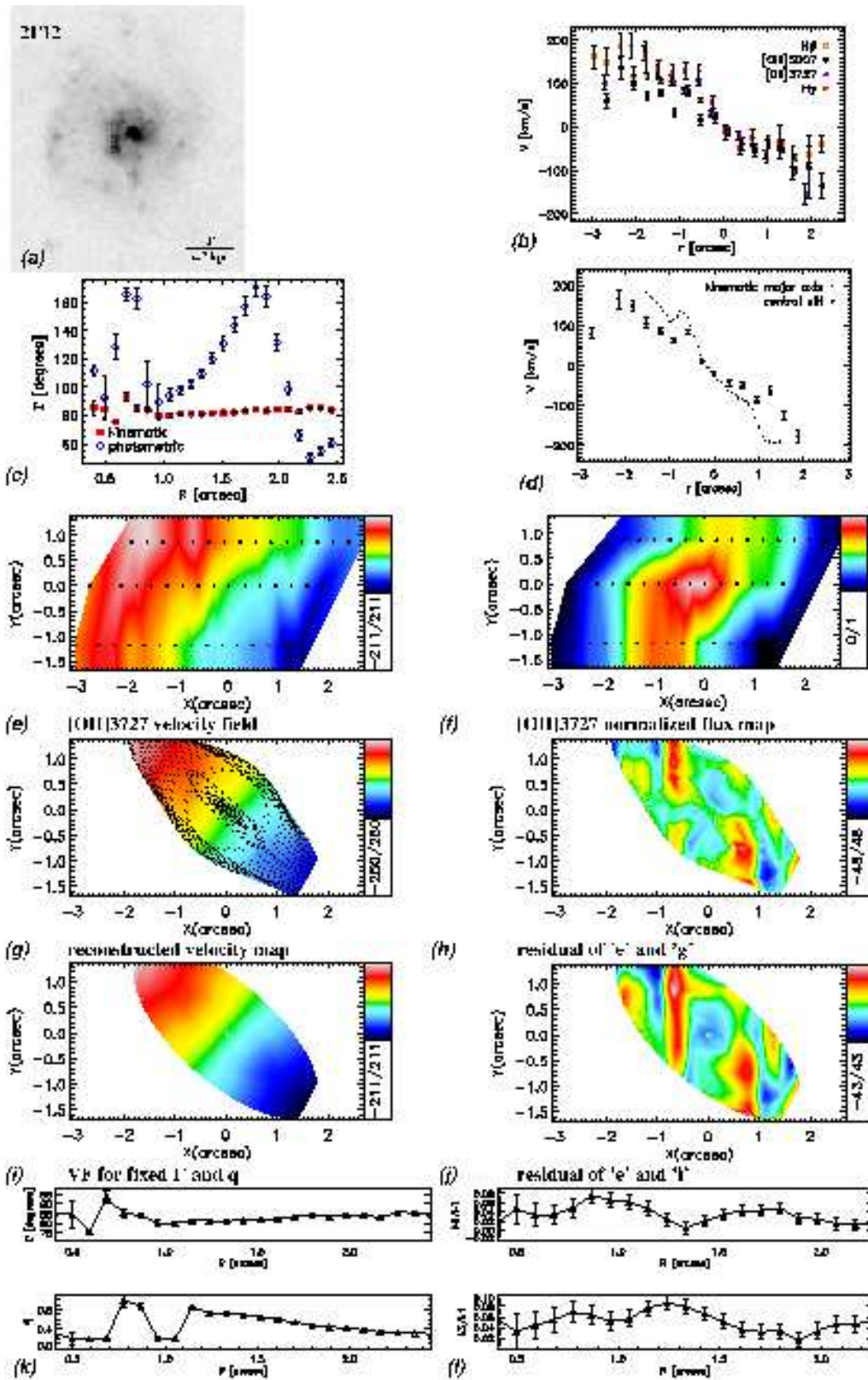
Fig. B.30. a) HST-ACS image of the galaxy in the *V* band. **b)** Rotation curves of different emission lines extracted along the central slit. **c)** Position angles of kinematic and photometric axes as a function of radius. **d)** Rotation curves extracted along the central slit and the kinematic major axis. **e)** [OII]3727 velocity field. **f)** Normalized [OII]3727 flux map. **g)** Velocity map reconstructed using 6 harmonic terms. **h)** Residual of the velocity map and the reconstructed map. **i)** Simple rotation map constructed for position angle and ellipticity fixed to their global values. **j)** Residual of the velocity map and the simple rotation map. **k)** Position angle and flattening as a function of radius. **l)** k_3/k_1 and k_5/k_1 (from the analysis where position angle and ellipticity are fixed to their global values) as a function of radius.

Fig. B.31. a) HST-ACS image of the galaxy in the *V* band. **e)** [OII]3727 velocity field. **f)** Normalized [OII]3727 flux map.
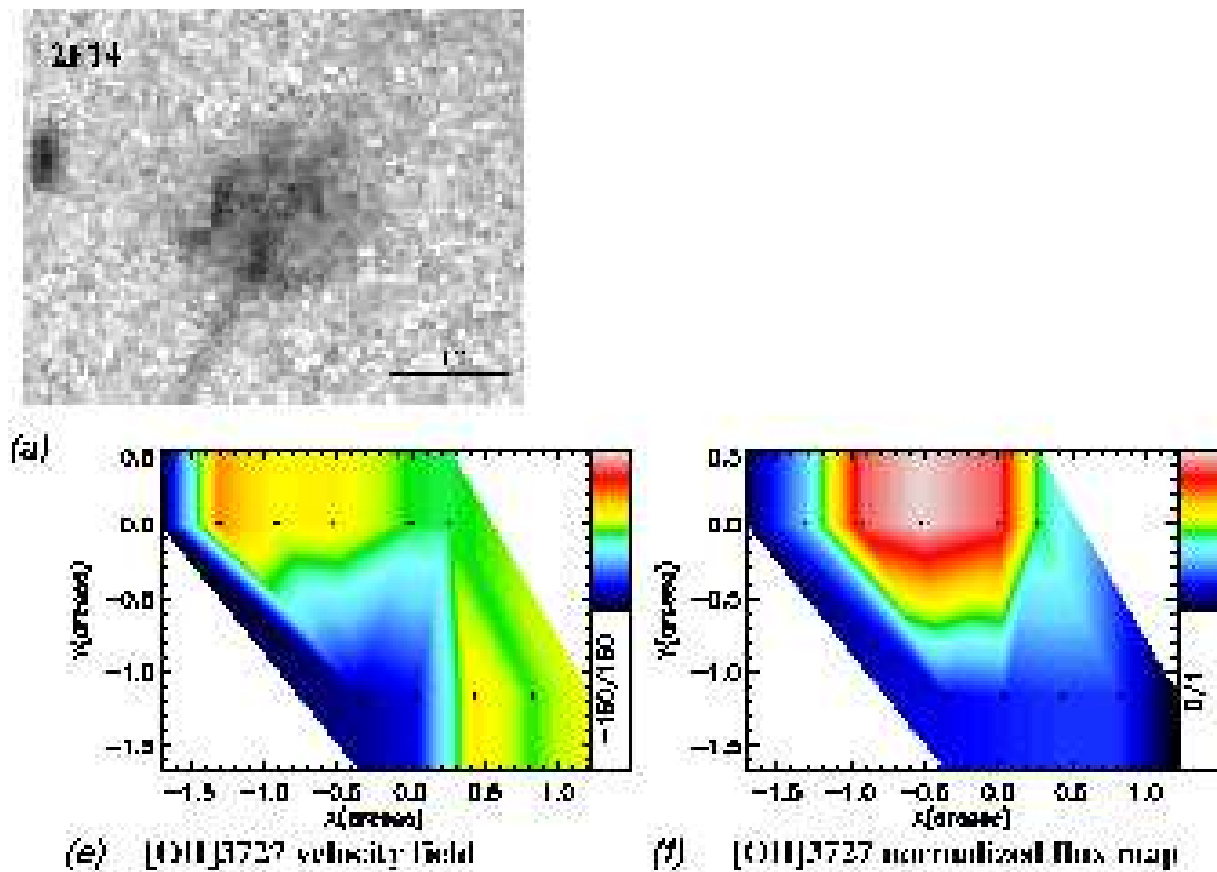
Fig. B.32. a) HST-ACS image of the galaxy in the *V* band. **e)** [OII]3727 velocity field. **f)** Normalized [OII]3727 flux map.
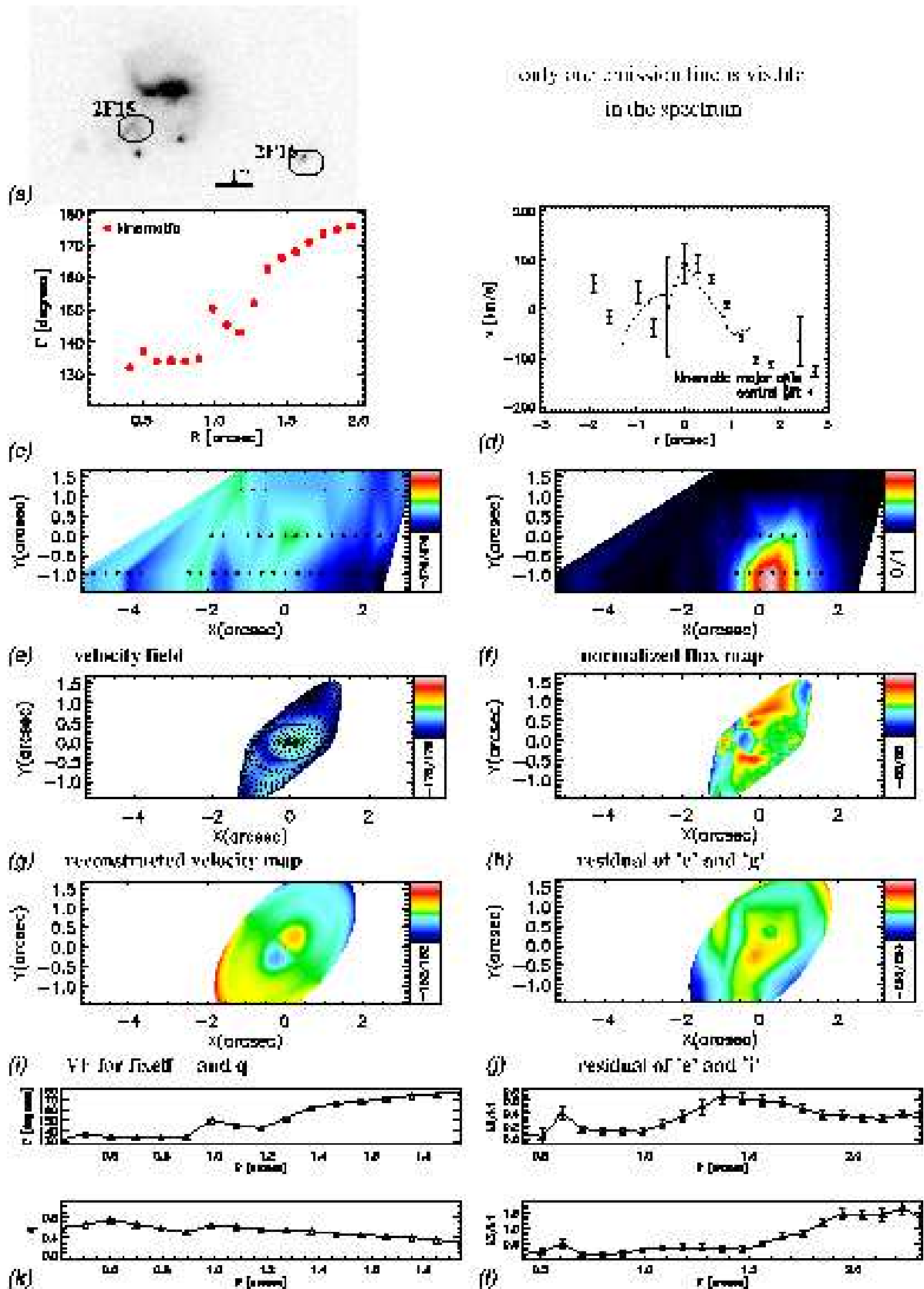
Fig. B.33. a) HST-ACS image of the objects in the *V* band. **c)** Position angle of the kinematic axis as a function of radius. **d)** Rotation curves extracted along the central slit and the kinematic major axis. **e)** Velocity field of the emission line which could not be identified. The map belongs to 2F15 and 2F16 together. **f)** Normalized flux map of the emission line which could not be identified. The map belongs to 2F15 and 2F16 together. **g)** Velocity map reconstructed using 6 harmonic terms. **h)** Residual of the velocity map and the reconstructed map. **i)** Simple rotation map constructed for position angle and ellipticity fixed to their global values. **j)** Residual of the velocity map and the simple rotation map. **k)** Position angle and flattening as a function of radius. **l)** k_3/k_1 and k_5/k_1 (from the analysis where position angle and ellipticity are fixed to their global values) as a function of radius.
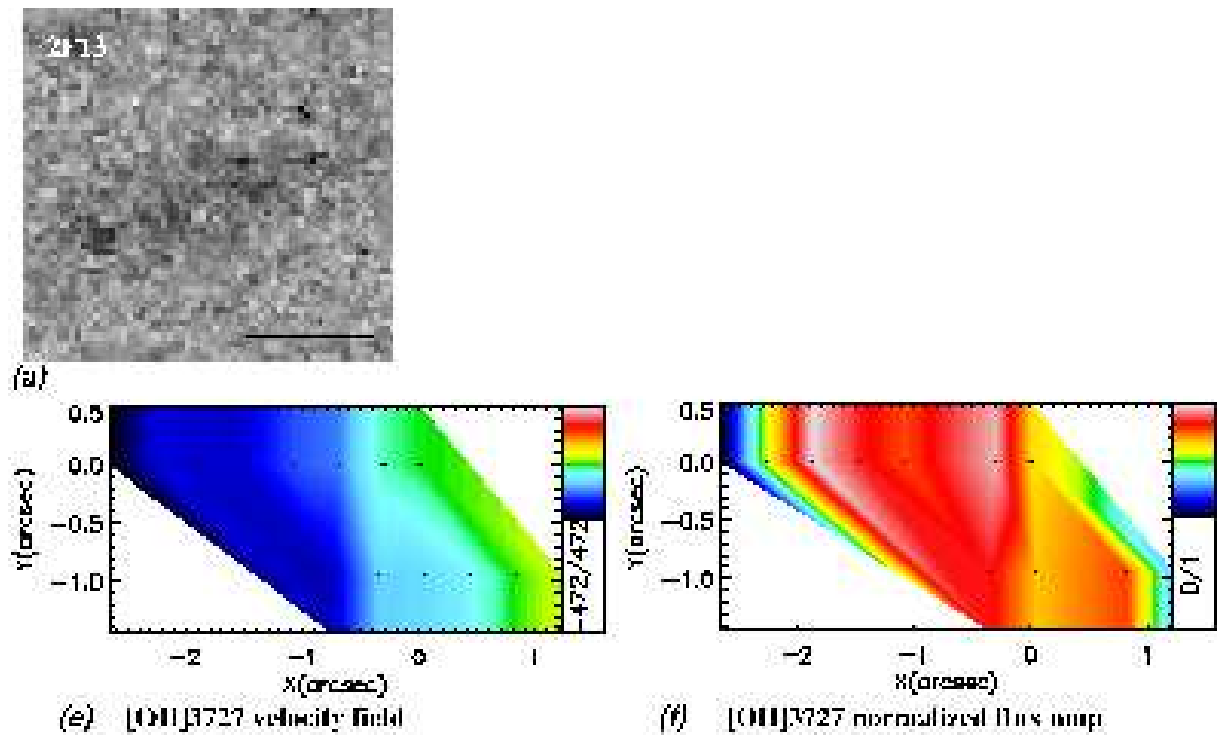
(a)

(b)

(e) [OIII]5007 velocity field

(f) [OIII]5007 normalized flux map

Fig. B.34. a.1) HST-ACS image of the galaxy in the *V* band. **a.2)** Image showing the galaxy together with its companion. **b)** Rotation curves of different emission lines extracted along the central slit. **e)** [OIII]5007 velocity field. **f)** Normalized [OIII]5007 flux map.

(a)

(e) [OII]3727 velocity field

(f) [OII]3727 normalized flux map

Fig. B.35. a) HST-ACS image of the galaxy in the *V* band. **e)** [OII]3727 velocity field. **f)** Normalized [OII]3727 flux map.

Fig. B.36. a) HST-ACS image of the galaxy in the *V* band. **b)** Rotation curves of different emission lines extracted along the central slit. **c)** Position angles of kinematic and photometric axes as a function of radius. **d)** Rotation curves extracted along the central slit and the kinematic major axis. **e)** [OIII]5007 velocity field. **f)** Normalized [OIII]5007 flux map. **g)** Velocity map reconstructed using 6 harmonic terms. **h)** Residual of the velocity map and the reconstructed map. **i)** Simple rotation map constructed for position angle and ellipticity fixed to their global values. **j)** Residual of the velocity map and the simple rotation map. **k)** Position angle and flattening as a function of radius. **l)** k_3/k_1 and k_5/k_1 (from the analysis where position angle and ellipticity are fixed to their global values) as a function of radius.
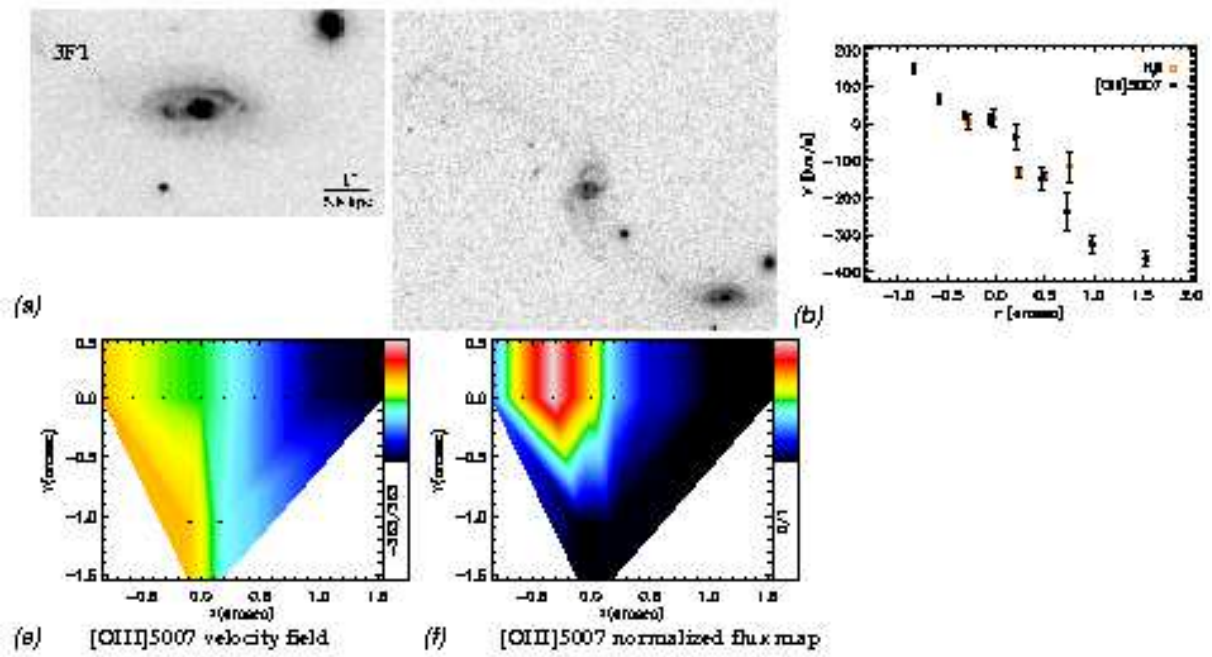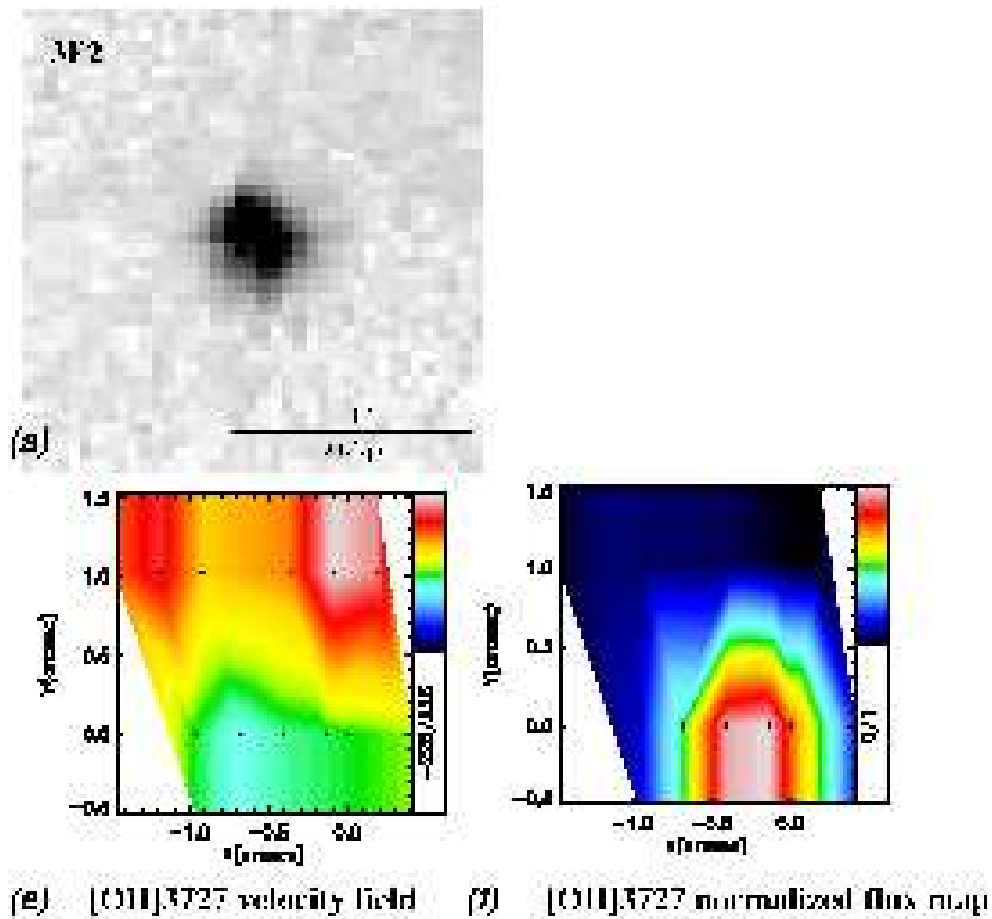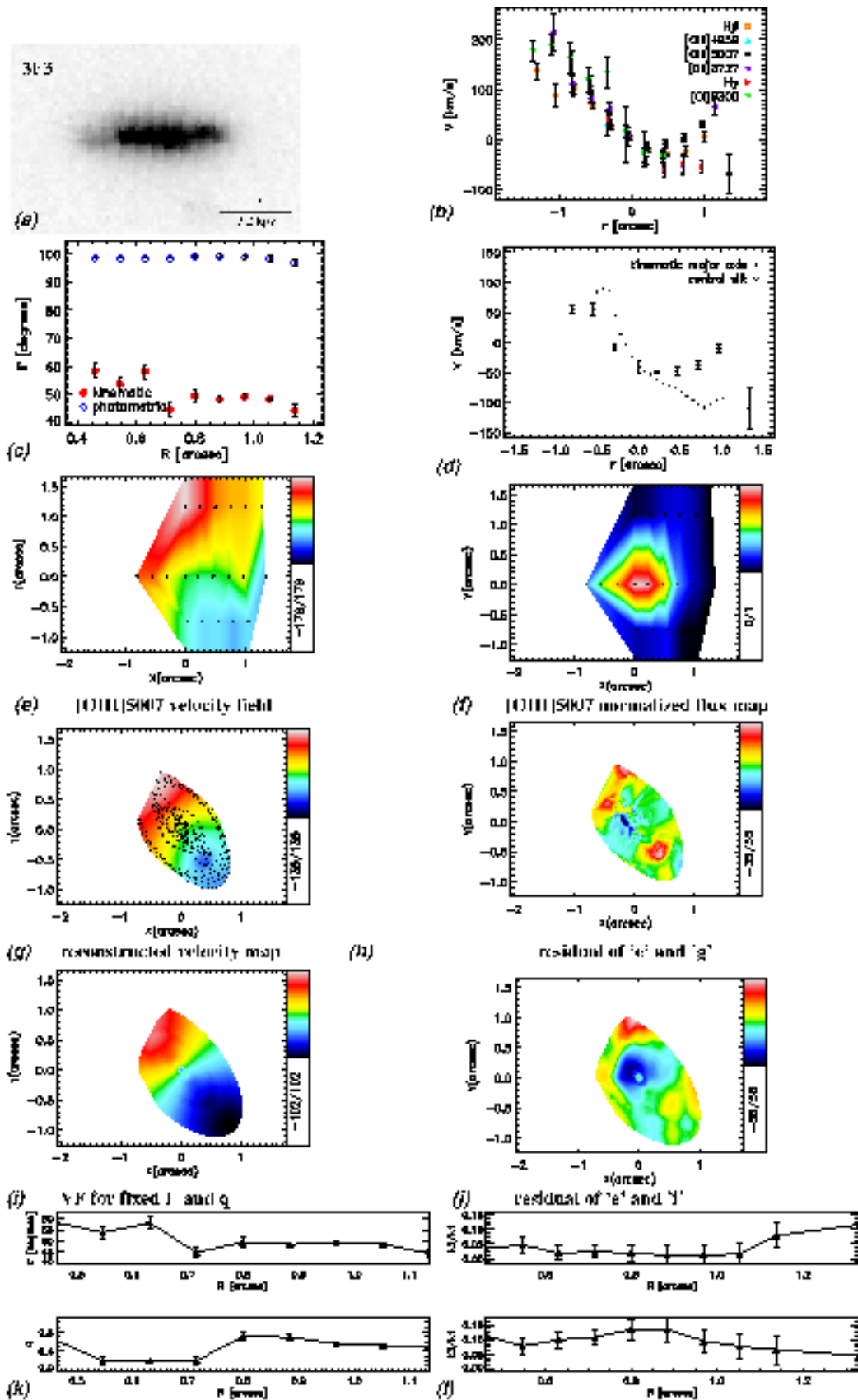
Fig. B.37. a) HST-ACS image of the galaxy in the *V* band. **b)** Rotation curves of different emission lines extracted along the central slit. **e)** [OII]3727 velocity field. **f)** Normalized [OII]3727 flux map.

Fig. B.38. a) HST-ACS image of the galaxy in the *V* band. **b)** Rotation curves of different emission lines extracted along the central slit.

Fig. B.39. a) HST-ACS image of the galaxy in the *V* band. **b)** Rotation curves of different emission lines extracted along the central slit. **c)** Position angles of kinematic and photometric axes as a function of radius. **d)** Rotation curves extracted along the central slit and the kinematic major axis. **e)** Hα velocity field. **f)** Normalized Hα flux map. **g)** Velocity map reconstructed using 6 harmonic terms. **h)** Residual of the velocity map and the reconstructed map. **i)** Simple rotation map constructed for position angle and ellipticity fixed to their global values. **j)** Residual of the velocity map and the simple rotation map. **k)** Position angle and flattening as a function of radius. **l)** k_3/k_1 and k_5/k_1 (from the analysis where position angle and ellipticity are fixed to their global values) as a function of radius.
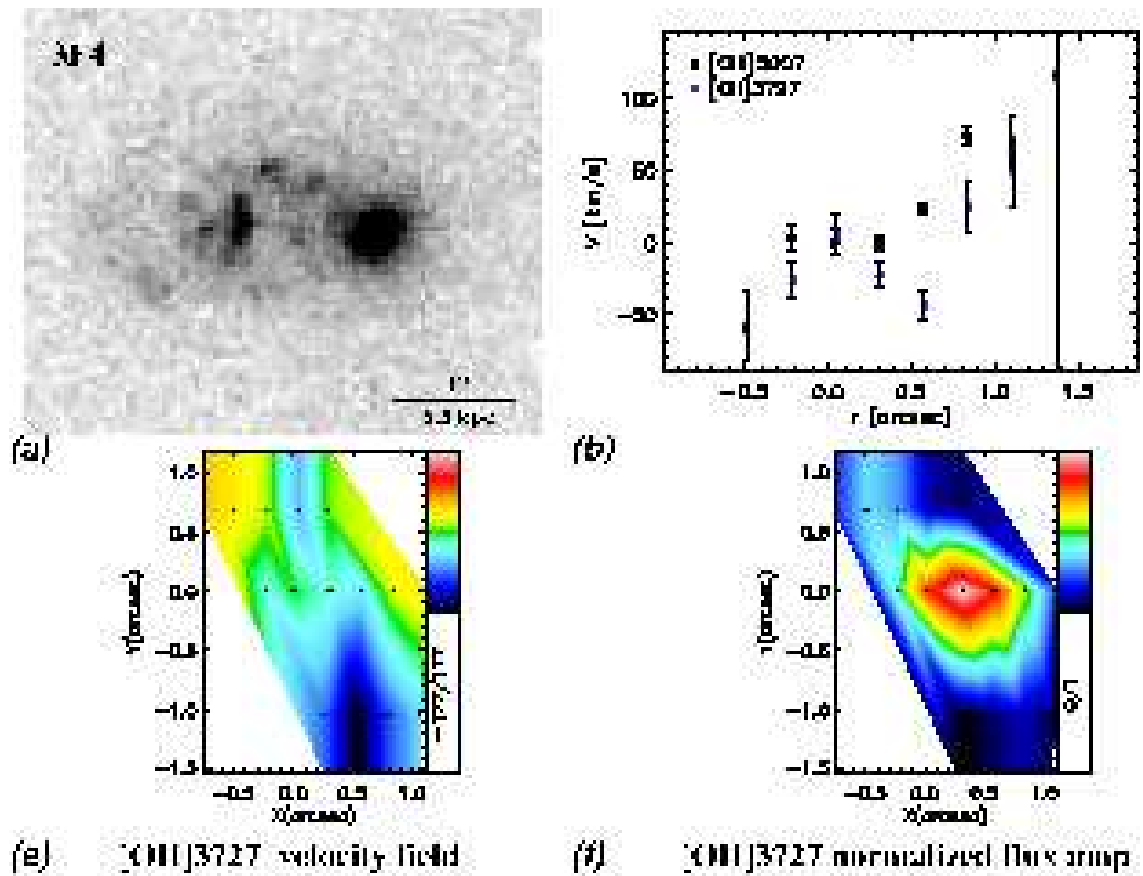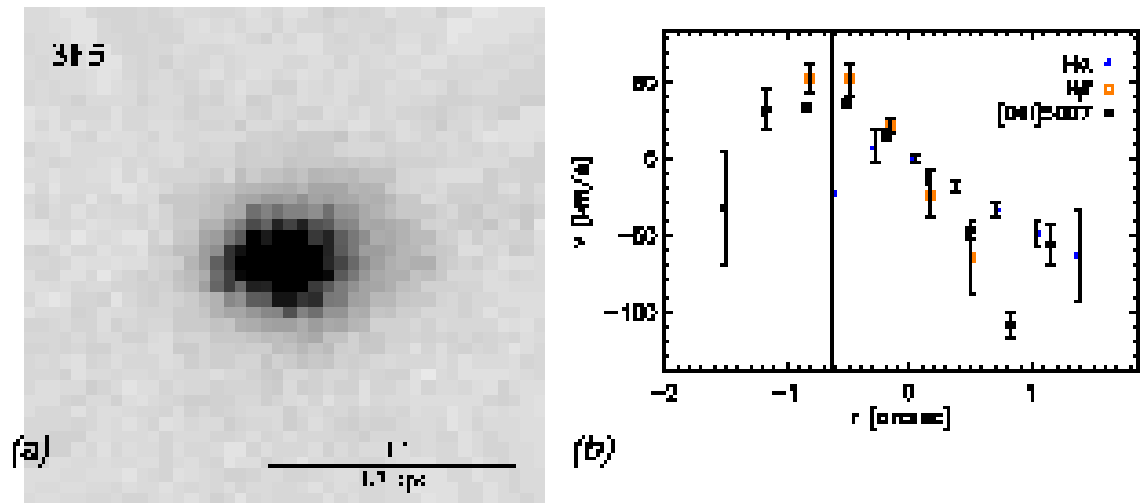
Fig. B.40. a) HST-ACS image of the galaxy in the *V* band. **b)** Rotation curves of different emission lines extracted along the central slit. **c)** Position angles of kinematic and photometric axes as a function of radius. **d)** Rotation curves extracted along the central slit and the kinematic major axis. **e)** Hα velocity field. **f)** Normalized Hα flux map. **g)** Velocity map reconstructed using 6 harmonic terms. **h)** Residual of the velocity map and the reconstructed map. **i)** Simple rotation map constructed for position angle and ellipticity fixed to their global values. **j)** Residual of the velocity map and the simple rotation map. **k)** Position angle and flattening as a function of radius. **l)** k_3/k_1 and k_5/k_1 (from the analysis where position angle and ellipticity are fixed to their global values) as a function of radius.
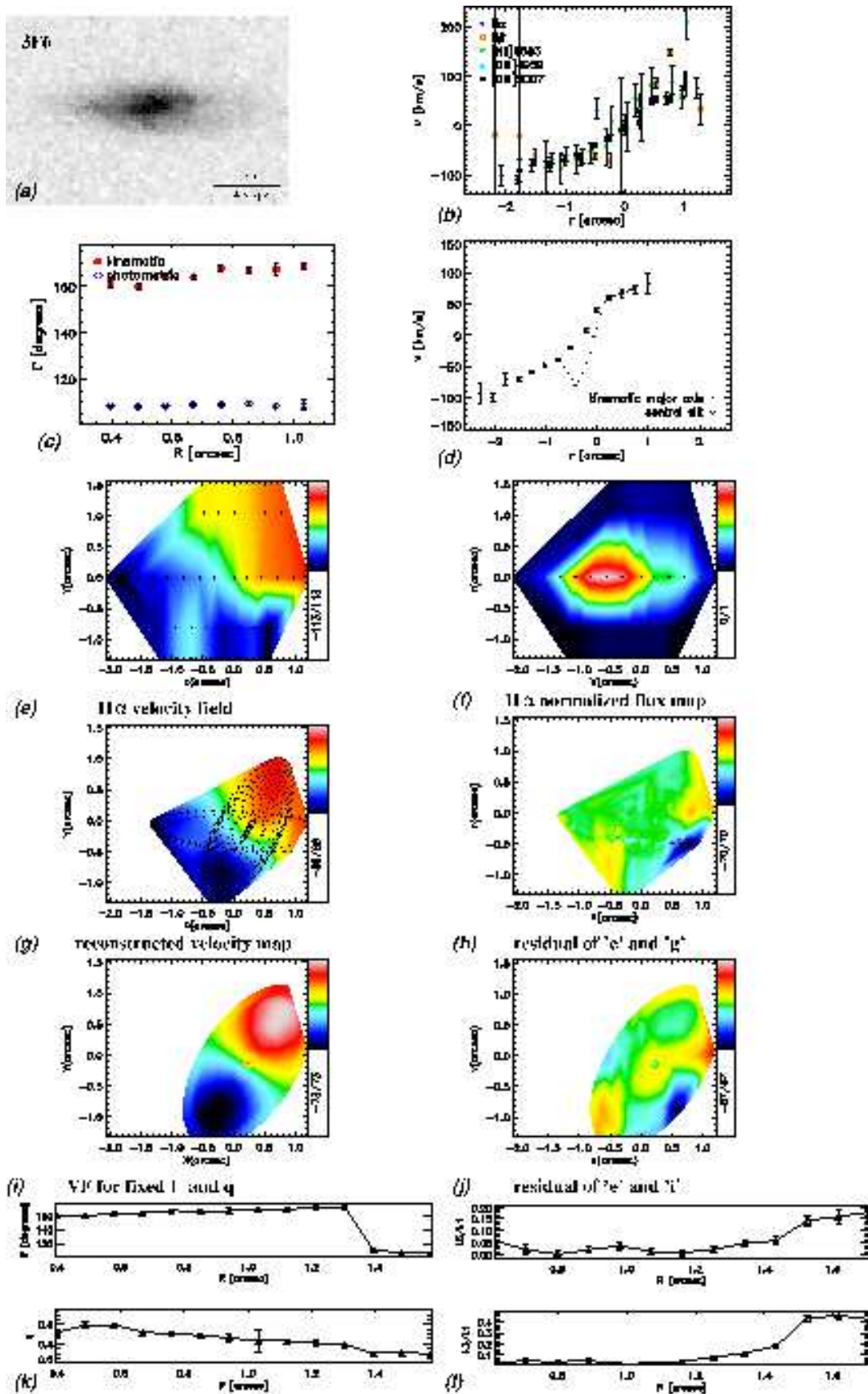
Fig. B.41. a) HST-ACS image of the galaxy in the *V* band. **b**) Rotation curves of different emission lines extracted along the central slit. **c**) Position angles of kinematic and photometric axes as a function of radius. **d**) Rotation curves extracted along the central slit and the kinematic major axis. **e**) [OII]3727 velocity field. **f.1**) Normalized Hβ flux map. **f.2**) Normalized [OII]3727 flux map. **g**) Velocity map reconstructed using 6 harmonic terms. **h**) Residual of the velocity map and the reconstructed map. **i**) Simple rotation map constructed for position angle and ellipticity fixed to their global values. **j**) Residual of the velocity map and the simple rotation map. **k**) Position angle and flattening as a function of radius. **l**) k_3/k_1 and k_5/k_1 (from the analysis where position angle and ellipticity are fixed to their global values) as a function of radius.
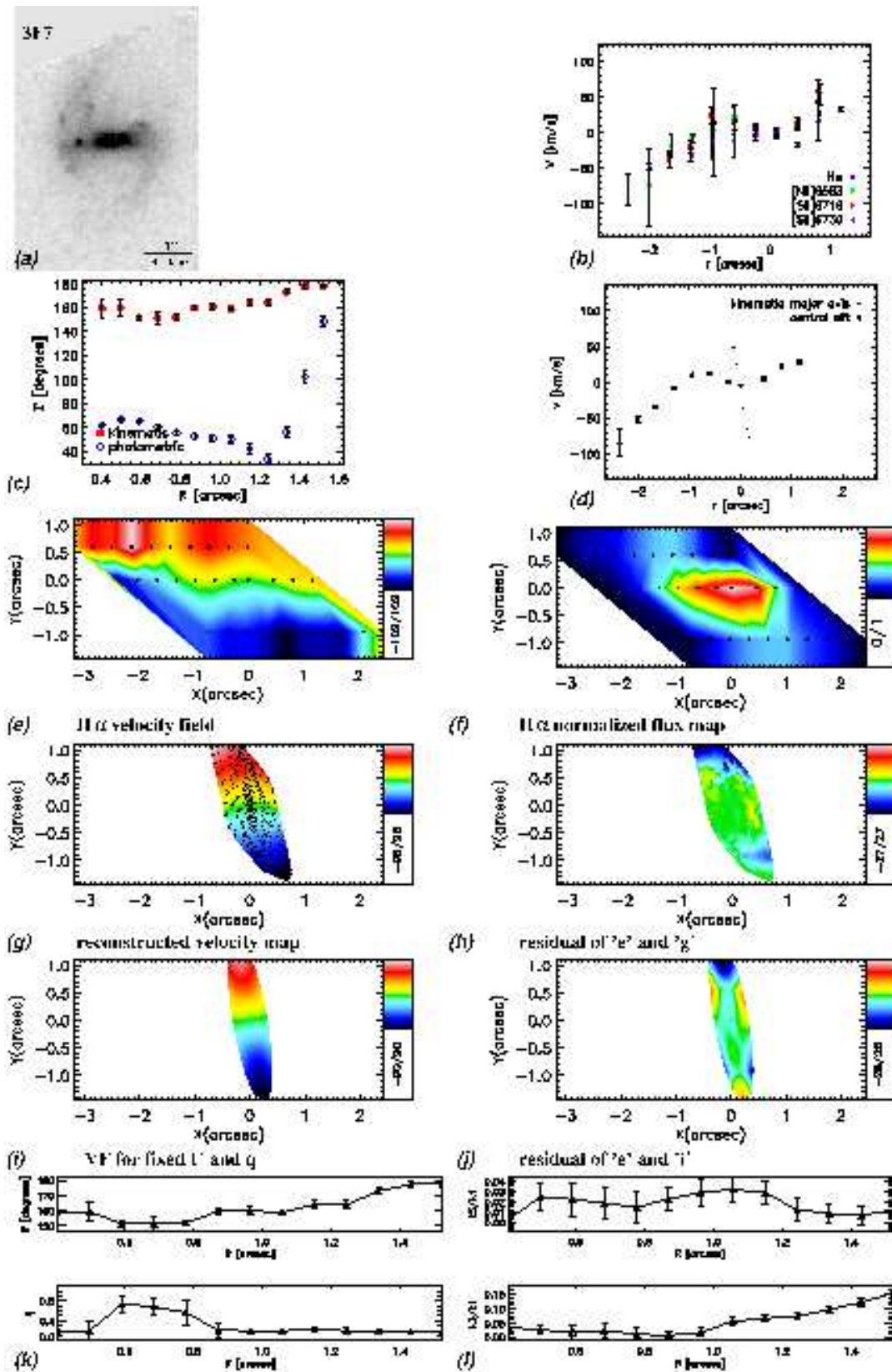
Fig. B.42. a) HST-ACS image of the galaxy in the *V* band. **b)** Rotation curves of different emission lines extracted along the central slit. **c)** Position angles of kinematic and photometric axes as a function of radius. **d)** Rotation curves extracted along the central slit and the kinematic major axis. **e)** Hα velocity field. **f)** Normalized Hα flux map. **g)** Velocity map reconstructed using 6 harmonic terms. **h)** Residual of the velocity map and the reconstructed map. **i)** Simple rotation map constructed for position angle and ellipticity fixed to their global values. **j)** Residual of the velocity map and the simple rotation map. **k)** Position angle and flattening as a function of radius. **l)** k_3/k_1 and k_5/k_1 (from the analysis where position angle and ellipticity are fixed to their global values) as a function of radius.
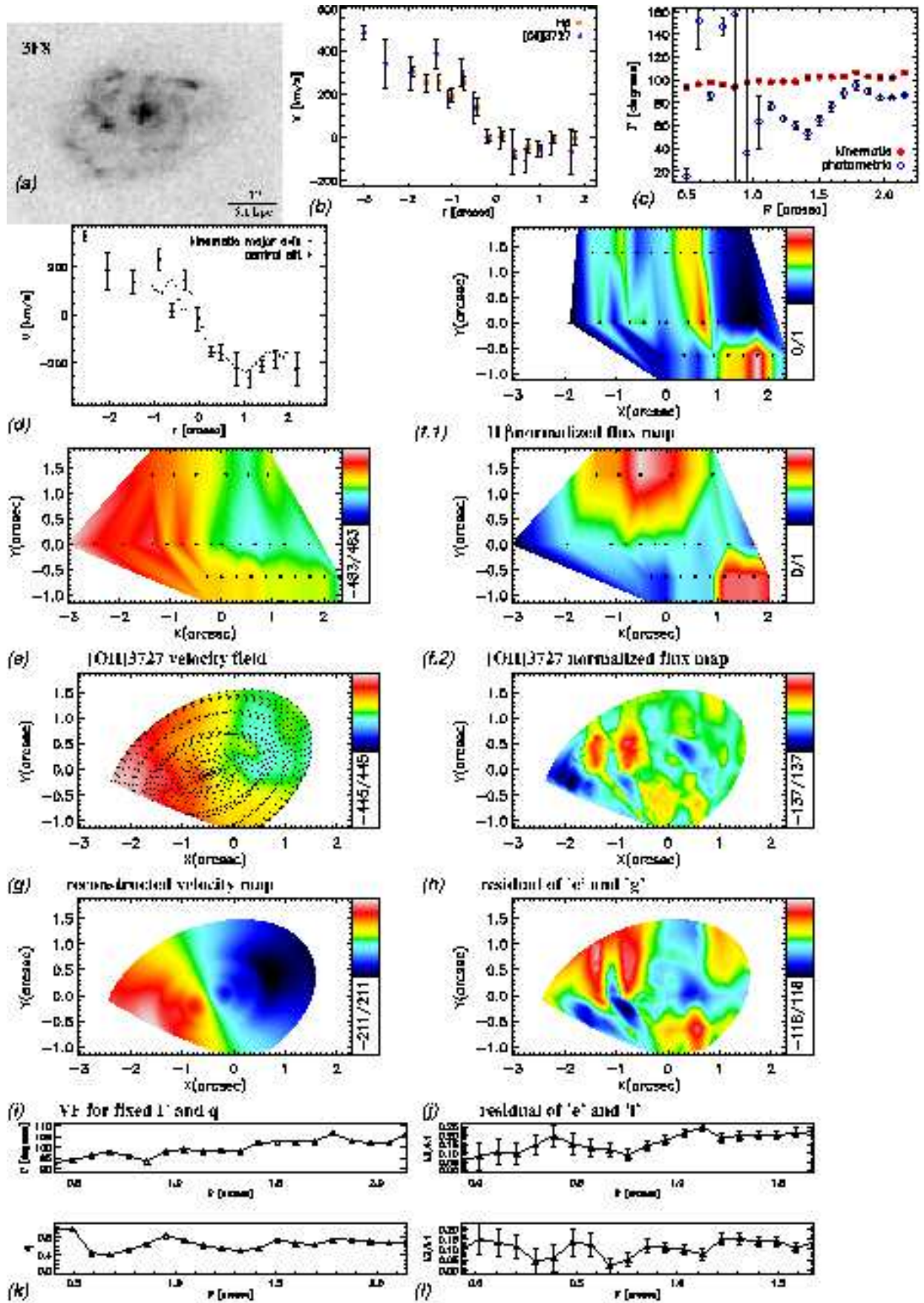
Fig. B.43. a) HST-ACS image of the galaxy in the *V* band. **b)** Rotation curves of different emission lines extracted along the central slit.

Fig. B.44. a) HST-ACS image of the galaxy in the *V* band. **b)** Rotation curves of different emission lines extracted along the central slit.

Fig. B.45. a) HST-ACS image of the galaxy in the *V* band. **b)** Rotation curves of different emission lines extracted along the central slit. **c)** Position angles of kinematic and photometric axes as a function of radius. **d)** Rotation curves extracted along the central slit and the kinematic major axis. **e)** [OII]3727 velocity field. **f)** Normalized [OII]3727 flux map. **g)** Velocity map reconstructed using 6 harmonic terms. **h)** Residual of the velocity map and the reconstructed map. **i)** Simple rotation map constructed for position angle and ellipticity fixed to their global values. **j)** Residual of the velocity map and the simple rotation map. **k)** Position angle and flattening as a function of radius. **l)** k_3/k_1 and k_5/k_1 (from the analysis where position angle and ellipticity are fixed to their global values) as a function of radius.
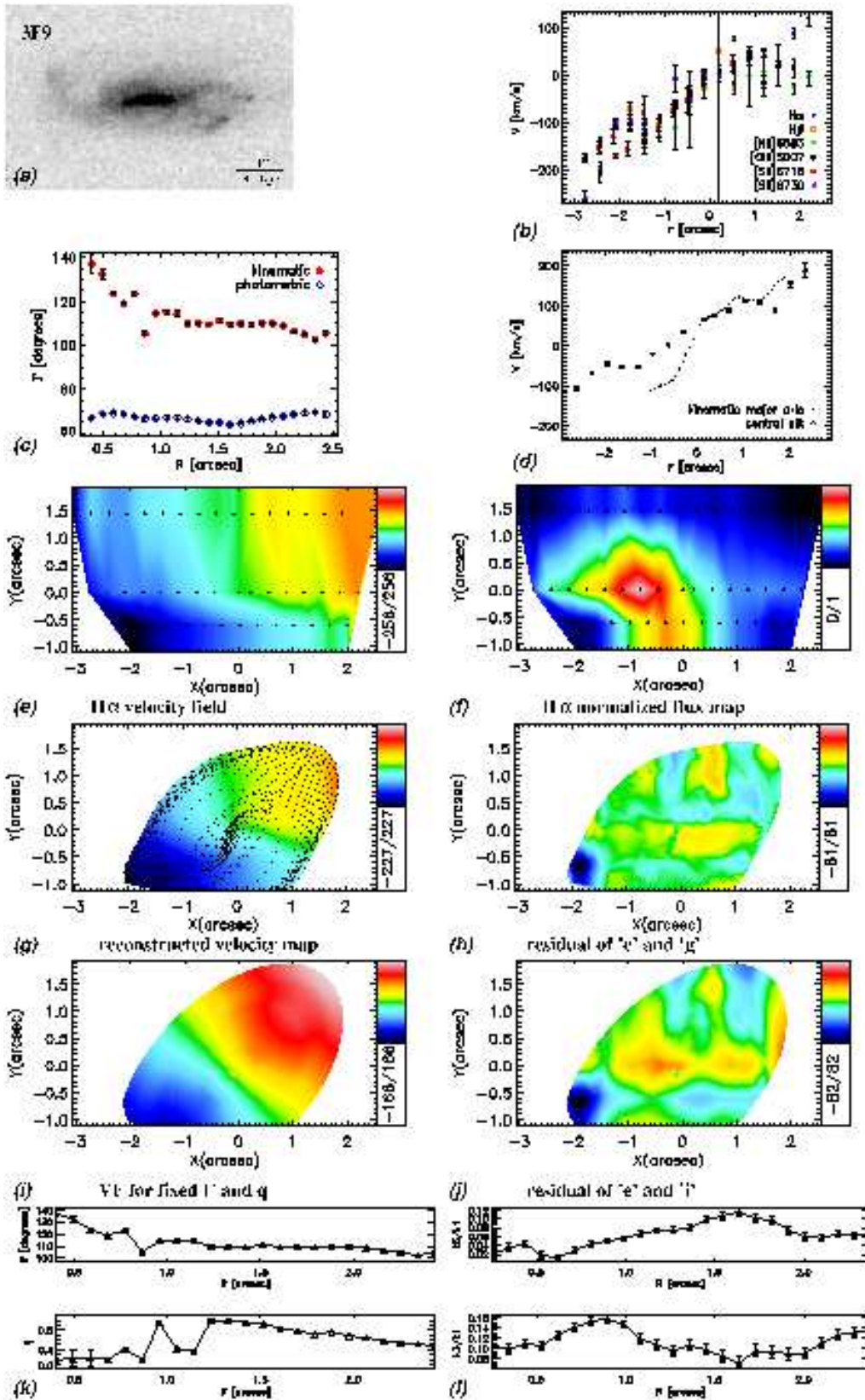
Fig. B.46. a) HST-ACS image of the galaxy in the *V* band. **b)** Rotation curves of different emission lines extracted along the central slit. **c)** Position angles of kinematic and photometric axes as a function of radius. **d)** Rotation curves extracted along the central slit and the kinematic major axis. **e)** [OIII]5007 velocity field. **f)** Normalized [OIII]5007 flux map. **g)** Velocity map reconstructed using 6 harmonic terms. **h)** Residual of the velocity map and the reconstructed map. **i)** Simple rotation map constructed for position angle and ellipticity fixed to their global values. **j)** Residual of the velocity map and the simple rotation map. **k)** Position angle and flattening as a function of radius. **l)** k_3/k_1 and k_5/k_1 (from the analysis where position angle and ellipticity are fixed to their global values) as a function of radius.
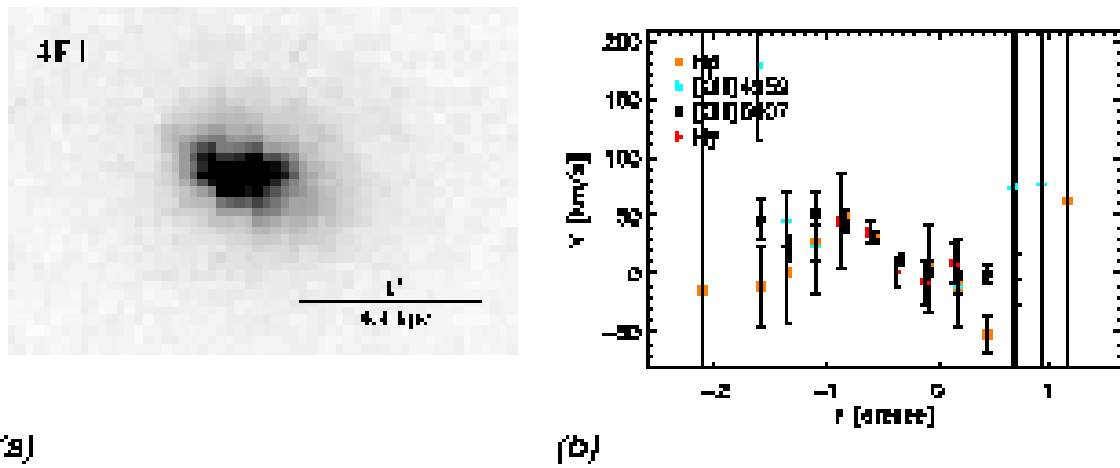
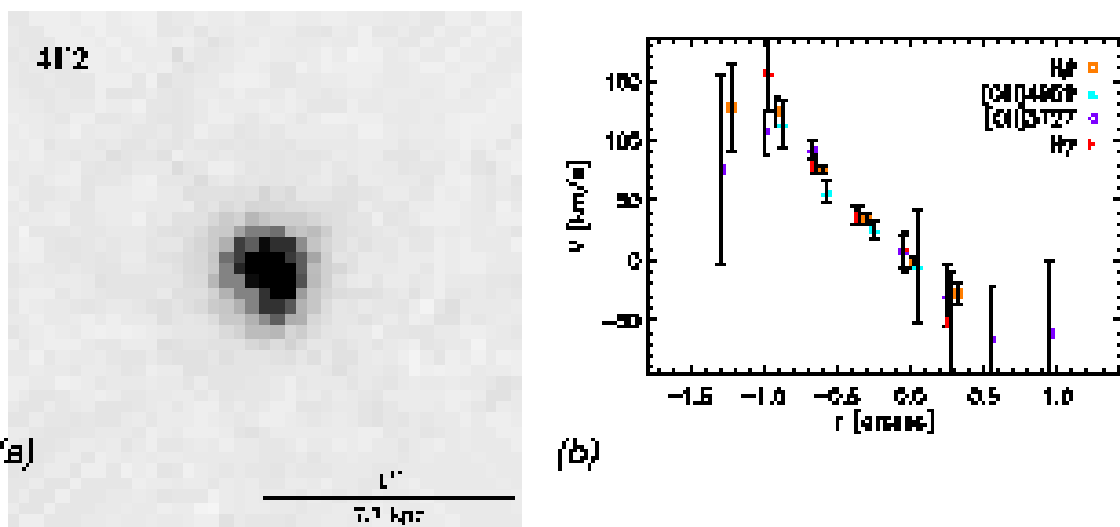**Fig. B.47. a)** HST-ACS image of the galaxy in the *V* band. **b)** Rotation curves of different emission lines extracted along the central slit. **c)** Position angles of kinematic and photometric axes as a function of radius. **d)** Rotation curves extracted along the central slit and the kinematic major axis. **e)** [OII]3727 velocity field. **f)** Normalized [OII]3727 flux map. **g)** Velocity map reconstructed using 6 harmonic terms. **h)** Residual of the velocity map and the reconstructed map. **i)** Simple rotation map constructed for position angle and ellipticity fixed to their global values. **j)** Residual of the velocity map and the simple rotation map. **k)** Position angle and flattening as a function of radius. **l)** k_3/k_1 and k_5/k_1 (from the analysis where position angle and ellipticity are fixed to their global values) as a function of radius.

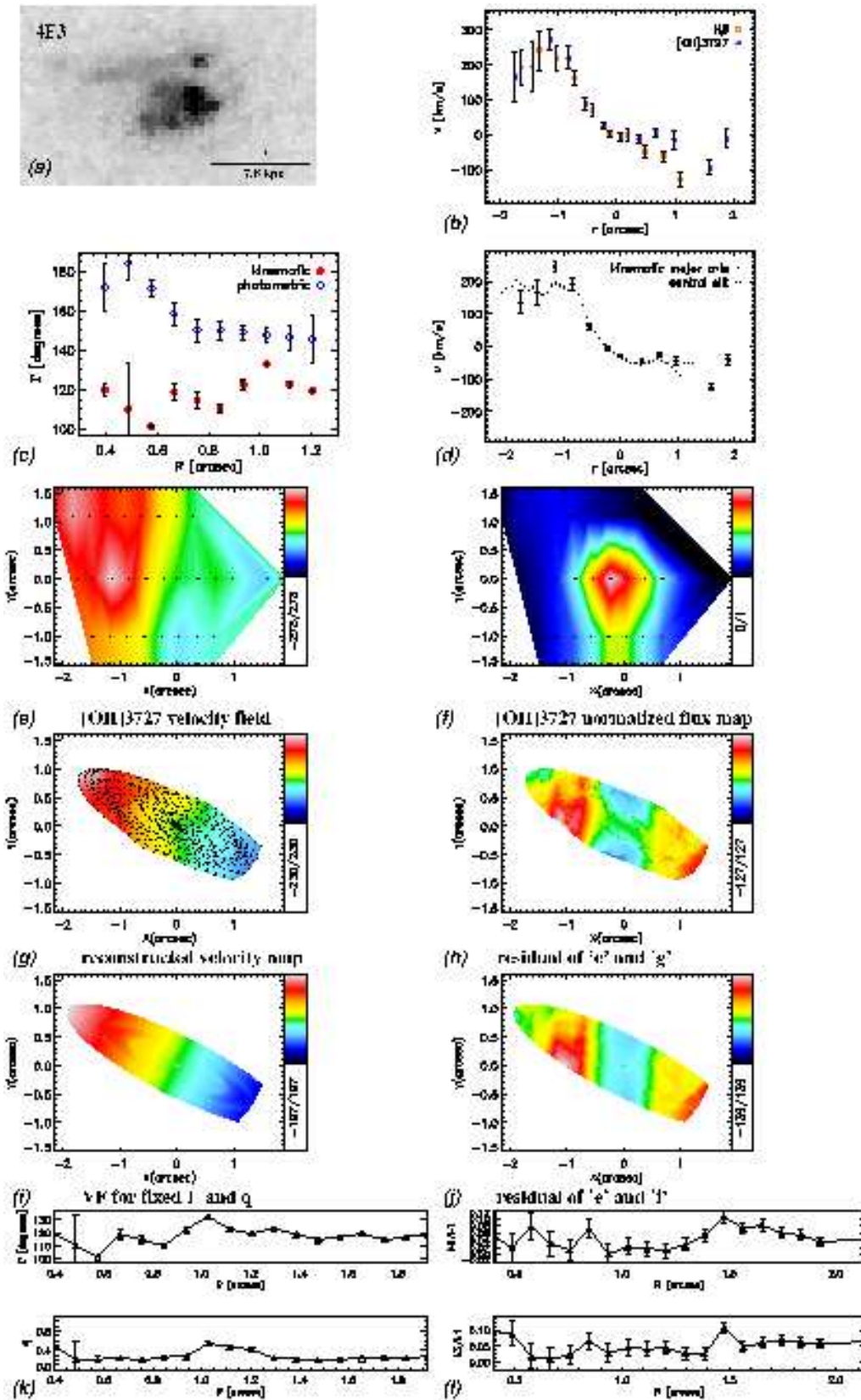**Fig. B.48. a)** HST-ACS image of the galaxy in the *V* band. **b)** Rotation curves of different emission lines extracted along the central slit. **c)** Position angles of kinematic and photometric axes as a function of radius. **d)** Rotation curves extracted along the central slit and the kinematic major axis. **e)** [OII]3727 velocity field. **f)** Normalized [OII]3727 flux map. **g)** Velocity map reconstructed using 6 harmonic terms. **h)** Residual of the velocity map and the reconstructed map. **i)** Simple rotation map constructed for position angle and ellipticity fixed to their global values. **j)** Residual of the velocity map and the simple rotation map. **k)** Position angle and flattening as a function of radius. **l)** k_3/k_1 and k_5/k_1 (from the analysis where position angle and ellipticity are fixed to their global values) as a function of radius.
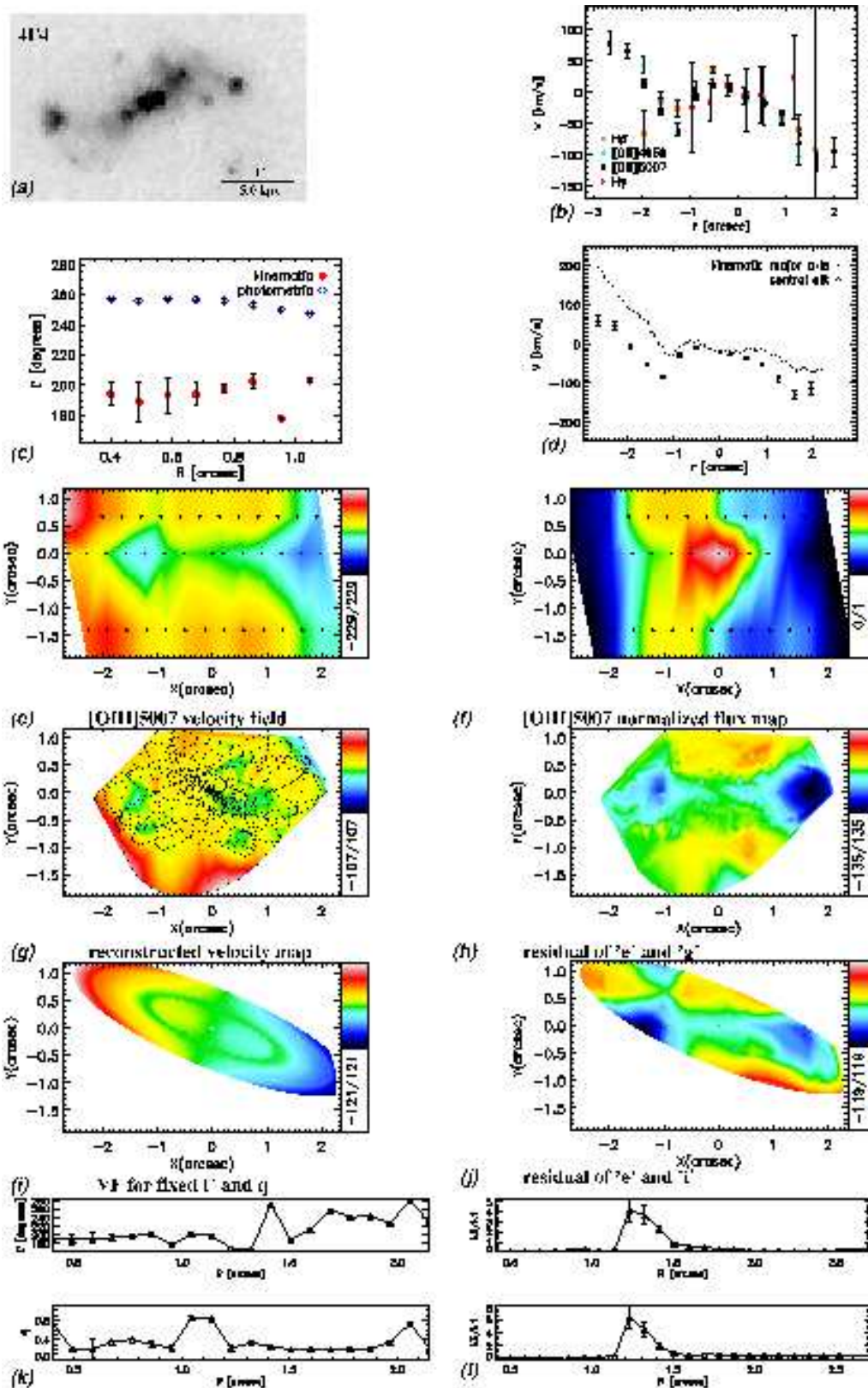
Fig. B.49. a) HST-ACS image of the galaxy in the *V* band. **b)** Rotation curves of different emission lines extracted along the central slit. **c)** Position angles of kinematic and photometric axes as a function of radius. **d)** Rotation curves extracted along the central slit and the kinematic major axis. **e)** [OII]3727 velocity field. **f)** Normalized [OII]3727 flux map. **g)** Velocity map reconstructed using 6 harmonic terms. **h)** Residual of the velocity map and the reconstructed map. **i)** Simple rotation map constructed for position angle and ellipticity fixed to their global values. **j)** Residual of the velocity map and the simple rotation map. **k)** Position angle and flattening as a function of radius. **l)** k_3/k_1 and k_5/k_1 (from the analysis where position angle and ellipticity are fixed to their global values) as a function of radius.
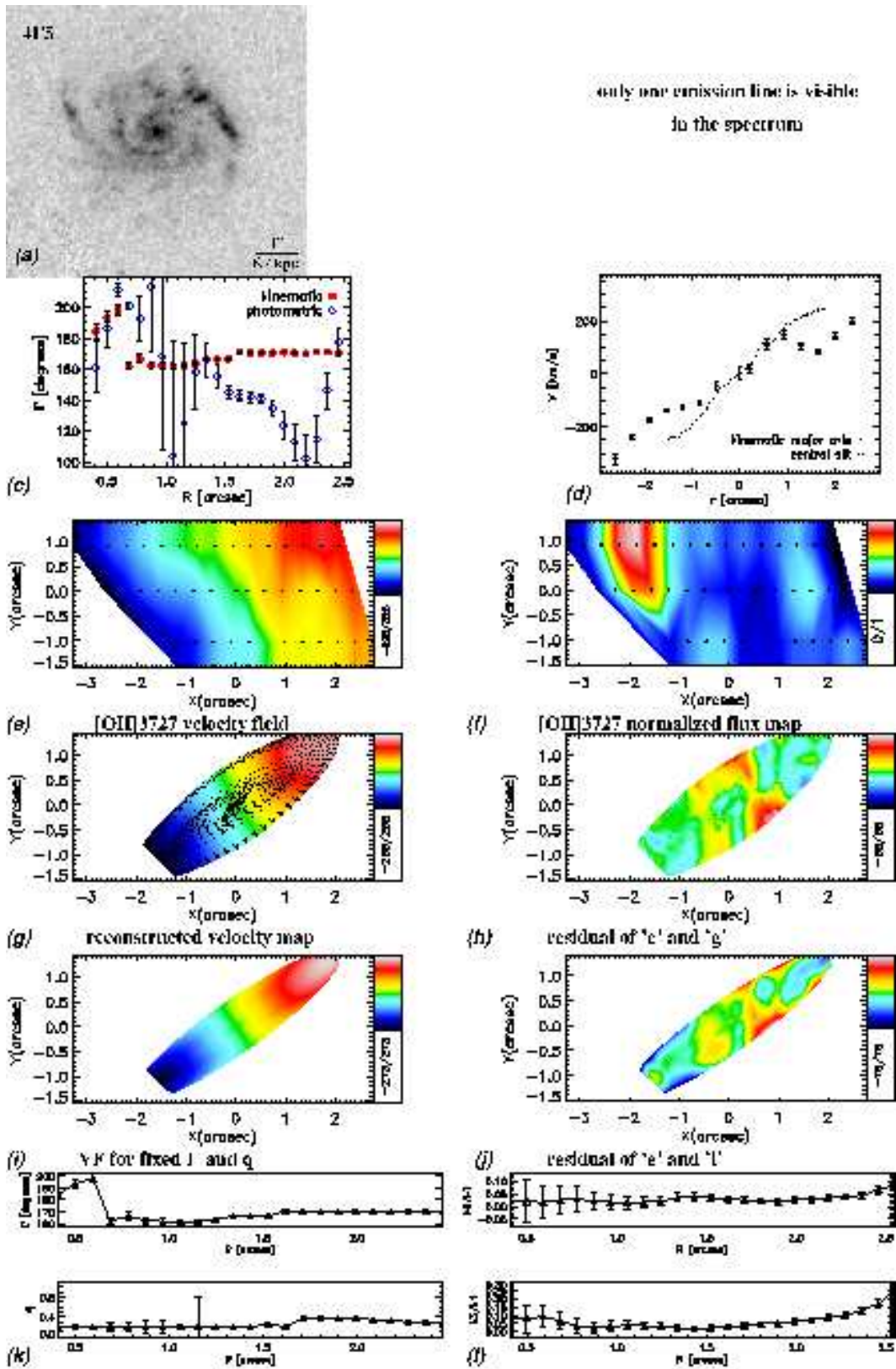
Fig. B.50. a) HST-ACS image of the galaxy in the *V* band. **b)** Rotation curves of different emission lines extracted along the central slit. **c)** Position angles of kinematic and photometric axes as a function of radius. **d)** Rotation curves extracted along the central slit and the kinematic major axis. **e)** [OIII]5007 velocity field. **f.1)** Normalized Hβ flux map. **f.2)** Normalized [OIII]5007 flux map. **g)** Velocity map reconstructed using 6 harmonic terms. **h)** Residual of the velocity map and the reconstructed map. **i)** Simple rotation map constructed for position angle and ellipticity fixed to their global values. **j)** Residual of the velocity map and the simple rotation map. **k)** Position angle and flattening as a function of radius. **l)** k_3/k_1 and k_5/k_1 (from the analysis where position angle and ellipticity are fixed to their global values) as a function of radius.
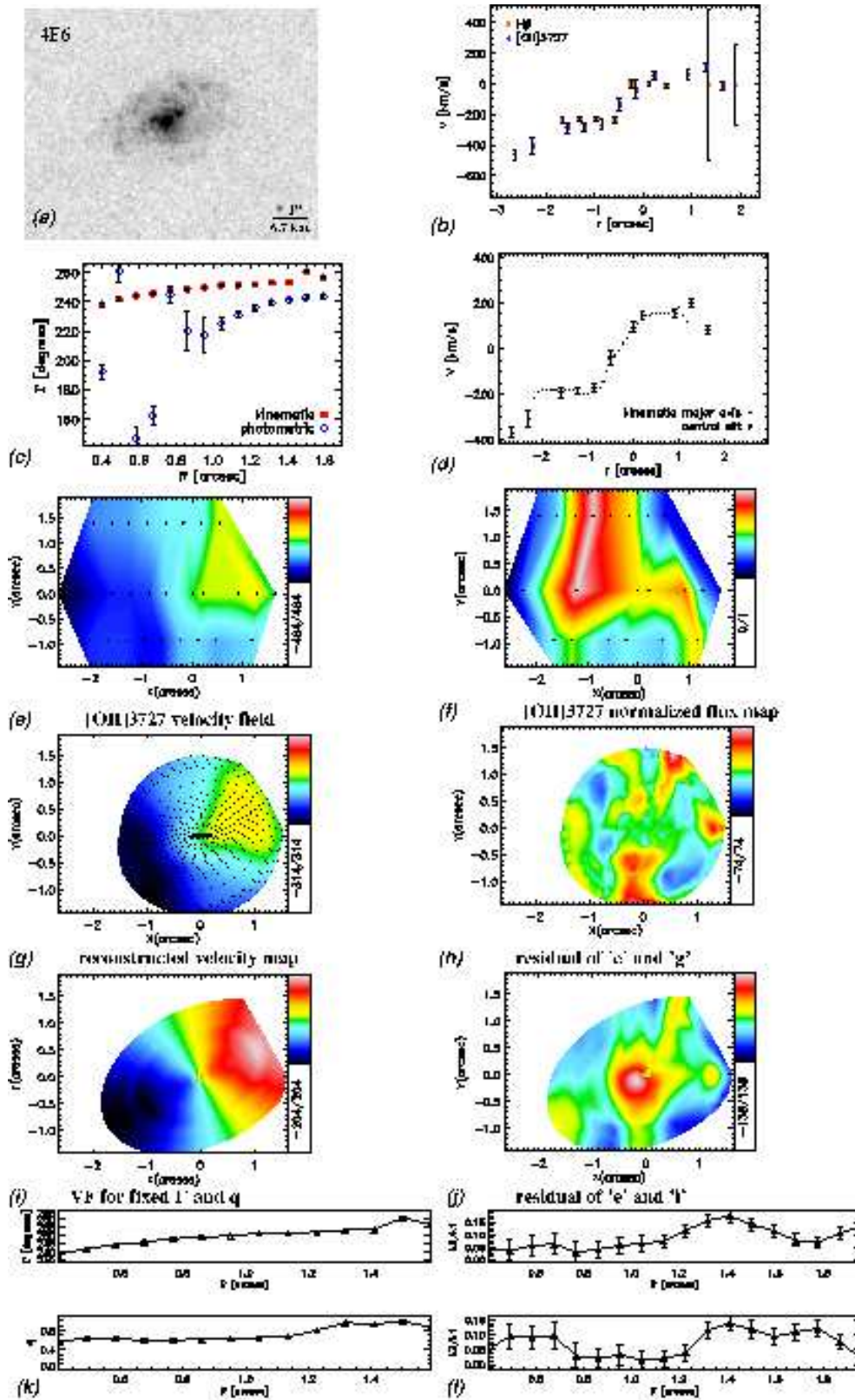
Fig. B.51. a) HST-ACS image of the galaxy in the *V* band. **b)** Rotation curves of different emission lines extracted along the central slit. **c)** Position angles of kinematic and photometric axes as a function of radius. **d)** Rotation curves extracted along the central slit and the kinematic major axis. **e)** [OIII]5007 velocity field. **f)** Normalized [OIII]5007 flux map. **g)** Velocity map reconstructed using 6 harmonic terms. **h)** Residual of the velocity map and the reconstructed map. **i)** Simple rotation map constructed for position angle and ellipticity fixed to their global values. **j)** Residual of the velocity map and the simple rotation map. **k)** Position angle and flattening as a function of radius. **l)** k_3/k_1 and k_5/k_1 (from the analysis where position angle and ellipticity are fixed to their global values) as a function of radius.
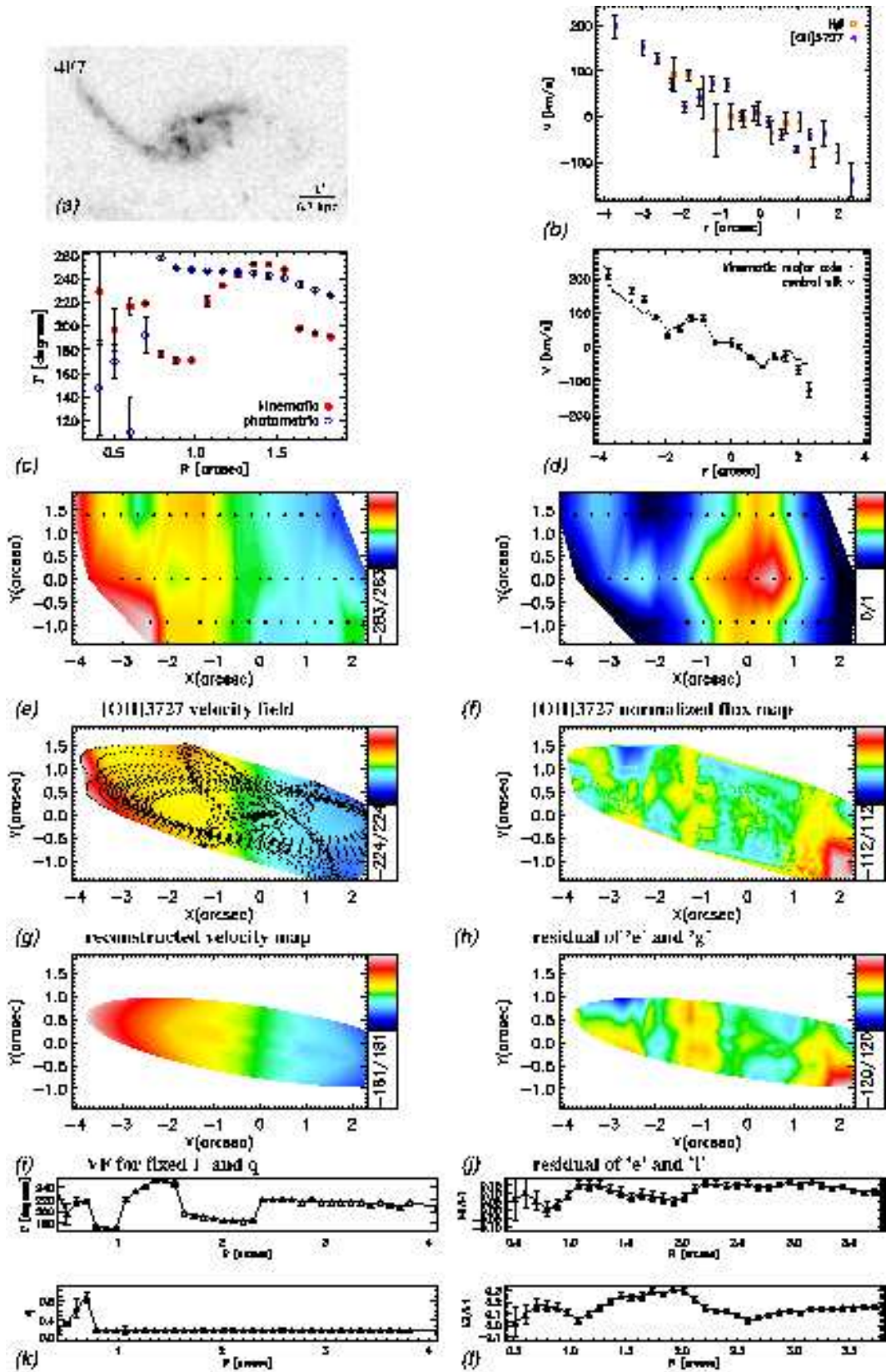
Fig. B.52. a) HST-ACS image of the galaxy in the *V* band. **b)** Rotation curves of different emission lines extracted along the central slit.
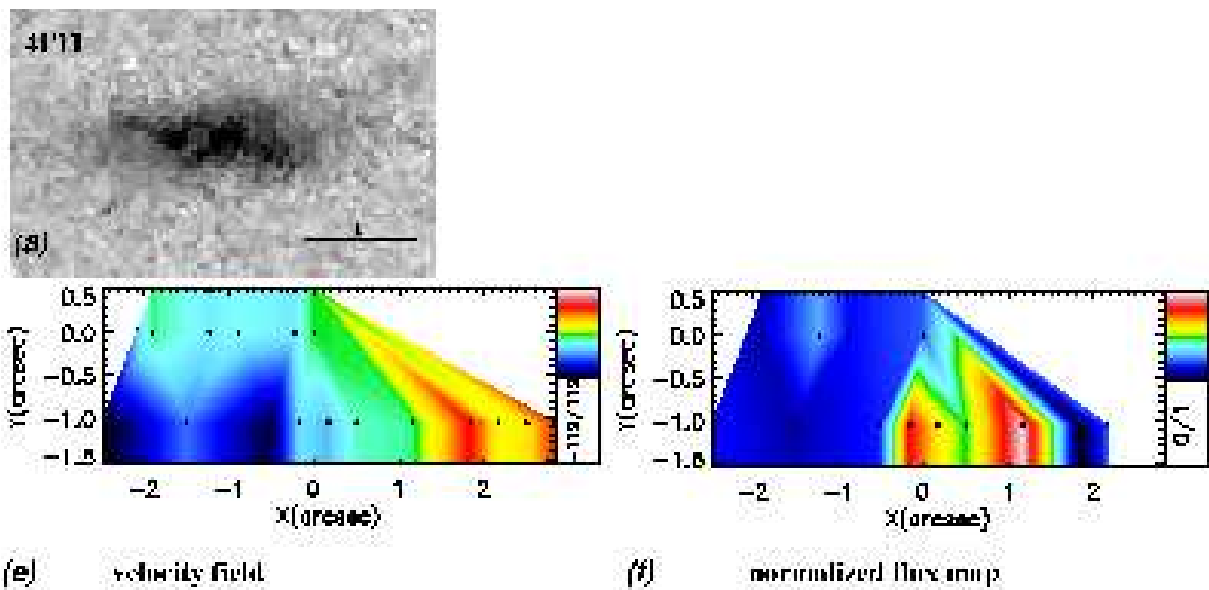
Fig. B.53. a) HST-ACS image of the galaxy in the *V* band. **e)** Velocity field constructed using the emission line which could not be identified. **f)** Normalized flux map of the emission line which could not be identified.

Fig. B.54. a) HST-ACS image of the galaxy in the *V* band. **b)** Rotation curves of different emission lines extracted along the central slit. **c)** Position angles of kinematic and photometric axes as a function of radius. **d)** Rotation curves extracted along the central slit and the kinematic major axis. **e)** [OII]3727 velocity field. **f.1)** Normalized Hβ flux map. **f.2)** Normalized [OII]3727 flux map. **g)** Velocity map reconstructed using 6 harmonic terms. **h)** Residual of the velocity map and the reconstructed map. **i)** Simple rotation map constructed for position angle and ellipticity fixed to their global values. **j)** Residual of the velocity map and the simple rotation map. **k)** Position angle and flattening as a function of radius. **l)** k_3/k_1 and k_5/k_1 (from the analysis where position angle and ellipticity are fixed to their global values) as a function of radius.
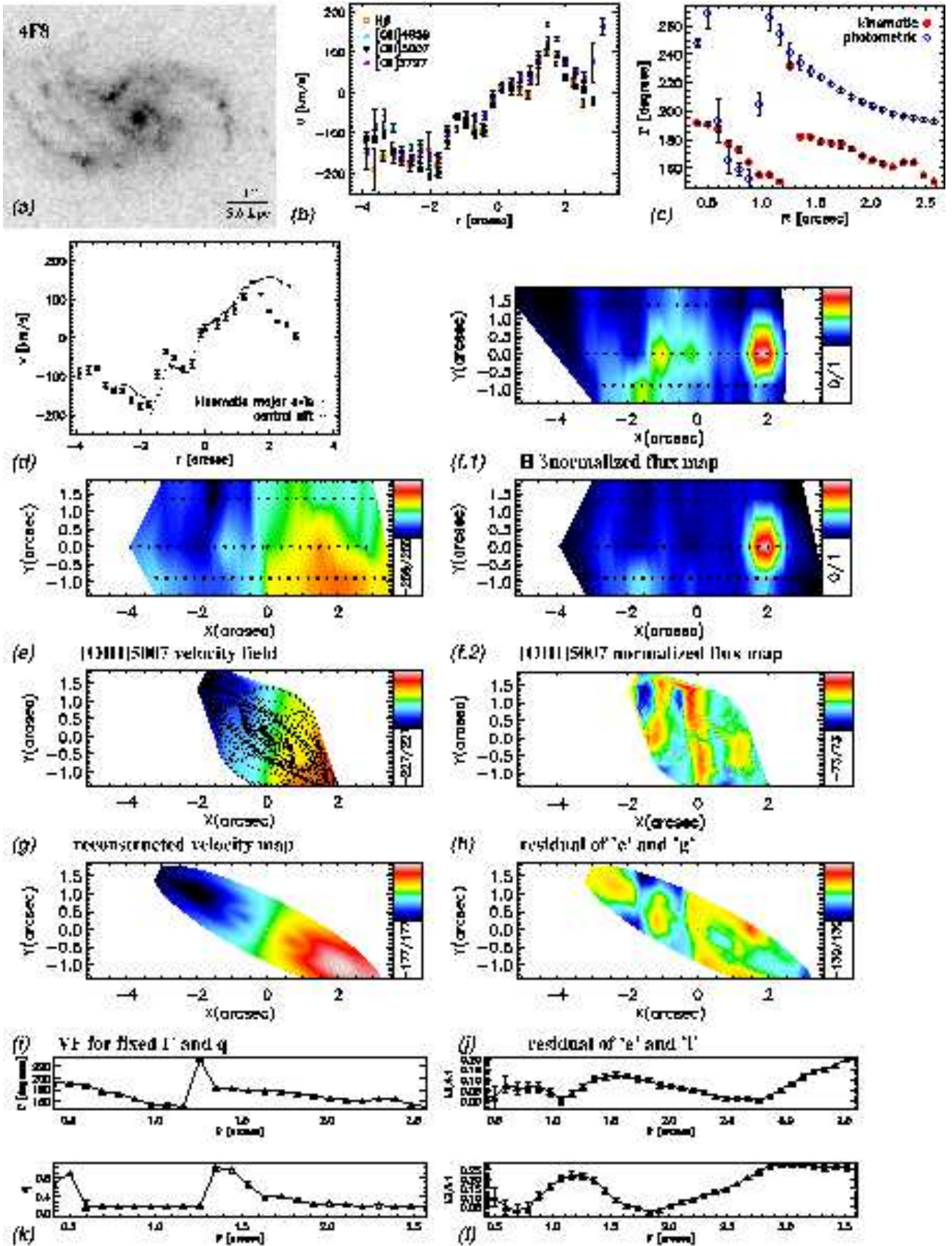
Fig. B.55. a) HST-ACS image of the galaxy in the *V* band. **b)** Rotation curves of different emission lines extracted along the central slit. **c)** Position angles of kinematic and photometric axes as a function of radius. **d)** Rotation curves extracted along the central slit and the kinematic major axis. **e)** [OIII]5007 velocity field. **f)** Normalized [OIII]5007 flux map. **g)** Velocity map reconstructed using 6 harmonic terms. **h)** Residual of the velocity map and the reconstructed map. **i)** Simple rotation map constructed for position angle and ellipticity fixed to their global values. **j)** Residual of the velocity map and the simple rotation map. **k)** Position angle and flattening as a function of radius. **l)** k_3/k_1 and k_5/k_1 (from the analysis where position angle and ellipticity are fixed to their global values) as a function of radius.
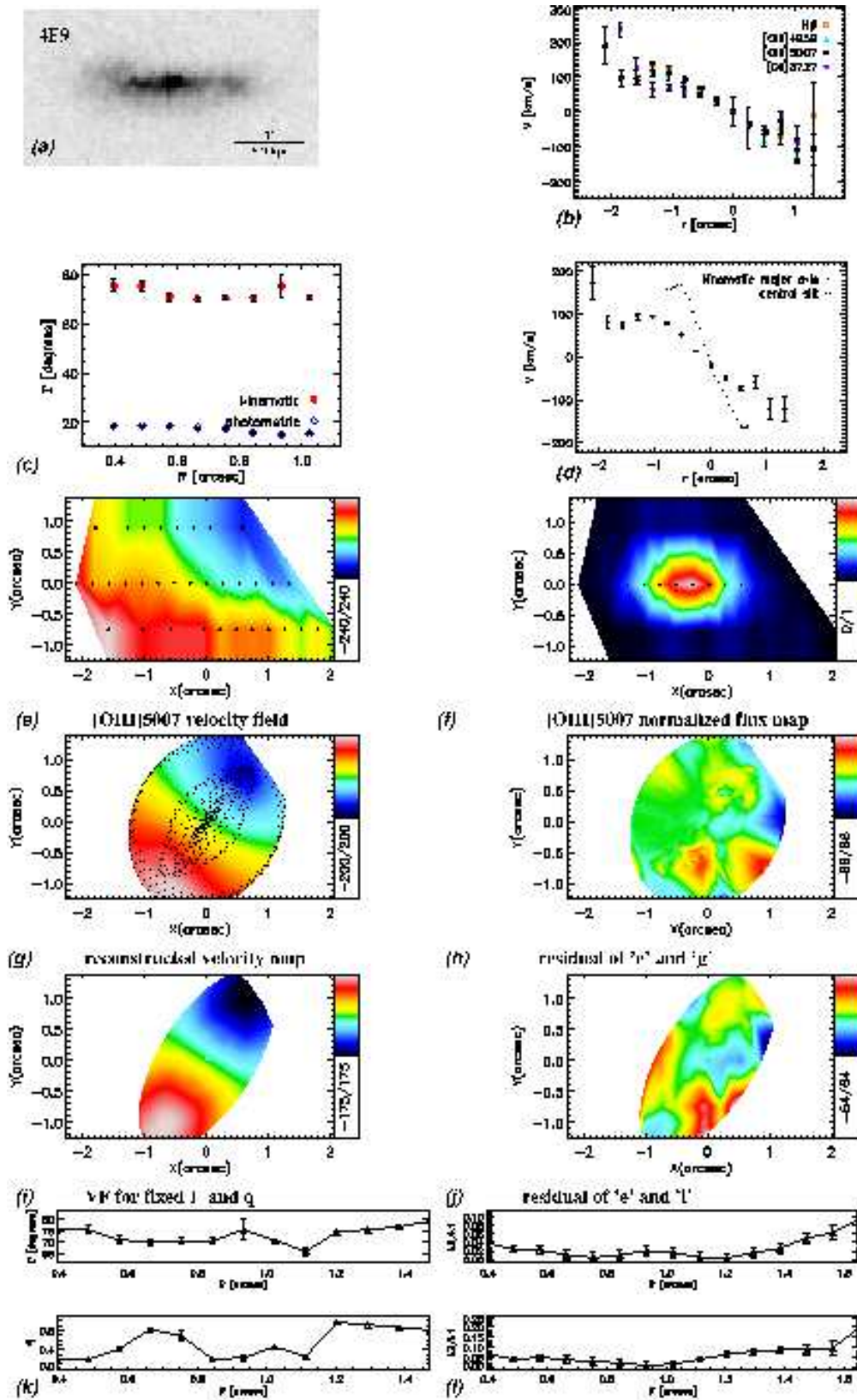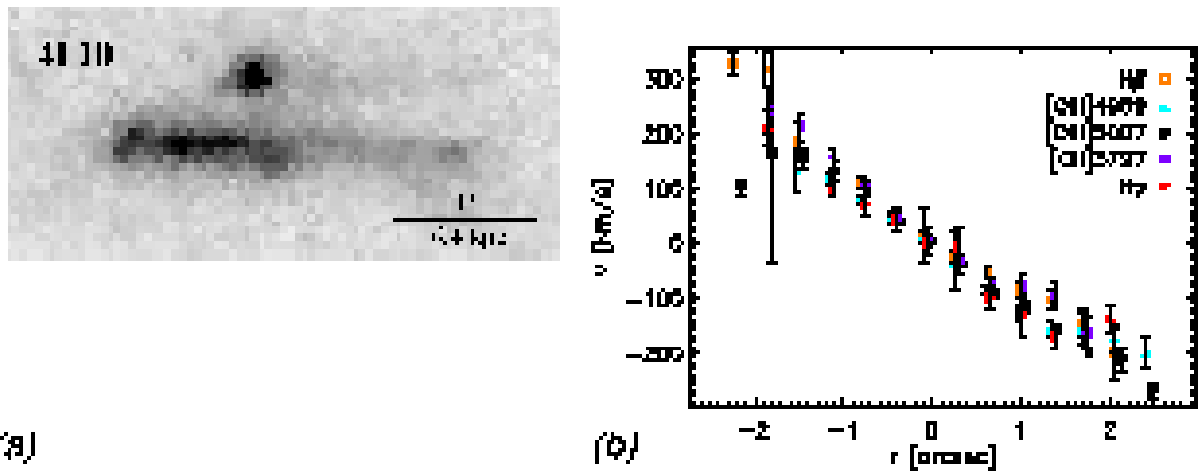
Fig. B.56. *V* band HST-ACS image of galaxies that have very weak or no emission.

Appendix C: Photometric tables

Table C.1. Photometric parameters for the whole sample.

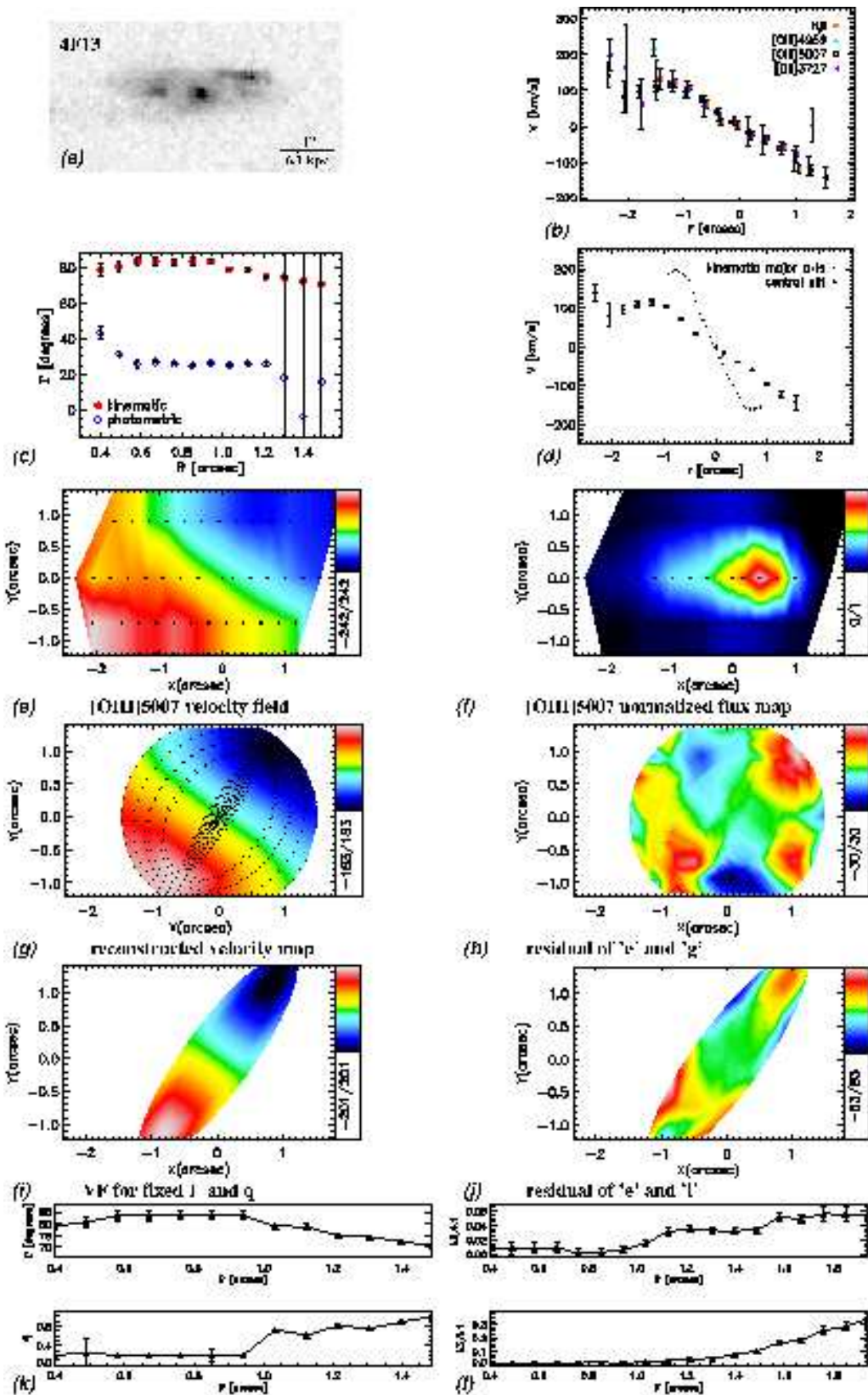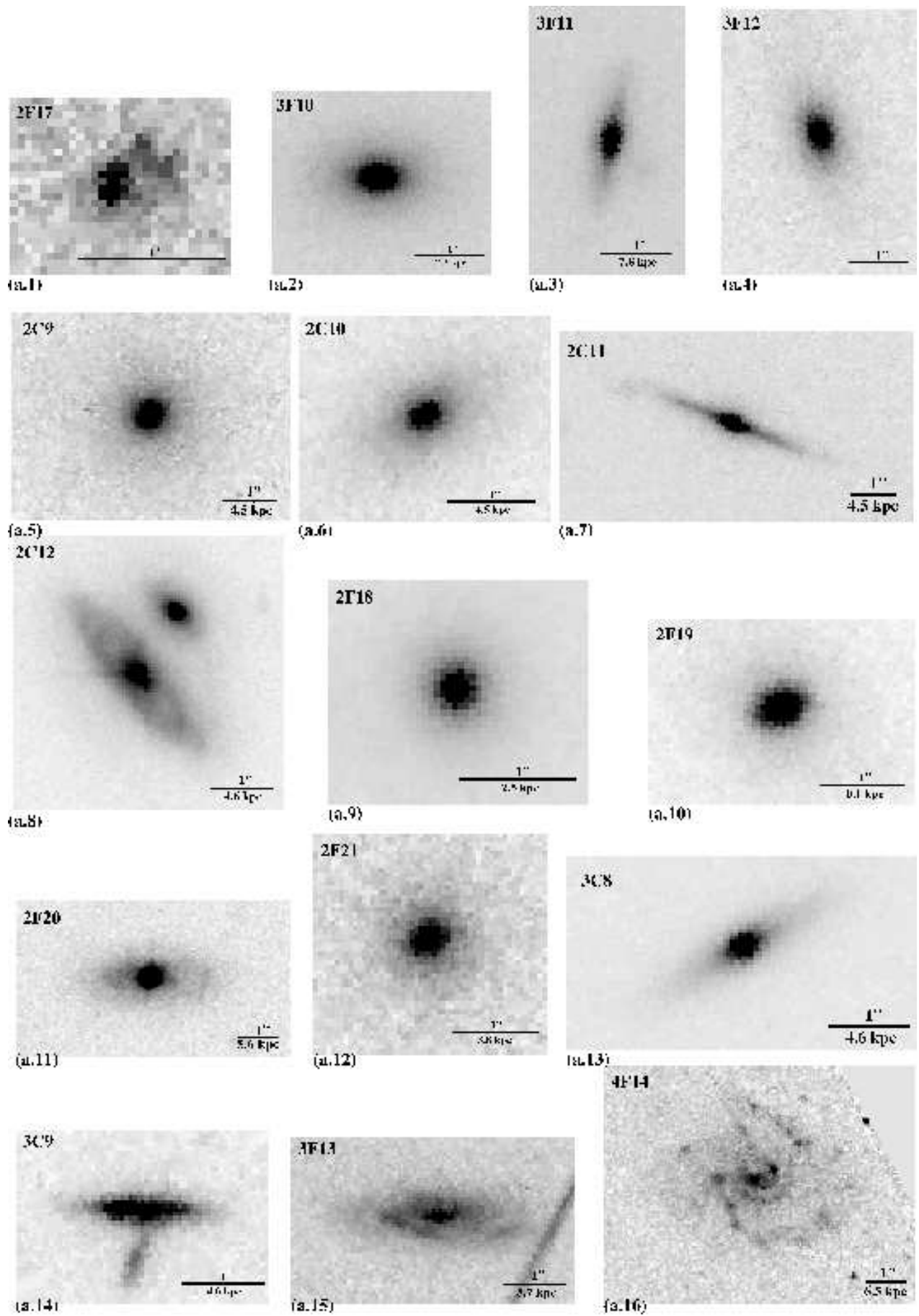| ID	α	δ	M_B	$B-V$	$V-R$	$R-I$	$M_{stellar}[M_\odot]$	A	C	G	M_{20}
(1)	(2)	(3)	(4)	(5)	(6)	(7)	(8)	(9)	(10)	(11)	(12)
1C1	04:54:02.2	-02:57:10	-21.06	0.76	0.61	0.61	2.7e+10	0.21	0.41	0.59	-2.06
1C2	04:54:17.2	-03:01:56	-20.91	0.68	0.59	0.55	1.7e+10	0.09	0.38	0.51	-2.19
1C3	04:54:18.6	-03:01:03	-20.68	0.52	0.50	0.37	7.7e+09	0.13	0.41	0.59	-2.04
1C4	04:54:17.6	-02:59:23	-20.37	0.42	0.44	0.21	3.2e+09	0.18	0.43	0.64	-1.37
1C5	04:54:01.5	-02:59:24	-20.82	0.79	0.62	0.64	3.4e+10	0.19	0.57	0.69	-2.26
1C6	04:54:01.3	-02:59:22	-20.59	0.46	0.49	0.42	8.3e+09	0.26	0.48	0.61	-2.24
1C7	04:54:05.0	-02:59:40	-22.45	0.23	0.36	0.13	5.0e+09	0.38	0.31	0.53	-1.23
1C8	04:54:04.4	-03:00:14	-21.68	0.48	0.49	0.40	1.4e+10	0.29	0.32	0.48	-1.60
1C9	04:54:15.0	-03:00:22	-21.76	0.26	0.36	0.17	4.3e+09	0.41	0.38	0.58	-1.48
1C10	04:54:17.7	-03:02:29	-20.05	0.18	0.36	0.07	1.1e+09	0.21	0.40	0.55	-1.74
1C11	04:54:10.3	-03:00:46	–	–	–	–	-	0.20	0.40	0.65	-2.24
1F1	04:54:02.7	-02:58:41	-20.97	0.47	0.46	0.35	1.4e+10	0.24	0.25	0.43	-1.27
1F2	04:54:03.8	-02:59:19	-21.96	0.43	0.46	0.32	1.4e+10	0.28	0.32	0.54	-1.43
1F3	04:54:14.9	-02:58:17	-20.66	0.26	0.37	0.15	2.0e+09	0.35	0.32	0.53	-1.24
1F4	04:54:07.8	-03:00:33	-18.78	0.28	0.29	0.30	3.8e+08	0.25	0.45	0.58	-1.88
1F5	04:54:10.0	-03:00:28	-19.95	0.35	0.37	0.36	1.7e+09	0.22	0.35	0.58	-1.97
1F6	04:54:18.9	-03:00:05	-18.56	0.39	0.41	0.28	2.8e+08	0.17	0.32	0.47	-1.74
1F7	04:54:02.3	-02:58:10	-21.64	0.40	0.43	0.31	2.1e+10	0.56	0.23	0.47	-1.32
1F8	04:54:10.4	-03:00:47	–	–	–	–	2.9e+10	0.26	0.28	0.51	-1.41
1F9	04:54:10.2	-03:01:57	-20.15	0.74	0.49	0.51	1.4e+10	0.15	0.61	0.71	-2.42
1F10	04:54:00.5	-02:58:15	-19.67	0.33	0.39	0.22	1.4e+09	0.23	0.26	0.40	-1.42
1F11	04:54:20.6	-03:00:16	–	–	–	–	-	0.21	0.36	0.54	-1.93
2C1	10:10:29.0	-12:37:34	-19.90	0.62	0.47	0.45	5.3e+09	0.24	0.37	0.58	-1.20
2C2	10:10:20.5	-12:39:03	-20.77	0.64	0.52	0.49	1.3e+10	0.43	0.41	0.60	-1.38
2C3	10:10:46.8	-12:40:32	-21.22	0.60	0.47	0.45	1.4e+10	0.25	0.46	0.60	-2.05
2C4	10:10:25.9	-12:38:29	–	–	–	–	–	0.22	0.38	0.51	-1.78
2C5	10:10:36.7	-12:40:04	-20.27	0.56	0.51	0.49	7.6e+09	0.50	0.33	0.54	-1.41
2C6	10:10:35.4	-12:39:59	-19.44	0.96	0.66	0.73	7.1e+09	0.16	0.26	0.45	-1.18
2C7	10:10:22.4	-12:40:53	-19.86	0.35	0.43	0.31	3.0e+09	0.22	0.48	0.64	-2.02
2C8	10:10:24.3	-12:37:44	–	–	–	–	–	0.28	0.49	0.64	-1.81
2C9	10:10:28.6	-12:37:37	-19.99	0.79	0.49	0.53	8.3e+09	0.12	0.42	0.51	-2.24
2C10	10:10:45.9	-12:38:31	-19.28	0.75	0.49	0.51	5.9e+09	0.10	0.43	0.54	-2.15
2C11	10:10:27.8	-12:37:07	-19.93	0.88	0.51	0.60	1.5e+10	0.13	0.54	0.66	-2.58
2C12	10:10:30.6	-12:37:23	-21.31	0.79	0.50	0.54	3.0e+10	0.15	0.41	0.59	-1.96
2F1	10:10:44.8	-12:38:31	-20.85	0.27	0.38	0.15	3.9e+09	0.60	0.32	0.56	-0.97
2F2	10:10:38.2	-12:38:14	-18.78	0.93	0.54	0.64	3.4e+09	0.09	0.41	0.53	-2.04
2F3	10:10:41.3	-12:39:21	-21.14	0.39	0.41	0.22	6.9e+09	0.33	0.30	0.51	-1.38
2F4	10:10:41.5	-12:39:19	-21.14	0.65	0.56	0.53	4.0e+10	0.18	0.41	0.53	-2.14
2F5	10:10:31.8	-12:41:03	-21.36	0.90	0.65	0.70	3.6e+10	0.10	0.41	0.53	-2.26
2F6	10:10:44.0	-12:36:35	-18.68	0.50	0.40	0.45	1.6e+09	0.15	0.34	0.53	-1.71
2F7	10:10:34.2	-12:37:27	-16.55	0.53	0.55	0.54	5.1e+08	0.29	0.18	0.39	-0.75
2F8	10:10:46.4	-12:40:36	-19.93	0.62	0.47	0.43	1.2e+10	0.17	0.13	0.32	-0.77
2F9	10:10:33.4	-12:37:13	-20.40	0.72	0.55	0.56	1.0e+10	0.24	0.32	0.47	-1.64
2F10	10:10:30.2	-12:37:26	-20.48	0.53	0.49	0.41	4.1e+09	0.26	0.23	0.43	-1.18
2F11	10:10:33.8	-12:37:19	-21.60	0.65	0.50	0.49	6.9e+09	0.25	0.19	0.35	-1.19
2F12	10:10:42.7	-12:40:21	-21.02	0.48	0.44	0.36	8.0e+09	0.28	0.39	0.54	-1.92
2F13	10:10:36.4	-12:40:09	–	–	–	–	–	0.16	0.12	0.35	-0.77
2F14	10:10:36.9	-12:39:58	–	–	–	–	–	0.28	0.16	0.34	-1.03
2F15	10:10:20.5	-12:39:03	–	–	–	–	–	–	–	–	–
2F16	10:10:20.2	-12:39:01	–	–	–	–	–	–	–	–	–
2F17	10:10:32.2	-12:40:58	–	–	–	–	–	0.39	0.14	0.42	-1.10
2F18	10:10:25.9	-12:38:28	–	–	–	–	2.7e+09	0.20	0.57	0.67	-2.42
2F19	10:10:38.9	-12:38:22	-10.28	1.23	0.77	0.85	–	0.17	0.55	0.62	-2.55
2F20	10:10:40.4	-12:36:31	-20.89	0.84	0.62	0.65	3.2e+10	0.14	0.45	0.57	-2.40
2F21	10:10:37.2	-12:39:57	-18.15	0.91	0.53	0.63	2.4e+09	0.13	0.38	0.51	-2.05
3C1	21:40:16.1	-23:37:10	-17.46	0.69	0.69	0.73	1.7e+09	0.08	0.33	0.48	-1.64
3C2	21:40:05.2	-23:40:44	-19.24	0.69	0.68	0.73	1.4e+10	0.33	0.33	0.51	-1.45
3C3	21:40:16.2	-23:37:13	-19.07	0.84	0.72	0.78	9.3e+09	0.12	0.36	0.54	-1.94
3C4	21:40:15.7	-23:38:53	-20.66	0.79	0.71	0.76	5.0e+10	0.39	0.46	0.55	-2.29
3C5	21:40:24.2	-23:36:51	-18.93	0.30	0.55	0.51	6.6e+09	0.24	0.26	0.43	-1.23

ID	α	δ	M_B	$B-V$	$V-R$	$R-I$	$M_{stellar}[M_\odot]$	A	C	G	M_{20}
(1)	(2)	(3)	(4)	(5)	(6)	(7)	(8)	(9)	(10)	(11)	(12)
3C6	21:40:21.9	-23:41:46	-19.54	0.50	0.63	0.65	9.2e+09	0.41	0.45	0.60	-1.99
3C7	21:40:05.9	-23:36:45	–	–	–	–	–	0.18	0.31	0.44	-1.88
3C8	21:40:28.1	-23:40:27	–	–	–	–	–	0.20	0.54	0.65	-2.37
3C9	21:40:06.9	-23:37:01	-18.48	1.08	0.77	0.84	4.9e+09	0.33	0.36	0.60	-1.44
3F1	21:40:02.9	-23:37:49	-20.27	1.13	0.78	0.85	7.2e+10	0.22	0.40	0.56	-2.16
3F2	21:40:27.1	-23:38:07	–	–	–	–	–	0.26	0.28	0.54	-1.51
3F3	21:40:24.9	-23:41:45	-17.39	0.54	0.64	0.67	3.0e+09	0.24	0.49	0.67	-1.35
3F4	21:40:17.9	-23:38:15	-20.20	0.75	0.70	0.75	3.3e+10	0.40	0.21	0.46	-0.97
3F5	21:40:05.6	-23:36:40	-17.90	0.12	0.47	0.32	7.6e+08	0.26	0.44	0.64	-1.98
3F6	21:40:18.8	-23:38:21	-17.89	0.43	0.60	0.60	1.6e+09	0.13	0.31	0.49	-1.76
3F7	21:40:15.8	-23:36:30	-17.22	0.19	0.50	0.40	1.7e+09	0.29	0.38	0.58	-1.92
3F8	21:40:07.1	-23:40:25	-20.28	0.83	0.72	0.78	6.0e+10	0.32	0.24	0.44	-1.16
3F9	21:40:22.8	-23:39:24	-16.79	0.28	0.55	0.50	1.7e+09	0.16	0.32	0.47	-1.74
3F10	21:40:06.4	-23:36:54	-22.93	0.69	0.60	0.57	3.4e+10	0.11	0.54	0.64	-2.66
3F11	21:40:05.9	-23:36:45	-22.30	0.81	0.49	0.56	1.8e+11	0.22	0.62	0.72	-2.49
3F12	21:40:19.2	-23:38:26	–	–	–	–	–	0.12	0.50	0.60	-2.19
3F13	21:40:11.7	-23:38:10	–	–	–	–	–	–	–	–	–
4C1	04:13:13.8	-65:48:56	-20.04	0.46	0.46	0.29	4.4e+09	0.20	0.26	0.50	-1.53
4C2	04:12:36.6	-65:49:52	-20.57	0.45	0.45	0.28	5.3e+09	0.29	0.41	0.60	-1.68
4C3	04:12:56.4	-65:51:13	-20.38	0.56	0.52	0.46	1.2e+10	0.21	0.41	0.62	-1.39
4F1	04:12:51.7	-65:50:43	-18.86	0.35	0.41	0.23	1.0e+09	0.29	0.48	0.63	-1.54
4F2	04:13:13.2	-65:49:24	-20.79	0.35	0.36	0.26	4.8e+09	0.28	0.61	0.72	-1.84
4F3	04:12:43.1	-65:52:02	-21.72	0.45	0.40	0.34	2.6e+10	0.48	0.33	0.53	-1.15
4F4	04:13:10.4	-65:52:20	-19.74	0.33	0.41	0.21	2.1e+09	0.38	0.33	0.57	-1.13
4F5	04:12:57.1	-65:52:49	-21.70	0.47	0.47	0.37	1.9e+10	0.25	0.19	0.40	-0.95
4F6	04:12:28.3	-65:50:30	-21.00	0.49	0.48	0.37	1.2e+10	0.23	0.30	0.43	-1.88
4F7	04:12:46.4	-65:51:28	-21.39	0.34	0.41	0.18	4.3e+09	0.44	0.19	0.44	-1.20
4F8	04:12:36.8	-65:53:07	-20.84	0.42	0.45	0.31	6.0e+09	0.33	0.24	0.41	-1.08
4F9	04:12:50.6	-65:47:45	-20.17	0.33	0.40	0.18	2.0e+09	0.32	0.32	0.47	-1.59
4F10	04:12:36.6	-65:47:60	-20.03	0.28	0.38	0.16	1.4e+09	0.48	0.30	0.48	-1.01
4F11	04:12:55.8	-65:49:38	–	–	–	–	–	0.12	0.23	0.38	-1.49
4F12	04:12:47.6	-65:53:35	-22.05	0.46	0.47	0.37	1.7e+10	0.35	0.26	0.43	-0.99
4F13	04:13:07.1	-65:47:17	-20.00	0.31	0.40	0.16	1.5e+09	0.37	0.24	0.46	-1.04
4F14	04:12:43.5	-65:51:42	-21.07	0.44	0.46	0.34	9.2e+09	0.38	0.22	0.36	-1.27

Column (1): object ID; Cols. (2, 3): RA and Dec (J2000); Col. (4): rest frame, galactic-extinction corrected Johnson-*B* magnitudes (*k*-correction applied using the `kcorrect` algorithm by Blanton & Roweis (2007)); Cols. (5–7): galactic extinction and k-corrected $B-V$, $V-R$ and $R-I$ colors measured from the FORS2/VLT images (The FORS2 filters B, V and I are close approximations to the Bessel (Bessell 1990) photometric system while R filter is a special filter for FORS2); Col. (8): Stellar mass (measured using the `kcorrect` algorithm by Blanton & Roweis (2007)); Col. (9): asymmetry index; Col. (10): concentration index; Col. (11): Gini coefficient; Col. (12): M_{20} index.

Table C.2. Morphological parameters for the MS 1008, MS 2137 and Cl 0413 samples.

ID	comp	$F606W$	R_e/R_d(kpc)	n	q	PA
(1)	(2)	(3)	(4)	(5)	(6)	(7)
2C1	exp disk	20.57 ± 0.00	4.14 ± 0.01	–	0.15 ± 0.00	61.22 ± 0.05
2C2	exp disk	20.62 ± 0.00	3.17 ± 0.03	–	0.68 ± 0.00	61.64 ± 0.67
2C3	exp disk	19.86 ± 0.00	5.15 ± 0.03	–	0.87 ± 0.00	-11.41 ± 1.36
2C4	exp disk	22.66 ± 0.01	2.37 ± 0.08	–	0.46 ± 0.01	-84.68 ± 0.99
	Sérsic bulge	23.15 ± 0.02	1.07 ± 0.02	0.49 ± 0.01	0.40 ± 0.00	-79.40 ± 0.44
2C5	exp disk	20.55 ± 0.01	2.39 ± 0.02	–	0.83 ± 0.00	71.68 ± 1.82
2C6	exp disk	21.13 ± 0.00	5.36 ± 0.03	–	0.16 ± 0.00	-4.39 ± 0.08
2C7	exp disk	21.29 ± 0.02	1.54 ± 0.01	–	0.73 ± 0.01	-30.79 ± 1.14
	Sérsic bulge	21.72 ± 0.03	2.13 ± 0.03	1.89 ± 0.03	0.23 ± 0.00	-20.02 ± 0.13
2C8	exp disk	21.46 ± 0.01	1.42 ± 0.01	–	0.64 ± 0.00	-48.14 ± 1.20
	Sérsic bulge	22.34 ± 0.03	1.05 ± 0.02	1.55 ± 0.05	0.28 ± 0.01	-75.94 ± 0.46
2C9	exp disk	21.43 ± 0.06	5.21 ± 0.12	–	0.73 ± 0.02	43.26 ± 2.12
2C10	exp disk	21.50 ± 0.04	2.90 ± 0.03	–	0.55 ± 0.00	-13.84 ± 0.41
	Sérsic bulge	22.64 ± 0.13	0.94 ± 0.17	3.44 ± 0.39	0.69 ± 0.01	-20.33 ± 1.58
2C11	exp disk	21.47 ± 0.01	3.92 ± 0.05	–	0.07 ± 0.00	23.44 ± 0.05
	Sérsic bulge	20.98 ± 0.01	2.10 ± 0.06	4.63 ± 0.07	0.49 ± 0.00	21.09 ± 0.38
2C12	exp disk	19.92 ± 0.00	3.30 ± 0.01	–	0.38 ± 0.00	54.83 ± 0.10
2F1	exp disk	22.06 ± 0.01	2.08 ± 0.01	–	0.34 ± 0.00	-59.02 ± 0.24
2F2	exp disk	21.26 ± 0.01	2.25 ± 0.02	–	0.55 ± 0.00	-37.44 ± 0.41
	Sérsic bulge	22.15 ± 0.03	3.62 ± 0.00	6.64 ± 0.23	0.59 ± 0.01	-37.83 ± 1.75
2F3	exp disk	21.80 ± 0.01	3.50 ± 0.06	–	0.66 ± 0.01	53.34 ± 0.98
2F4	exp disk	22.31 ± 0.04	1.99 ± 0.03	–	0.92 ± 0.02	7.72 ± 8.31
	Sérsic bulge	23.30 ± 0.26	1.80 ± 1.04	8.00 ± 2.30	0.55 ± 0.04	-80.62 ± 2.45
2F5	exp disk	21.62 ± 0.02	5.85 ± 0.11	–	0.61 ± 0.01	55.29 ± 1.34
	Sérsic bulge	20.56 ± 0.06	21.20 ± 2.19	8.00 ± 0.22	0.65 ± 0.01	49.96 ± 0.74
2F6	exp disk	20.18 ± 0.00	2.21 ± 0.01	–	0.40 ± 0.00	-51.62 ± 0.13
2F7	exp disk	24.39 ± 0.03	1.61 ± 0.06	–	0.21 ± 0.01	27.67 ± 0.78
2F8	exp disk	22.72 ± 0.03	5.37 ± 0.23	–	0.41 ± 0.01	-16.63 ± 1.58
2F9	exp disk	21.62 ± 0.01	3.45 ± 0.05	–	0.33 ± 0.00	-42.86 ± 0.38
2F10	exp disk	20.87 ± 0.00	6.08 ± 0.04	–	0.19 ± 0.00	-79.34 ± 0.10
2F11	exp disk	20.13 ± 0.01	5.64 ± 0.05	–	0.94 ± 0.01	-18.94 ± 5.13
2F12	exp disk	19.84 ± 0.00	2.77 ± 0.01	–	0.94 ± 0.00	-69.08 ± 1.84
2F13	exp disk	23.79 ± 0.05	0.′′76 ± 0.′′05	–	0.30 ± 0.02	63.86 ± 1.62
2F14	exp disk	22.25 ± 0.06	0.′′55 ± 0.′′03	–	0.74 ± 0.00	85.43 ± 0.00
2F17	exp disk	24.33 ± 0.02	0.′′16 ± 0.′′01	–	0.63 ± 0.02	-88.64 ± 3.00
2F18	exp disk	22.45 ± 0.04	0.71 ± 0.02	–	0.85 ± 0.02	61.53 ± 6.92
	Sérsic bulge	20.62 ± 0.01	1.38 ± 0.05	5.32 ± 0.12	0.91 ± 0.01	45.36 ± 3.13
2F19	exp disk	21.22 ± 0.01	0.07 ± 0.00	–	0.79 ± 0.01	76.85 ± 1.27
	Sérsic bulge	21.68 ± 0.01	0.02 ± 0.00	1.77 ± 0.03	0.74 ± 0.00	-33.67 ± 0.67
2F20	exp disk	20.94 ± 0.00	3.80 ± 0.03	–	0.43 ± 0.00	-84.05 ± 0.22
	Sérsic bulge	22.26 ± 0.01	0.67 ± 0.01	1.23 ± 0.03	0.85 ± 0.01	-25.12 ± 2.00
2F21	exp disk	23.31 ± 0.07	1.63 ± 0.08	–	0.57 ± 0.03	-9.64 ± 2.74
	Sérsic bulge	21.78 ± 0.03	4.99 ± 0.61	4.59 ± 0.32	0.68 ± 0.01	77.47 ± 1.58
3C1	exp disk	22.86 ± 0.01	1.19 ± 0.02	–	0.43 ± 0.00	-85.27 ± 0.56
3C2	exp disk	20.40 ± 0.00	3.81 ± 0.02	–	0.45 ± 0.00	63.61 ± 0.16
3C3	exp disk	20.91 ± 0.00	2.74 ± 0.01	–	0.41 ± 0.00	-30.27 ± 0.13
	Sérsic bulge	24.05 ± 0.03	0.65 ± 0.02	0.99 ± 0.06	0.66 ± 0.02	19.67 ± 3.16
3C4	exp disk	19.76 ± 0.02	4.25 ± 0.03	–	0.51 ± 0.00	81.07 ± 0.21
	Sérsic bulge	20.11 ± 0.04	2.33 ± 0.15	4.73 ± 0.15	0.35 ± 0.00	74.28 ± 0.12
3C5	exp disk	20.70 ± 0.00	3.83 ± 0.02	–	0.65 ± 0.00	26.97 ± 0.46
3C6	exp disk	20.83 ± 0.00	2.42 ± 0.01	–	0.60 ± 0.00	-36.02 ± 0.28

ID (1)	comp (2)	$F606W$ (3)	R_e/R_d(kpc) (4)	n (5)	q (6)	PA (7)
3C7	exp disk	21.58 ± 0.01	3.59 ± 0.03	–	0.36 ± 0.00	84.27 ± 0.24
	Sérsic bulge	25.08 ± 0.05	0.67 ± 0.02	0.40 ± 0.08	0.76 ± 0.03	59.11 ± 7.07
3C8	exp disk	21.38 ± 0.01	2.30 ± 0.02	–	0.25 ± 0.00	-0.15 ± 0.10
	Sérsic bulge	21.91 ± 0.01	0.41 ± 0.01	2.36 ± 0.06	0.77 ± 0.01	-0.01 ± 1.27
3C9	exp disk	22.04 ± 0.01	1.51 ± 0.01	–	0.21 ± 0.00	57.93 ± 0.12
3F1	exp disk	20.76 ± 0.09	4.53 ± 0.35	–	0.47 ± 0.02	88.06 ± 2.63
3F2	Sérsic	23.86 ± 0.01	0.37 ± 0.01	0.49 ± 0.03	0.86 ± 0.01	21.10 ± 4.63
3F3	exp disk	21.21 ± 0.01	1.52 ± 0.01	–	0.52 ± 0.00	-85.25 ± 0.40
3F4	Sérsic galaxy	22.07 ± 0.04	4.27 ± 0.23	3.69 ± 0.11	0.92 ± 0.01	63.62 ± 5.77
3F5	exp disk	22.91 ± 0.08	0.62 ± 0.01	–	0.56 ± 0.01	-22.48 ± 1.33
	Sérsic bulge	23.08 ± 0.09	0.88 ± 0.06	3.09 ± 0.33	0.74 ± 0.02	-42.64 ± 6.24
3F6	exp disk	21.96 ± 0.01	2.16 ± 0.02	–	0.30 ± 0.00	-69.12 ± 0.20
3F7	exp disk	20.78 ± 0.01	3.34 ± 0.04	–	0.65 ± 0.01	-12.81 ± 0.82
3F8	exp disk	20.47 ± 0.00	5.28 ± 0.03	–	0.64 ± 0.00	82.54 ± 0.43
3F9	exp disk	20.85 ± 0.01	2.98 ± 0.01	–	0.34 ± 0.00	64.12 ± 0.15
3F10	exp disk	21.80 ± 0.05	7.51 ± 0.18	–	0.89 ± 0.02	-64.26 ± 8.70
	Sérsic bulge	19.46 ± 0.02	17.68 ± 0.75	8.00 ± 0.11	0.60 ± 0.00	-32.79 ± 0.24
3F11	exp disk	22.63 ± 0.03	2.74 ± 0.03	–	0.13 ± 0.00	44.70 ± 0.13
	Sérsic bulge	21.14 ± 0.01	3.00 ± 0.09	7.05 ± 0.18	0.56 ± 0.01	45.90 ± 0.47
3F12	exp disk	22.63 ± 0.07	0.″79 ± 0.″03	–	0.34 ± 0.01	37.03 ± 0.71
	Sérsic bulge	21.64 ± 0.05	0.″54 ± 0.″04	4.02 ± 0.13	0.63 ± 0.01	35.39 ± 0.70
4C1	exp disk	22.16 ± 0.01	2.99 ± 0.03	–	0.27 ± 0.00	25.29 ± 0.21
4C2	exp disk	21.88 ± 0.00	1.67 ± 0.01	–	0.59 ± 0.00	-56.86 ± 0.40
4C3	exp disk	22.40 ± 0.01	2.38 ± 0.06	–	0.86 ± 0.01	39.80 ± 3.35
	Sérsic bulge	22.63 ± 0.03	2.01 ± 0.01	0.20 ± 0.01	0.87 ± 0.01	57.35 ± 1.61
4F1	exp disk	22.15 ± 0.00	1.14 ± 0.01	–	0.74 ± 0.01	-14.87 ± 1.05
	Sérsic bulge	23.03 ± 0.01	0.71 ± 0.00	0.48 ± 0.02	0.43 ± 0.00	-6.59 ± 0.49
4F2	exp disk	24.75 ± 0.11	0.36 ± 0.01	–	0.11 ± 0.18	24.15 ± 1.65
	Sérsic bulge	23.27 ± 0.01	0.72 ± 0.01	1.87 ± 0.08	0.81 ± 0.01	-36.89 ± 3.40
4F3	Sérsic galaxy	22.51 ± 0.01	4.13 ± 0.05	0.85 ± 0.02 –	0.79 ± 0.01	-32.88 ± 1.64
4F4	exp disk	21.71 ± 0.01	3.66 ± 0.03	–	0.28 ± 0.00	59.17 ± 0.23
4F5	exp disk	20.84 ± 0.00	6.46 ± 0.03	–	0.82 ± 0.01	-34.24 ± 1.22
4F6	exp disk	21.71 ± 0.04	4.68 ± 0.07	–	0.60 ± 0.01	60.91 ± 0.72
	Sérsic bulge	23.60 ± 0.29	4.00 ± 1.18	2.63 ± 0.34	0.69 ± 0.03	-66.50 ± 4.63
4F7	exp disk	21.57 ± 0.01	5.98 ± 0.05	–	0.40 ± 0.00	69.82 ± 0.25
4F8	exp disk	20.59 ± 0.00	6.25 ± 0.04	–	0.67 ± 0.00	13.23 ± 0.48
	Sérsic bulge	24.26 ± 0.27	2.73 ± 1.66	8.00 ± 2.54	0.24 ± 0.03	84.10 ± 1.66
4F9	exp disk	21.71 ± 0.00	3.21 ± 0.00	–	0.22 ± 0.00	16.39 ± 0.00
4F10	Sérsic galaxy	22.64 ± 0.01	5.84 ± 0.06	0.84 ± 0.02	0.17 ± 0.00	42.87 ± 0.14
4F11	exp disk	22.64 ± 0.01	0.″54 ± 0.″01	–	0.31 ± 0.00	-40.26 ± 0.44
4F12	exp disk	20.39 ± 0.02	7.42 ± 0.04	–	0.71 ± 0.00	-41.83 ± 0.61
4F13	exp disk	21.84 ± 0.01	4.48 ± 0.04	–	0.30 ± 0.00	27.72 ± 0.22
4F14	exp disk	21.14 ± 0.01	5.85 ± 0.05	–	0.78 ± 0.01	-32.58 ± 1.13

Column (1): object ID; Col. (2): component; Col. (3): total magnitude; Col. (4): effective radius of the bulge/scale length of the disk; Col. (5): Sérsic index of the bulge profile; Col. (6): flattening; Col. (7): position angle of the disk measured from North through East.
The photometric zero point of the magnitude measurements is $Z_p^{F606W} = 26.398$. The parameters of 2F14 are unreliable since there is a diffraction spike on top of it. The HST image of 3F7 is incomplete and therefore, its parameters are also unreliable. The disk scale length of these galaxies is not used in the analysis. 3F13 could not be analyzed because of the diffraction spike on the image. Col. (4) is given in arcseconds in case the redshift of a galaxy is unknown.